Experimental analysis of inkjet printed polymer electrolyte fuel cell electrodes

by

Shantanu Shukla

A thesis submitted in partial fulfillment of the requirements for the degree of

Doctor of Philosophy

Department of Mechanical Engineering
University of Alberta

Abstract

The success of commercial applicability of polymer electrolyte fuel cells (PEFCs) depends on the cost competitiveness with respect to current energy sources. A major fraction of the system cost can be mitigated by reducing the amount of platinum (Pt) catalyst in the electrodes and by improving the catalyst utilization. The electrode fabrication process governs the electrode microstructure and Pt loading. Application of inkjet printing (IJP) to PEFC electrode fabrication is a relatively recent introduction and has not been extensively studied. The drop-on-demand nature of this method allows for a precise control over the deposition process, thickness and Pt loading of the electrodes. A detailed analysis of this method is therefore essential to understand its feasibility as a fabrication tool.

In this work, a comprehensive analysis of inkjet printed electrodes has been carried out. By studying the effect of Nafion (from 10 wt% to 50 wt%) in thin, low Pt loading IJP electrodes, the performance is not found to be affected by Nafion loading in the range of 20 - 40 wt%. The effect of Pt loading on active area, Tafel slope, reaction order and evaluation of oxygen transport resistance for IJP electrodes has been carried out to understand their lower performance compared to a conventional spray coated electrode. The reduced performance of IJP electrodes at higher Pt loadings is associated to a reduction in the active area and porosity.

In an attempt to improve reactant transport, a novel electrode coated membrane (ECM) architecture is developed where the carbon micro-porous layer (MPL) is fab-

ricated directly over the catalyst layer. Results indicated a lower transport resistance in ECMs as compared to using an MPL based diffusion media. Inkjet printing is also implemented to study patterned electrode structures. However, fine enough patterns to show the advantage of patterned structures could not be observed.

Lastly, a study of particle interactions using colloidal science is carried out to understand the effect of dispersion solvents on ink stability. A semi-empirical model based on diffusion limited aggregation is developed to evaluate the rate of particle aggregation and predict the stability time. Experimental determination of stability was carried out for carbon based inks in non-aqueous dispersion media based on visual inspection and measurement of particle size by dynamic light scattering. A qualitative comparison of the stability time between the model and experimental observation could be made.

Overall, this work presents an improved performance of IJP electrodes compared to previous literature, possible reasons for the reduced performance compared to conventional electrodes based on detailed analysis of electrode parameters, a novel electrode coated membrane architecture using IJP that improves the transport resistance and a simple semi-empirical model for determination of ink dispersion stability.

Keywords: Electrode fabrication, inkjet printing, fuel cell testing, catalyst ink dispersion, colloidal interactions

Preface

Parts of chapter 2 of this thesis have been published as S. Shukla, K. Domican, K. Karan, S. Bhattacharjee and M. Secanell. "Analysis of Low Platinum Loading Thin Polymer Electrolyte Fuel Cell Electrodes Prepared by Inkjet Printing". *Electrochimica Acta*, 2015, Volume. 156, pp. 289. I was responsible for electrode fabrication, testing, data analysis and manuscript writing. K. Domican helped with the fabrication and testing of electrodes. K. Karan provided intellectual guidance in inkjet printing fabrication. S. Bhattacharjee contributed to the manuscript composition and editing. M. Secanell was the supervisory author and contributed with the concept formation, intellectual guidance in fabrication and testing, manuscript composition and editing.

Parts of chapter 3 of this thesis have been accepted for publication to *Journal of Electrochemical Society* as S. Shukla, D. Stanier, M. S. Saha, J, Stumper and M. Secanell. "Analysis of Inkjet Printed PEFC Electrodes with Varying Platinum Loading", *in press*. I was responsible for electrode fabrication, testing, data analysis and manuscript writing. D. Stanier helped with the fabrication and testing of electrodes. J. Stumper and M. Saha, our industrial collaborators, provided intellectual guidance and funding for the research. M. Secanell was the supervisory author and contributed with the concept formation, intellectual guidance in fabrication and testing, manuscript composition and editing.

To my family

Acknowledgements

Table of Contents

List of Tables

List of Figures

Chapter 1

Introduction

1.1 Background and motivation

Fuel cells are energy conversion devices that convert the chemical energy of the supplied fuel to electrical energy by means of electrochemical reactions taking place at the electrode sites. Fuel cells are ideally categorized depending on the type of electrolyte, fuel consumed and operating temperature range. Polymer electrolyte fuel cells (PEFCs) usually operate at temperatures between 40°C and 95°C and are the type of fuel cell that are considered to be a viable alternative to the internal combustion engine for powering future automobiles owing to their high efficiency, quick start-up capabilities and capacity to operate without producing greenhouse-gas emissions when fueled with hydrogen [8, 9].

Figure 1.1 shows the schematics of a single PEFC cell in operation. Collectively referred to as membrane electrode assembly (MEA), the anodic and cathodic electrodes are separated by a polymeric ion exchange membrane. Components (a-d) labeled in the figure are given below.

(a) Bipolar Plates/current collectors

(b) Gas diffusion media

(c) Catalyst layers (CLs)

(d) Polymer electrolyte membrane (PEM)

The bipolar plates consist of flow-field channels through which anodic and cathodic reactants, viz., hydrogen and air (oxidant) are supplied to the cell. The reactants diffuse through the gas diffusion layer to reach the catalyst layer. The gas diffusion layer (GDL) is a porous structure consisting of carbon-fiber materials held together by
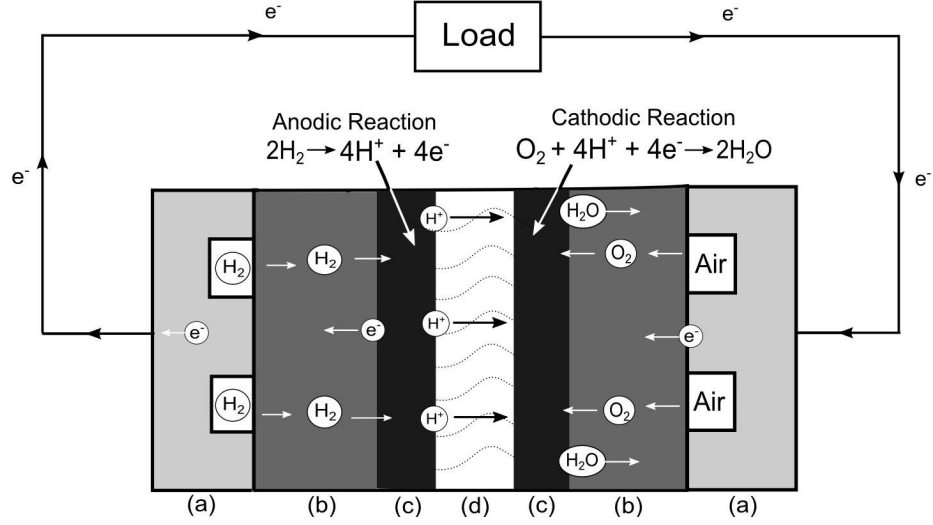
Figure 1.1 – PEFC schematics

a binder [10]. A micro-porous layer (MPL) is usually coated over the GDL to facilitate better water management and to reduce contact resistance with the CL resulting in an improved cell performance [11, 12]. Conventional CLs consist of carbon supported platinum (Pt) as the catalyst [13]. At the anodic CL, hydrogen is split into protons and electrons in presence of the catalyst. The half-cell hydrogen oxidation reaction (HOR) is given as,

$$2H_2 \rightleftharpoons 4H^+ + 4e^- \tag{1.1}$$

The protons (H^+) travel across the PEM, commonly referred to by its commercial name, Nafion, whereas the electrons travel back to the current collectors and across an external electrical circuit towards the cathodic side. The flow of electrons across the external circuit generates an electrical current. At the cathodic side, oxygen diffuses through the GDL, reaching the CL and combines with the protons and electrons to form water by means of the oxygen reduction reaction (ORR), given as,

$$O_2 + 4H^+ + 4e^- \rightleftharpoons 2H_2O \tag{1.2}$$

The overall electrochemical reaction of the PEFC can thus be represented by addition of the anodic and cathodic half-cell reactions and is given as,

$$2H_2 + O_2 \rightleftharpoons 2H_2O \tag{1.3}$$
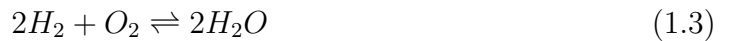
Liquid water formed at the cathode is removed by means of evaporation and permeation across the GDL and out through the gas channels. Water management in PEFCs is critical since too much water may flood the electrode and lead to transport losses whereas too little water may increase the proton transport losses, both of which

may lower the cell performance [13]. For commercial applications, several MEAs are connected in series and used to increase the total voltage and thus, the power output.

The main motivation behind reducing the amount of Pt in the CLs is the high and unstable cost associated with it. Improvements in catalyst and electrode fabrication technologies have resulted in a drop of Pt loading from 28 mg_{Pt}/cm^2 in the 1960s to less than 0.2 mg_{Pt}/cm^2 today [9]. Despite this remarkable progress, Pt electrodes still contribute significantly to the overall cost of the system. A recent study on the cost breakdown of a PEFC stack showed that 34% of its total cost is attributed to the catalyst [14]. Less than 10-20% of the catalyst is however estimated to be utilized during the operation of a conventional CL due to mass and charge transport limitations [15]. Re-designing the CL to improve these transport limitations has the potential to achieve better Pt utilization, i.e., generate more current per gram of catalyst [16]. The CL fabrication process governs its utilization efficiency, microstructure and Pt loading in the electrodes. Thus, a reduction of Pt loading in the CLs without any loss in performance and durability is essential to make this technology a viable energy source.

The main objectives of this work are (a) to improve the drop-on-demand inkjet printing technology for controlled deposition of the catalyst inks to fabricate catalyst coated membranes (CCMs) resulting in a uniform, controlled thickness and lower Pt loading than conventional fabrication techniques and (b) study the effect of Pt loading on fuel cell performance using this fabrication technique.

1.2 Literature Review

1.2.1 Catalyst layer fabrication techniques

A variety of fabrication techniques such as hand painting, spraying, screen-printing, doctor-blade method and sputtering have been used for the catalyst layer deposition. They can be broadly classified into two types, conventional techniques that make use of a carbon supported catalyst ink which is applied to the substrate (membrane or GDL), and vacuum assisted ultra-thin deposition techniques where support-free Pt is directly deposited over the substrate. Comprehensive reviews on PEFC electrode fabrication techniques have been reported by Litster [8] and Wee et al. [17].

1.2.1.1 Conventional fabrication techniques

The work of Wilson and Gottesfeld [18, 19] at Los Alamos National Laboratory in 1992 introduced the thin film fabrication method where the catalyst layer consists of Nafion as a binder unlike the previously used Teflon. The Nafion solution consisted of the ionomer, dispersed in organic solvents that are usually a mixture of isopropanol (IPA) and water. The standard operating protocol (SOP) described for formulating the catalyst ink involved mixing a 5% Nafion solution and 20% Pt/C catalyst with a mixture of water and glycerol [18]. The mixture was sonicated extensively and then applied to a blank Teflon film using hand painting that was hot-pressed over the Nafion membrane [18]. The presence of Nafion in the CL helped to improve protonic transport across the CL and increases the cell performance. The ink formulation protocol has since largely remained unchanged consisting of the Pt/C catalyst particles, Nafion and suitable solvent additives.

Several studies on improving the design, the fabrication process and lowering the amount of Pt in the electrodes have since been reported [20–25]. Kumar et al. [22] report using spraying to deposit the catalyst slurry containing Pt/C particles and Teflon over the diffusion layer. After sintering and impregnating with Nafion, the anodic and cathodic gas diffusion electrodes (GDEs) were hot-pressed over Nafion 117 membrane to form the MEA [22]. Pt loadings of 0.1 mg/cm^2 were achieved [22]. Paganin et al [20] used a mixture of Nafion solution, catalyst particles and IPA as the catalyst ink that was brushed over the carbon diffusion layer to form a GDE. The GDEs were then hot-pressed over the Nafion membrane to form the MEA. It was reported that Pt loading could be reduced to 0.1/0.2 mg/cm^2 in the anode and cathode respectively without a significant loss in the cell performance [20]. Ralph et al. [24] summarized the progresses made at Johnson Matthey and Ballard to develop low Pt loaded electrodes by a high volume production process. Using a similar ink preparation process to that of Wilson [18], electrodes with a Pt loading in the range of 0.1 to 0.7 mg/cm^2 in the cathode and 0.25 mg/cm^2 in the anode were fabricated and tested [24]. Performance and durability testing showed that the lower Pt loading electrodes were able to match the performance of higher loading electrodes used at the time [24].

Qi and Kaufman [2] fabricated GDEs using 20% and 40% Pt/C catalysts to obtain a range of Pt loadings from 0.022 mg/cm^2 to 0.387 mg/cm^2. Based on a parametric study of Pt loading and Nafion content, they report the optimal Pt loading to be dependent on the type of Pt/C catalyst due to changes in the catalyst surface area

and the optimal Nafion loading to be 30 wt% in the CL. More recently, Kriston et al. [26] used a spraying technique to deposit the catalyst ink that was a mixture of Pt/C particles, water, ethanol and the ionomer solution over Nafion 212 membrane. They reported the relationship between the electrochemical active area and Pt loading from 0.05 mg/cm^2 to 0.4 mg/cm^2. The active area decreased with increasing Pt loading due to the decreasing catalyst accessibility [26]. Similar spraying techniques have been used to deposit the catalyst ink either directly over the Nafion membrane [27–29] or over the GDL [30]. Decal transfer is another popular technique where the catalyst slurry is initially applied over a blank polytetrafluoroethylene (PTFE) sheet usually by means of a doctor blade and film applicator, that is then decal-transferred over the membrane by hot-pressing [4, 31–33]. The CL thickness and Pt loading can be controlled by changing the blade height during the film application process. The hot-pressing conditions such as temperature, pressure and duration are also equally important since they are known to affect the cell performance [34, 35]. By knowing the weight difference of the PTFE sheet before and after hot-pressing, the Pt loading is easily measurable in such a method.

Several recent studies have looked into fabrication and characterization of electrodes with reduced Pt loadings [3, 17, 26, 36–44]. Greszler et al. [42] fabricated low loading electrodes using decal transfer method and by using a mixture of catalyzed and catalyzed carbon black particles in order to keep electrode thickness, and thereby transport properties, similar to that of conventional electrodes while reducing the Pt loading. Electrospraying has also been used to fabricate low Pt loading electrodes with loading as low as 0.02 mg/cm^2 [37, 43]. In this case, the CLs produced are highly porous with thickness of 50 μm or greater [37, 43]. Millington et al. [44] report using ultrasonic-spray method for fabricating gas diffusion electrodes with Pt loadings in the range of 0.4 - 0.05 mg/cm^2. The coating thickness was reported to range from 200 nm to 50 μm [44].

Influence of ionomer loading

As discussed earlier, PTFE was replaced by perflurosulfonate ionomer i.e., Nafion as the binding agent in catalyst layers after Wilson et al. [18] showed a considerable improvement in performance with such a technique. The effect of ionomer loading in the CL on cell performance has been examined for conventional electrodes [2, 45–56]. In this case, an optimal Nafion loading usually exists that provides a good trade-off between gas and proton transport. The lack of an optimal value would indicate that neither of these processes are limiting the electrode performance and that the per-

formance is limited by either kinetic or micro-scale losses at catalyst-electrolyte or gas-electrolyte interfaces.

For the conventionally fabricated CLs, the optimal Nafion Loading (NL) has been found to be between 30 - 36 wt%. Lee et al.[46] found the optimal Nafion loading to be 1.9 mg/cm^2 ($\sim$48 wt%) when operating the cell with H_2/O_2. The increase in the ionomer loading led to an increase in the electrochemical active area [46]. Sasikumar et al. [51, 52] found that the optimal NL increased with decreasing Pt loading. They reported the optimal NL to be 20, 40 and 50 wt% for CLs with a Pt loading of 0.5, 0.25 and 0.1 mg/cm^2 respectively and was not a function of the type of membrane used [51]. Based on electrochemical impedance spectroscopy (EIS), Li et al. [45] reported a decrease in cathodic ionic conductivity with increasing Nafion content upto 30 wt%. Paganin et al. [20] report an optimal NL of 1.1 mg/cm^2 (35.5 wt%) for an electrode with a Pt loading of 0.4 mg/cm^2 (20% Pt/C). For a Pt loading of 0.1 mg/cm^2, Passalacqua et al.[54] studied a range of NLs from 14% to 66%. Similar to previous observations, the optimal NL was found to be 33% [54]. In a recent study, using the decal method for CL fabrication with loading of 0.2 mg/cm^2, Xie et al. [48] found the optimal NL to be in the range of 27$\pm$6 wt%. Changing the NL was found to affect the kinetics, ohmic as well as mass-transport regions of the polarization plots. Employing atomic force microscopy to examine the surface structure of the CLs of low and high NLs showed that higher NL resulted in smaller aggregates in the CL [48]. This was attributed to the higher ink volume for the higher NL sample thus improving the dispersion [48].

1.2.1.2 Ultra-thin fabrication techniques

In terms of using vacuum assisted ultra-thin deposition techniques, Hirano et al. [57] first reported using sputter-deposition to fabricate the cathode catalyst layer with Pt loadings from 0.04 - 0.1 mg/cm^2. The cell performance for a Pt loading of 0.1 mg/cm^2 was observed to be similar to that of a standard electrode. Cha et al. [58] used plasma-sputtering to deposit Pt with a loading of 0.043 mg/cm^2 over Nafion membrane. It was found that application of carbon/Nafion ink over the membrane prior to sputtering improving the performance further [58]. Similarly, O'Hayre et al. [59] used sputtering to deposit the Pt over Nafion 117 membrane. They studied the effect of surface roughness of the membrane and the thickness of sputtered catalyst layer on the cell performance. They found that for a smooth membrane surface, the peak performance is achieved when the sputtered film thickness was around 5 nm

(0.014 mg/cm^2). With increased membrane roughness, higher loading is required to get a good performance that was stable over a wide thickness range [59]. They concluded that in order to get a good cell performance, the thickness should be such that the Pt coalesces in a single film [59].

Sputtering of a high-active area substrate was used in 3M's nanostructured thin film (NSTF) electrodes to fabricate electrodes with low loading, high active area and a reduced thickness [60–63]. The NSTF electrodes consisted of densely packed whiskers of a high aspect ratio over which the Pt was sputter deposited [62]. The electrochemical active area and durability was found to be better than other fabrication methods. However, due to the reduced thickness of less than 1 μm and lack of ionomer in the CL, a higher dependence of cell performance on operating conditions was reported [62]. Also, the layers were prone to flooding during wet operating conditions especially at low temperature [62].

Comparison of low Pt loading PEFC electrodes with different fabrication methods

Table 1.1 shows a comparison of the fabrication processes reporting high Pt utilization values and their respective Pt loadings, CL thicknesses and peak power densities. It has to be emphasized that the reactant concentration and operating conditions such as humidity level, cell temperature and pressure has a considerable impact on electrode performance. Higher values of relative humidity (RH) may reduce the ohmic losses in the membrane and electrodes improving the performance at intermediate current densities. Similarly, the operating cell pressure will change the oxygen partial pressure in the cathode affecting the electrode kinetics and mass transport regions. For this reason, most studies reporting high Pt utilization values are performed using oxygen and at a higher backpressure to assess the maximum electrode performance. Also, depending on the type of electrode and its microstructure, changes in operating conditions may not have the same effect on electrode performance. For example, at higher operating RH, the performance in the high current density region may drop for thicker CLs since they are prone to mass transport losses due to flooding, whereas it may increase for electrodes that are thinner in comparison. Since these reported testing conditions vary in literature, an exact comparison of power densities and Pt utilization between the fabrication techniques is not possible and only a qualitative assessment can be made.

Table 1.1 – Literature comparison of various fabrication techniques for low Pt loading electrodes and their cell performance

Sr. No.	Fabrication method	Cathodic Pt loading (mg cm^{-2})	CL thickness (μm)	Operating conditions	Peak power density (W cm^{-2})	Cathodic Pt utilization (kW g$_{Pt}^{-1}$)	Reference
1	Spraying	0.12	1.3 - 5	H$_2$/air (wet) at 20 psig, T$_{cell}$=60°C	0.66	5.5	[36]
2	Sputtering	0.01	0.5	H$_2$/O$_2$ (wet) at 55 psig, T$_{cell}$=80°C	0.4	40	[64]
3	Electrospray	0.012	~50	H$_2$/O$_2$ (dry) at 49 psig, T$_{cell}$=70°C	0.25	20	[50]
4	Ultra-sonic spraying	0.05	0.2 - 50	H$_2$/O$_2$ (wet) at 29 psig, T$_{cell}$=70°C	0.544	10.9	[44]
5	Spraying + sputtering	0.035	1.2	H$_2$/O$_2$ (wet) at 30 psig, T$_{cell}$=80°C	1.02	29	[39]
6	Electrospinning + electrospraying	0.022	~50	H$_2$/O$_2$ (wet) at 30 psig, T$_{cell}$=80°C	0.936	42	[43]
7	Electrospinning	0.029	1.9	H$_2$/Air (wet) at ambient, T$_{cell}$=80°C	0.3	10.5	[40]
8	Hand painting	0.05	3	H$_2$/O$_2$ (wet) at 25 psig, T$_{cell}$=80°C	~0.7	6.25	[65]

From the Table 1.1, it can be seen that the absence of a support material such as carbon for the ultra-thin deposition methods like sputtering produced CLs in the nanometer length scale whereas fabrication techniques like electrospraying produced highly porous electrodes with a thickness of $\sim$50 μm. Based on the table, for most cases, increasing the Pt loading resulted in a reduced Pt utilization, e.g., spray coated electrodes with a Pt loading of 0.12 mg/cm^2 had a peak Pt utilization of 5.5 kW g$_{Pt}^{-1}$.

As discussed earlier, conventional fabrication methods make use of a dispersion of carbon supported catalyst and ionomer that is applied over the substrate by means of doctor blade deposition or spraying; whereas the ultra-thin deposition methods such as sputtering directly deposit the catalyst metal over the substrate [3]. While the operating cost and equipment for conventional fabrication methods are cheaper than the ultra-thin deposition method, CL thickness and Pt loading is relatively greater. Even though the active areas are higher and substrate modification is not required, the conventional ink-based fabrication methods do not provide sufficient control regarding CL uniformity and spatial deposition of catalyst to accurately fabricate thin, low platinum loading electrodes [17]. Based on the discussion above, it would be beneficial to develop a fabrication method with a high deposition control like the ultra-thin methods but that allows the fabrication of conventional Pt/carbon/Nafion structures. One of such methods is the drop-on-demand inkjet printing.

1.2.1.3   Inkjet printed electrode fabrication

Application of inkjet printers for CCM fabrication has progressed little since its introduction in 2007 [5, 66] even though this type of fabrication method does not have the usual drawbacks of conventional or ultra-thin deposition methods. Drop-on-demand technology means that the transfer losses are significantly reduced with respect to spraying; and the flexibility of controlling the Nafion and Pt loading distribution in the CL is much higher than that with other methods. The controlled deposition provided by inkjet printing readily permits the fabrication of thin, low-loading electrodes. Also, because of its higher reproducibility and ability to use multiple cartridges with different ink compositions, this technology can be easily applied to perform ink composition studies. This method can also be applied to large scale commercial fabrication processes as it does not lose its adaptability and versatility when scaled up [3, 5].

Taylor et al. [66] first reported using a commercial thermal inkjet printer to fabricate catalyst layers over the GDLs that were later hot-pressed over the Nafion

membrane. Anodic loadings studied were 0.021 mg/cm^2, 0.138 mg/cm^2 and 0.510 mg/cm^2 whereas the cathodic loading was fixed at 0.5 mg/cm^2 applied using hand painting. Based on the polarization plots, the performance of inkjet printed (IJP) electrodes was found to be slightly better than conventional hand painted electrodes for an anodic Pt loading of 0.51 mg/cm^2. The IJP electrodes with a loading of 0.021 mg/cm^2 showed Pt utilization values of 16 kW/g which was the highest at the time [66]. Towne et al. [5] reported using thermal and piezo-electric office IJP to fabricate CLs directly on the Nafion 117 membrane. A mixture of water, ethylene glycol and isopropanol were used to acquire the desired viscosity and surface tension of the catalyst ink [5]. After eight printed layers, the CL thickness was reported to be 3.2 μm [5]. For a Pt loading of 0.2 mg/cm^2, the IJP cell could reach just 500 mA/cm^2 at a voltage of 0.2 V. Although the performance was lower than commercial MEAs, the study aimed at identifying some key advantages of this fabrication technology such as high flexibility to adapt to MEA pattern and composition, precise deposition control allowing a higher transfer efficiency and a lower Pt loading and thickness [5].

Further improvements in the the IJP methodology and cell performance were carried out by Saha et al. [3, 67, 68] using a research grade Fujifilm Dimatix printer. IPA and glycerol were used as the organic solvents to prepare the catalyst inks and fabricate electrodes having a Pt loading between 0.02 - 0.12 mg/cm^2 and a CL thickness of about 5 μm (after 10 printed layers). The Pt loading was modified by varying the number of printed passes over the membrane which also varied the CL thicknesses [3]. The electrochemical active area was found to be between 33.9 and 45.7 m^2/g for the printed electrodes. The catalyst utilization increased with decreasing CL thickness and the peak power density was reported to be 365 mW/cm^2 for the IJP electrode with a Pt loading of 0.12 mg/cm^2 [3]. The research group also studied fabrication and testing of patterned CLs [69], however difficulties in fabricating sharp patterns over the membrane were identified. Recently, Klingele et al. [70, 71] used the inkjet printing technique to deposit polymer electrolyte dispersion solution over the anodic and cathodic GDEs. These membrane coated GDEs were then assembled together and the surrounding region was sealed using a PTFE subgasket [70]. They report high Pt utilization values of 88 kW/g for a Pt loading of 0.029 mg/cm^2 [71]. Other studies involving inkjet printing include the identification of optimal parameters and the effects of hot-pressing the inkjet printed CCMs by Yazdanpour et al. [72], and deposition of Nafion ionomer onto the catalyst layers using IJP by Wang et al. [73].

The reported literature on IJP electrodes did not study the effect of Nafion load-

ing on the performance of printed CLs. Unlike conventional electrodes, thin, low loading electrodes should have lower macro-scale proton and oxygen transport losses and therefore, it is hypothesized that a lower sensitivity to ionomer loading should be observed. The impact of Nafion loading on the transport and cell performance of CCMs with thin, low loading electrodes might thus be different. Also, lacking in the literature is an in-depth analysis of kinetic parameters such as influence of oxygen partial pressure on Tafel slope, reaction order and quantification of the oxygen transport resistance and its dependence on operating parameters. These studies are essential in order to understand the reason for the performance gap observed with respect to conventional electrodes. In this work, fabrication and characterization of PEFC electrodes has been carried out using inkjet printing [6, 7, 74, 75]. The fabricated electrodes with a Pt loading of 0.026 mg/cm^2, could reach current densities of 5 A/cm^2 and a peak cathodic Pt utilization of almost 48 kW/g$_{Pt}$ when operated with H$_2$/O$_2$ (200 kPaG) [74]. A study of the impact of Nafion loading from 10 wt% to 50 wt% on cell performance was carried out for thin, low Pt loaded IJP electrodes. A comprehensive study of ex-situ and in-situ characterization of the CL microstructure, performance, kinetics, reaction order and local mass transport losses in electrodes with varying Pt loadings from 0.014 to 0.113 mg/cm^2 has also been performed for the case of these inkjet printed electrodes [7]. Further, the effect of electrode patterning and printer resolution has been studied [75].

1.2.2 Oxygen transport resistance

As progress was made towards fabricating electrodes with reduced Pt loading, the performance of the electrodes with low Pt content was observed to be severely degraded in the kinetic and mass transport regions [1, 2, 26, 76]. An optimal value of Pt loading was observed above which performance gains are not very significant [1, 32]. Qi and Kaufman [2] reported the optimal Pt loading to be 0.2 $\pm$ 0.05 mg/cm^2 for the case of 20% Pt/C catalyst and 0.35 $\pm$ 0.05 mg/cm^2 for the case of 40% Pt/C catalyst. A sharp increase in performance was observed when the Pt loading increased from 0.022 mg/cm^2 to 0.083 mg/cm^2 after which the increase in performance substantially reduced for the case of 20% Pt/C catalyst [2]. Kriston et al. [26] reported the relationship between the electrochemical active area and Pt loading from 0.05 mg/cm^2 to 0.4 mg/cm^2. The active area decreased with Pt loading due to the decreasing catalyst utilization [26]. The performance increase was reported to be substantial from 0.05 mg/cm^2 to 0.2 mg/cm^2, but minimal thereafter [26]. Similar performance trends can be observed in other literature on low loading PEFCs [40, 77].

One of the reasons for the reduced performance of low loading electrodes is attributed to a high oxygen mass transport resistance at the reaction site [1, 4, 42, 78–81], whereas the minimal increase in performance at higher loadings can be attributed to a trade off between increased Pt surface area and the increased thickness, i.e., reduced local transport losses and reduced through-plane oxygen transport. The source of this resistance is still under debate and has gained attention in recent years. It is speculated that this transport resistance may arise from oxygen dissolution in the ionomer [82], densification of the ionomer layer near the ionomer/Pt interface [83], and catalyst/oxygen interactions at the catalyst site [79].

The oxygen diffusion process in the cathodic CL includes the bulk diffusion in the gas phase, Knudsen diffusion occurring in the smaller pores of the MPL and CL and diffusion in the water and ionomer films near the catalyst sites. Based on Fick's law, the through-plane molar flux of oxygen, N_{O_2} in the x direction is given by,

$$N_{O_2} = -D_{O_2}^{eff} \frac{\partial c_{O_2}}{\partial x} \tag{1.4}$$

where $D_{O_2}^{eff}$ is the effective diffusion coefficient of oxygen through the diffusion media and c_{O_2} is the oxygen concentration. Assuming the CL to be infinitely thin, equation (1.4) can be re-written as

$$N_{O_2} = D_{O_2}^{eff} \frac{\Delta c_{O_2}}{L} \tag{1.5}$$

where Δc_{O_2} is the concentration gradient of oxygen in the diffusion media and L is the diffusion length. At limiting current, the concentration near the Pt site can be considered to be zero [42, 84]. Using Faraday's relation between the oxygen molar flux and amount of current produced, the equation becomes,

$$N_{O_2} = \frac{i_{lim}}{4F} = \left(\frac{D}{L}\right) c_{O_2} = \frac{c_{O_2}}{R_{O_2}^{total}} \tag{1.6}$$

where i_{lim} is the limiting current, c_{O_2} becomes the gas channel concentration of oxygen and $\left(\frac{D}{L}\right)$ is the reciprocal of the total transport resistance for oxygen, $R_{O_2}^{total}$. Based on this relationship, it is possible to determine $R_{O_2}^{total}$ if the oxygen concentration in the channel, c_{O_2} and the limiting current, i_{lim} are known.

Beuscher [84] obtained the overall oxygen transport resistance by performing limiting current measurements at 70°C using fully humidified reactants, H$_2$ and air at 101 kPa of backpressure. The total transport resistance was reported to be 1.032±2.5%

12

s/cm for the tested samples [84]. By varying the carrier gas from Nitrogen to Helium, it was found that mass transport resistance in the gas diffusion media accounted for 26% of the total resistance whereas majority of the resistance was attributed to the Knudsen and film diffusion through the ionomer and water films in the CL [84]. Baker et al. [78] used limiting current measurements by using reduced oxygen partial pressure and varying the total cell pressure to determine the oxygen transport resistance and separate it into individual components. $R_{O_2}^{total}$ was reported to be 0.9 s/cm for the cell operating at 80°C, 62% RH. Contrary to Beuscher [84], the contribution of transport resistance from channel and diffusion media was found to be greater than 75% [78].

Using a similar method for measuring $R_{O_2}^{total}$, Nonoyama et al. [4] quantified the transport resistance with changing cell temperature, Pt loading and inlet RH. It was found that the transport resistance dropped with increasing RH upto 100%, above which it increased. The drop in $R_{O_2}^{total}$ when RH was below 100% was attributed to changes in the oxygen permeability in the ionomer film. With increasing cell temperature from 50°C to 80°C, $R_{O_2}^{total}$ decreased from ~1.1 s/cm to 0.6 s/cm using 1% O_2/N_2 [4]. Similarly, the transport resistance decreased with increasing Pt loading from 0.1 mg/cm^2 to 0.2 mg/cm^2. After separating $R_{O_2}^{total}$ into individual resistances, a significant contribution was reported to be from the local transport resistance of oxygen through the ionomer film [4].

Greszler et al. [42] studied the oxygen transport resistance over a wide range of Pt loadings from 0.03 mg/cm^2 to 0.4 mg/cm^2 while keeping the CL thickness constant between 11.3 and 13.6 μm. Assuming a negligible through-plane oxygen diffusion in the electrode, the local transport resistance was extracted by plotting $R_{O_2}^{total}$ vs. $1/f$, where f is the roughness factor (cm_{Pt}^2/cm_{CL}^2). The local transport resistance was found to be between 10 - 17 s/cm, similar to the values reported by Ono et al. [85]. Owejan et al. [1] reported that the local transport resistance is a function of both Pt surface area and the Pt particle dispersion in the electrodes. Recent work carried out by Liu et al. [79] to evaluate the transport resistance of oxygen in thin Nafion films in absence of active catalyst particles found no significant changes in the interfacial resistance at the ionomer thickness as thin as 50 nm. It was concluded that the increased resistance observed in presence of the catalyst might be due to interaction between the ionomer and Pt [79].

For the case of inkjet printed electrodes, the oxygen transport resistance has not

been reported in literature. Comparing the performances, it was found that inkjet printed electrodes could not match the performance of spray coated electrodes, even at similar values of Pt loadings at ambient pressure operation. In order to understand whether the performance gap is due to a comparatively higher transport resistance for the inkjet printed electrodes, it was essential to determine these values and compare them to the ones reported for conventionally fabricated electrodes. Details regarding this work can be found in chapter 3.

1.2.3 Fabrication of micro-porous layers

As discussed earlier, the main purpose of the MPL is to help in reducing the contact resistance between the MPL and CL and improving transport of reactants by removal of water formed in the CL [11, 12]. Conventionally, the MPL is fabricated over the GDL surface by means of brush painting or spraying [86–89]. PTFE is used during the MPL ink preparation to impart hydrophobicity to the layer [86].

Park et al. [90, 91] sprayed a mixture of Vulcan XC72R carbon black and polyvinylidene fluoride (PVDF) dispersed in dimethyl formamide (DMF) directly over a commercial CCM (Gore PRIMEA). The reported thickness of the fabricated MPLs was between 50 and 100 μm based on SEM imaging [91]. PVDF was used instead of PTFE due to its lower sintering temperature, since exposure to higher temperature during this process may damage the membrane [90]. Performance comparison between the two MPL thicknesses of 50μm and 100μm showed a higher current density for the thinner MPL in the mass transport region [91].

Kitahara et al. [92–95] studied the effect of hydrophilic MPL by replacing PTFE with polyvinyl alcohol (PVA) as the MPL binder. A commercial CCM from Gore (PRIMEA 5580) with a Pt loading of 0.4 mg/cm^2 and a CL thickness of 30 μm was used for testing [92]. The hydrophilic MPL coating over a hydrophobic MPL (double MPL) helped in retaining water and improving the cell performance during low operating RH. The group studied the effect of hydrophilic coating thickness and PVA/PTFE content in the hydrophilic/hydrophobic MPLs. They report an optimal hydrophilic MPL thickness of 5μm and a PVF and PTFE content of 5 wt% and 10-40 wt% respectively [92].

Ahn et al. [96] used Nafion ionomer during their carbon ink formulation in order to fabricate MPLs with the hydrophilic polymer. An improvement in the cell perfor-

mance and lowering of ohmic losses was observed with the presence of Nafion based MPL on the cathodic side as compared to the PTFE based MPL [96]. Similarly, Tanuma [97] used a mixture of water, ethanol and Flemion ionomer dispersion to obtain hydrophilic MPL coating over the GDL substrate. A performance improvement at dry operating condition of 30% RH, 80°C was reported when using the hydrophilic ionomer based MPL [97].

The effect of MPL fabrication over thin, low Pt loading CCMs has not been reported in the literature. Further, only Park et al. [90, 91] have reported directly depositing the MPL over a CCM using conventional spraying technique. The reported MPL thickness however was 50μm or greater. It was observed that reducing the MPL thickness from 100μm to 50 μm resulted in a better performance in the high current density region [91]. In this work, Nafion based carbon ink is fabricated directly over the CL by means of inkjet printing to form an electrode coated membrane (ECM). Due to the fabrication method used, a controlled low thickness of the CL and MPL is achieved. The results show a lower transport loss for the ECM compared to a standard CCM. Further details can be found in chapter 4.

1.2.4 Role of dispersion solvents in catalyst inks

Most CL fabrication methods for PEFCs are based on wet deposition of a colloidal dispersion i.e., the catalyst ink onto either a membrane or a gas diffusion electrode [8]. The catalyst ink is usually a mixture of carbon supported platinum particles, Nafion ionomer and organic dispersion media. The ink preparation and fabrication process can have a substantial impact on the fuel cell performance since it governs the microstructure of the CL [8]. Poor Pt utilization occurs due to the transport losses taking place at the macro and micro-scale of the CL [98, 99]. The structure of the aggregate present in the CL and ionomer distribution will determine the extent of the micro-scale transport losses.

The aggregate size in the CL can be thought to be a function of aggregate size in the catalyst ink, which is the first step for most fabrication methods and the particle-substrate, particle-particle and particle-dispersion media interactions during drying of the layer after deposition. It is therefore important to have a well dispersed catalyst ink and prevent the formation of larger aggregates. Another advantage of having a well dispersed catalyst ink is increasing the storage time of the inks for larger commercial fabrication processes. Even though the importance of appropriate

ink recipes has been recognized, very few studies have aimed at understanding the impact of dispersion media (DM) on the ink stability and dispersion. The type of dispersion medium, particle concentration and ionomer content of the ink will dictate its stability and particle aggregate size. This in turn will dictate the viscosity and surface tension of the ink, and ultimately, performance of the electrode. The deposition efficiency of fabrication techniques such as inkjet printing highly rely on aggregate size in the catalyst ink, as a higher aggregate size may block the cartridge nozzles and prevent the ink from jetting [100].

The effect of DM selection on the electrode performance has been based on whether Nafion ionomer will form a solution, colloidal suspension or precipitate [30, 101–109]. Uchida et al. [101, 102] first proposed the relationship between the dielectric constant of the DM on the state of Nafion chains in the ink. The ionomer formed a solution, colloid or precipitate depending on whether the dielectric constant of the DM, $\epsilon >$10, 3$< \epsilon >$10 or $\epsilon <$3 respectively. This has since been used as a benchmark for categorizing the dispersion media and determination of their effect on cell performance [30, 104, 109]. Shin et al. [30] compared the effect of DM and concluded that the DM, where Nafion is present in a colloidal state resulted in a higher cell performance. Yang et al. [104] on the other hand found the cell performance to be better when Nafion was present in the solution form. These discrepancies might be caused due to the different substrates used in the two cases since the optimal aggregate size when depositing on carbon paper might be different than when depositing on a membrane. Malek et al. [110] and Xiao et al. [111] use coarse-grained molecular dynamic (CGMD) simulations to study the interaction of carbon, Nafion and the DM. Malek [110] reported an increasing agglomerate size with decreasing dielectric constant of the solvent which was validated experimentally by measuring the catalyst particle size in a range of solvents. Although the model predictions for the aggregate size varied quantitatively, the qualitative assessment was confirmed [110].

In spite of being one of the major factors in the ink preparation process, the DM or solvent selection is done either by a simplistic empirical approach or by using complex molecular dynamic simulations. A simple semi-empirical model predicting the differences in particle-particle interactions and ink stability with changing DM would be useful to determine the "goodness" of a particular solvent. A part of this work involves implementing a modified form of the Derjaguin-Landau-Verwey-Overbeek (DLVO) model to determine the interaction energy between the interacting colloidal particles and subsequently the stability ratio for different non-aqueous dispersion me-

dia. Quantification of settling time for the aggregates in the ink is carried out based on population balancing assuming a diffusion limited aggregation process [100]. Experimental validation using carbon based inks in IPA, ethyl acetate, ethanol and methanol is done using transient stability tests based on visual inspection and dynamic light scattering (DLS) to determine the particle size. It is believed that this model may serve as a foundation upon which more complex physics of particle interactions such as the effect of ionomer chains (steric interactions) can be implemented. Details regarding this work can be found in chapter 6.

1.3   Contributions

The main contributions of this work are in the areas utilizing inkjet printing for fabrication of electrodes with a controlled loading and thickness and the effect of Pt loading on the fuel cell performance. Such improvements in the electrode fabrication for lowering the Pt content and improving the performance are essential if PEFC technology is to achieve a full commercialization. The present work contributes to the field in the following areas,

1. Study the effect of Nafion loading on thin, low Pt loading inkjet printed electrodes

2. Analysis of kinetic parameters and effect of oxygen partial pressure with varying Pt loading for inkjet printed electrodes

3. Measurement of local oxygen transport resistance in inkjet printed electrodes using limiting current density experiments

4. Development of new electrode architecture where both CL and MPL are deposited over the Nafion membrane using inkjet printing

5. Developing a simple semi-empirical model based on colloidal science to understand the relationship between the dispersion solvents and particle stability in the catalyst inks

1.4   Thesis Outline

This thesis has been divided into seven chapters. Chapter 1 gives a brief introduction to the PEFC technology and a broad motivation for the work. An extensive literature review on catalyst layer fabrication methods, inkjet printing technology and oxygen

transport resistance in low Pt loading electrodes is presented along with a brief literature review and motivation to study dispersion media on the ink stability. Chapter 1 also includes the main contributions of the work. Chapter 2 includes details regarding catalyst ink SOP, inkjet printed fabrication process and results on the effect of cell performance on ionomer loading. Chapter 3 presents a detailed kinetic analysis and evaluation of transport resistance for electrodes with varying Pt loading. Chapter 4 talks about fabrication and characterization of novel electrode coated membrane structures. Chapter 5 discusses the printer resolution and feasibility of patterned electrode structures. Chapter 6 gives details regarding the developed colloidal science based model for particle interactions in order to rationalize dispersion solvent selection. Finally, chapter 7 summarizes the contributions of the work and possible future avenues of research in this field.

Chapter 2

Fabrication and characterization of thin, low loading electrodes and effect of ionomer loading

This chapter describes in detail the inkjet printed electrode fabrication and characterization process. Section 2.1 describes the materials and methods used for ink formulation and the electrode fabrication process using inkjet printing. CLs having Nafion loadings from 10 wt% to 50 wt% were fabricated and tested in order to determine an optimal ionomer content in the electrodes. This section also describes the various ex-situ and in-situ characterization techniques used for testing the electrodes. Section 2.2 includes results obtained from the electrode characterization. This includes comparison of CL thicknesses, active areas and performance for the different Nafion loading CCMs. A conventionally fabricated spray coated electrode is tested at the same conditions and the results are compared.

2.1 Materials and methods

2.1.1 Ink formulation

The catalyst ink preparation was done using a similar procedure to that presented by Saha et al. [3]. 37.5 mg of 20 wt% Pt on Vulcan XC carbon black (Alfa-Aesar) was mixed with 1.8 to 2.5 g of isopropanol (IPA), 0.5 g of glycerol (Fisher Scientific) and desired amounts of 5 wt% Nafion ionomer from Ion Power Inc. (1100 equivalent wt.) depending upon the required NL in the CCM. The amount of ionomer to be added was calculated using the following relation

---

$$Y_{el} = \frac{m_N}{m_N + m_{Pt/C}} \qquad (2.1)$$

where Y_{el} is the Nafion Loading (NL) in the electrodes, m_N is the amount of solid Nafion to be added and $m_{Pt/C}$ is the amount of catalyst added. Addition of glycerol to the ink helps to increase its viscosity and facilitate proper jetting during the fabrication process. Due to their lower boiling point than glycerol, ethylene glycol (EG) and propylene glycol (PG) have also been used instead of glycerol to facilitate faster drying of the electrodes. Fabrication and testing of inkjet printed electrodes using EG and PG as the solvents will be discussed in detail later in chapters 3 and 4. In order to maintain a fixed ink volume irrespective of the NL, the IPA volume was altered to account for the changing amounts of ionomer solution required to achieve different Nafion loadings. The fixed volume irrespective of the NL ensures a fixed particle concentration in the inks which corresponds to a fixed value of Pt loading. The Nafion ionomer was added drop-wise to the ink while it was being sonicated in a water bath (Branson 1800) having an output frequency of 40 kHz, at room temperature since such a technique has been known to improve the cell performance [102]. Once Pt/C, ionomer and dispersion media were mixed, the ink was placed in a waterbath and treated using a probe sonicator (Qsonica S-4000) at frequency of 20 kHz for 15 minutes at an amplitude of 20% to break up the aggregates and homogenize the suspension. A water-bath helped to maintain the ink temperature constant during the ultrasonic treatment since a temperature rise in the catalyst ink may reduce the process efficiency as reported by Pollet [112]. The ink was degassed in the water bath for 60 minutes and left on the magnetic stirrer at a speed of 350 rpm for further use. Degassing was found to be an important step to improve the drop deposition efficiency and reduce nozzle clogging. Figure 2.1 shows a flow chart of the catalyst ink preparation that was followed.

The dispersion media in the ionomer solution which is primarily a mixture of water and IPA will change the ink volume depending on its NL. In order to maintain the ink volume constant irrespective of the NL, IPA content was varied. Table 2.1 gives the composition of catalyst ink for various NLs. The weight of IPA to be added for each type of NL is given. Thus, considering 30 wt% NL ink as the base-case, the amount of IPA deficiency/surplus in the 10, 20, 40 and 50 wt% NL samples is calculated and the amount of IPA is added accordingly.

As an example, the amount of ionomer to be added to the ink for the case of 40
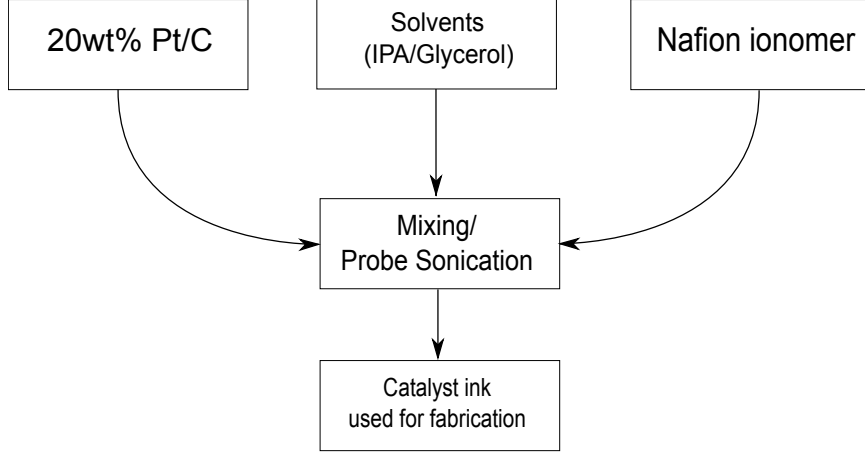
Figure 2.1 – Flowchart followed for the catalyst ink formulation

wt% NL calculated using Equation (2.1) is 500 mg. This amount contains 5% Nafion and 95% dispersion media, i.e., 475 mg of dispersion media. Considering 30 wt% NL as the base-case, the surplus amount of dispersion media present in the ionomer solution is 475 - 305 = 170 mg. This amount of IPA was thus added, taking into account this surplus dispersion media already present in the ink.

Table 2.1 – Ink composition for various NLs. The amount of IPA to be added was calculated based on the amount of ionomer added

Nafion Loading (%)	Ionomer solution added (mg)	Dispersion media in the ionomer solution (mg)	IPA surplus/deficient (mg)	Final IPA added (g)
10	83.3	79.14	225(deficiency)	2.5
20	187.5	178.125	127 (deficiency)	2.41
30	321	305	0	2.28
40	500	475	170(surplus)	2.11
50	750	712.5	407.5(surplus)	1.873

2.1.2 Electrode fabrication

A commercially available piezo-electric printer, Dimatix 2831, Fujifilm Inc (Figure 2.2) consisting of programmable piezo-voltages for individual nozzles was used for CCM fabrication of both the anodic and cathodic electrodes.

Figure 2.3 shows the nozzle head schematics. A pressure pulse is induced inside the ink-cavity by a mechanical actuator made of piezoelectric material [113]. A rapid
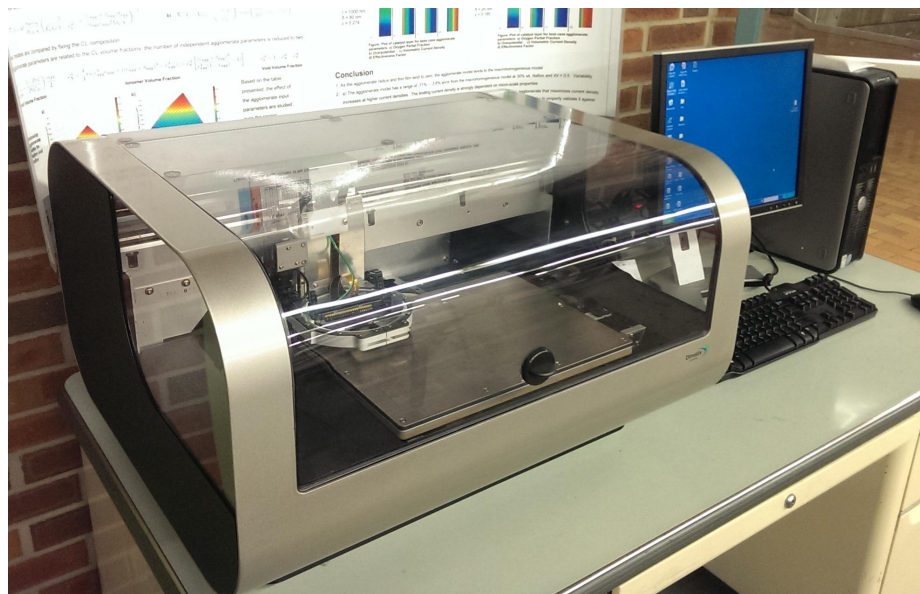
Figure 2.2 – Dimatix-2831 piezo-electric inkjet printer used for electrode fabrication

change in volume inside the cavity forces the ink to jet through the nozzle and draw more ink from the reservoir.
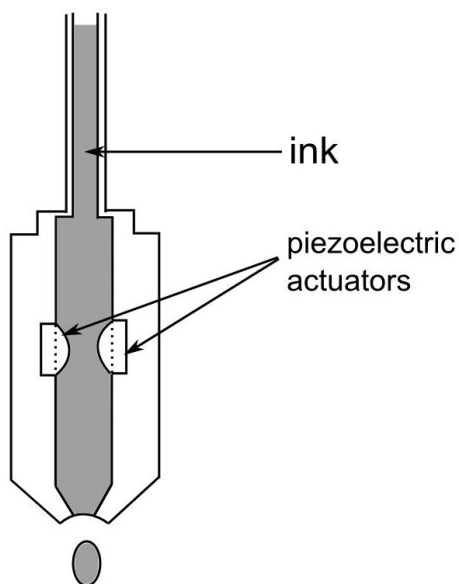
Figure 2.3 – Piezo-electric drop-on-demand nozzle schematics showing jetting of the ink drop by actuating the piezoelectric material

The catalyst ink prepared using the methodology described above was used to

fill up the cartridge and jetted over a Nafion membrane (NR-211 from Ion Power, as received) acting as a substrate. The cartridge (DMC-11610) used for this work had a volume capacity of 1.5 ml. Figure 2.4 shows the image of the cartridge and cartridge head containing the nozzles. The drops were jetted from a nozzle having a diameter of 21.5 μm with an individual drop volume of 10 pL. After completion of the fabrication process, the cartridge was cleaned using bath-sonication and stored for re-use. Figure 2.5 shows a snapshot of 6 nozzles in action while jetting the ink. The ink present inside the ink-cavity had to be incompressible in order for it to eject out of the nozzle head. Presence of air bubbles caused some of the nozzles to stop working. Even if the ink had been degassed before filling it in the cartridge, shaking of the ink due to the motion of the printer head during printing may introduce some air bubbles in the ink. One solution is to intermittently *purge* the ink on a cleaning pad. Alternatively, making the ink more viscous by increasing the amount of viscous solvents during its preparation may help to a certain extent at the expense of increased drying time.
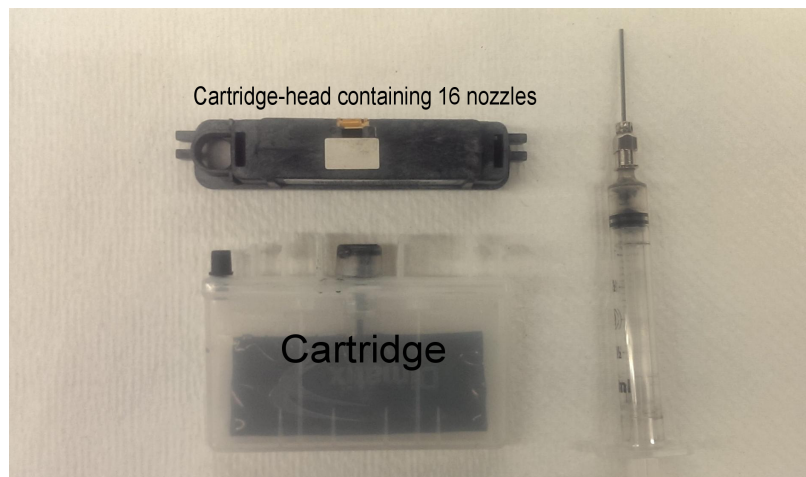
Figure 2.4 – Cartridge and cartridge head containing the nozzles

Five passes of 5 cm^2 were printed over the membrane with a time interval of 20 seconds between the passes and a drop spacing of 20 μm for all the tested samples. The number of printer passes can be varied depending upon the desired Pt loading and CL thickness. Figure 2.6 shows the versatility of the inkjet printing method during electrode deposition. Fabrication and testing of CCMs having larger active areas such as 25 cm^2 and patterned electrodes have also been achieved using this technique. Results obtained from testing of such patterned electrodes will be discussed later in chapter 5.
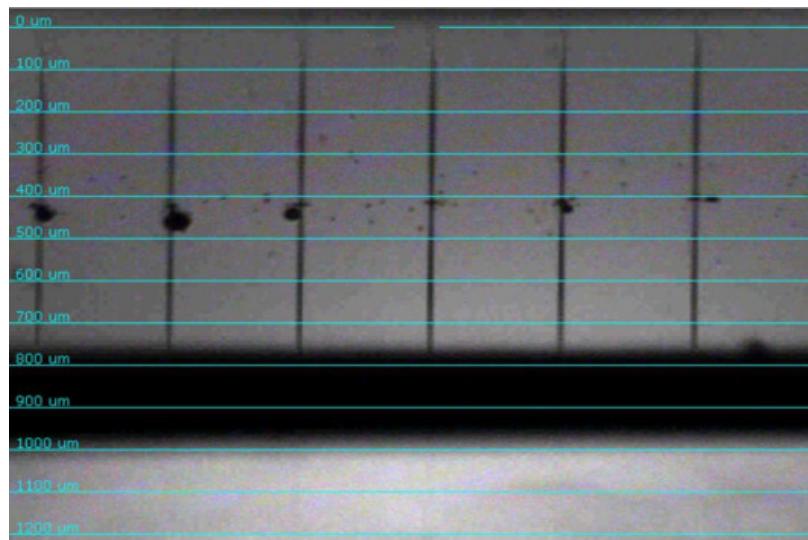
Figure 2.5 – Ink-jetting of the drops from the nozzles in action
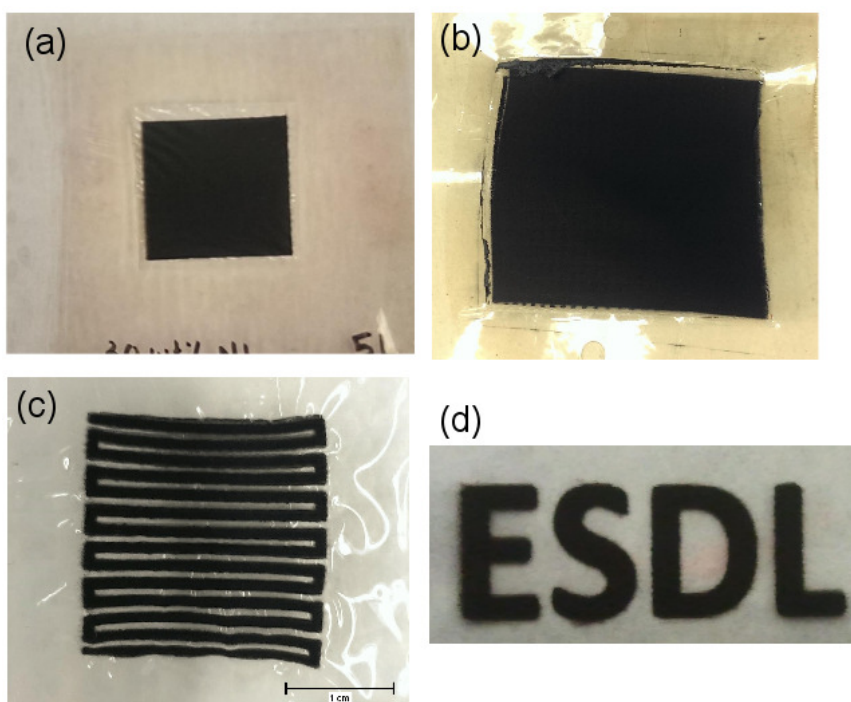
Figure 2.6 – Fabricated CCMs using inkjet printing (a) 5 cm^2 electrode (b) 25 cm^2 electrode (c) patterned electrode depicting the flow-channels (d) Energy Systems Design Lab logo

In order to assess the cathodic performance, the NL for anodic electrodes were kept fixed at 30 wt% while the NL for cathodic electrodes were varied from 10 to 50 wt%. After both the electrodes were fabricated, the CCM was dried in the oven at

80±2°C overnight, boiled in deionized water for 3 hours, dried and stored for further use. Pt loading was measured using X-ray fluorescence (XRF) technique (Thermo Scientific, Niton XL3t) [68] and gravimetric analysis (GA). For GA, CL was fabricated on a pre-weighed Aluminum foil. It was dried for 3 hours at 300°C to remove the solvents and weighed again. The weight difference was used to calculate the amount of Pt in the CL. For comparison, a spray-coated electrode is used. The spray-coated electrode had a NL of 30 wt% and used a 46 wt% Pt/C catalyst (TEC10E50E) over NRE-211 membrane [27].

2.1.3   Electrode micro-structure characterization

The CL morphology and thickness was determined using a scanning electron microscope (JEOL 6301 F - field emission SEM). The samples were freeze-fractured in liquid nitrogen before mounting them over the SEM stubs. Mean thickness was reported with a standard deviation from multiple readings from different CL locations. Electrode porosity was estimated based on the ink composition and the measured CL thickness.

Density of carbon black needed for estimation of CL porosity was evaluated by using a mercury intrusion porosimeter (Poremaster 33, Quantachrome Instruments). Pre-weighed sample of Vulcan XC-72 carbon black (Fuel Cell Store) was dried in the oven overnight at 80°C and filled in the bulb of the glass penetrometer tube having a stem volume of 0.5 cm^3. The penetrometer was then filled with mercury and the mercury pressure was increased to a maximum of 227.5 MPa. With increasing pressure, mercury intruded into the pores of the carbon sample. The pore radius, r (cm) is estimated using the Washburn equation given as [114]

$$r = -2\frac{\gamma cos(\theta)}{p} \tag{2.2}$$

Here, p is the applied pressure (dyne/cm^2), γ and θ are the surface tension and contact angle of mercury taken as 480 dyne/cm and 140° respectively [114].

The volume of the sample was calculated by subtracting the volume of mercury in the penetrometer without the sample by the volume of mercury after its intrusion into the sample pores. Figure 2.7 shows the pore size distribution (PSD) of the vulcan carbon from four independent experiments that were carried out. The plot shows the logarithmic pore distribution, $\frac{DX}{Dln(r)}$ plotted with the pore radius, r. The term $\frac{DX}{Dln(r)}$
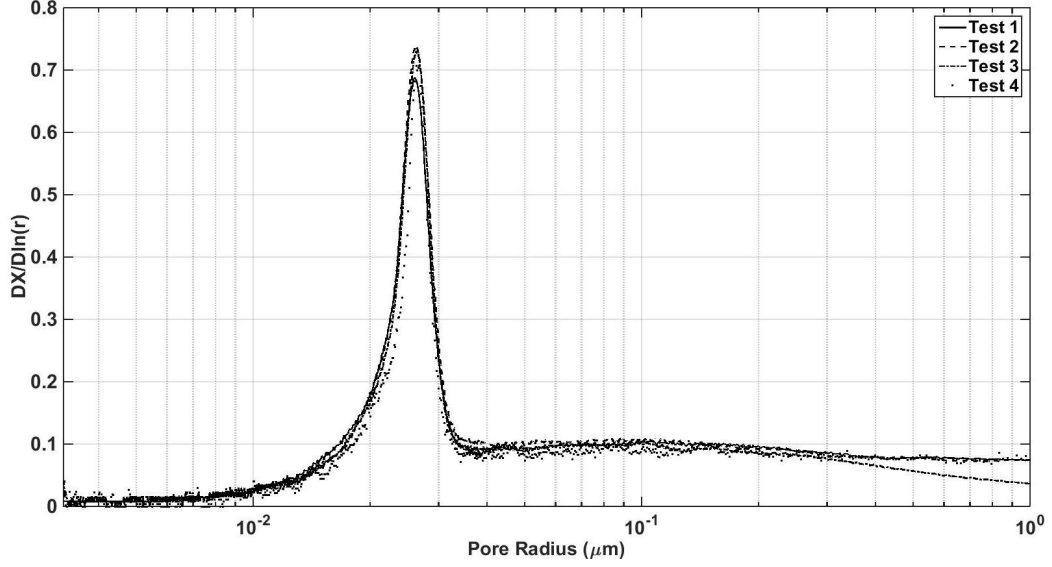
Figure 2.7 – Pore size distribution of Vulcan XC-72 carbon black using mercury intrusion porosimetry from four independent tests. Density of carbon based on the MIP data is $1.69{\pm}0.21$ g/cm^3

was calculated by using the following expression [114]

$$\frac{DX}{Dln(r)} = \frac{(V_i - V_{i-1})/V_{pore}}{ln(p_i) - ln(p_{i-1})} \tag{2.3}$$

where X is the cumulative pore volume fraction, V_i is the intruded volume of mercury into the sample upto pressure p_i and V_{pore} is the total intruded volume of mercury. A good consistency between the measured PSDs for the four experiments suggests good repeatability. A peak between 20-30 nm indicates that the size of the inter-particle pores for carbon black are in this size range. Assuming the density of mercury to be 13.69 g/cm^3, the density value averaged from the four tests was found to be $1.69{\pm}0.21$ g/cm^3. The maximum pressure of 227.5 MPa corresponds to a minimum pore diameter of around 4 nm. Pores smaller than 4 nm are unlikely to contribute to mass transport. Therefore, this estimate for density is used for calculating the electrode porosity since this value might be more representative of the actual available macro-pore network inside the catalyst layers.

2.1.4 Electrode electrochemical characterization

Electrochemical impedance spectroscopy (EIS), cyclic voltammetry (CV) and chronoamperametry tests were performed for quantification of the ionic resistance for the electrodes, active area and hydrogen crossover respectively. A potentiostat (VersaStat 4, Princeton Applied Research) was used for the electrochemical measurements. The

26

anode (hydrogen electrode) served as the reference and counter electrode while the cathode was the working electrode.

EIS was implemented to determine the protonic resistance through the electrode. 0.1 lpm of dry N_2 was fed through the cathode and 0.1 lpm of hydrogen at 50% RH was fed on the anodic side with a cell temperature maintained at 80°C. The reason for using dry gas at the cathode was to increase the electrode resistance since at higher humidity, the expected 45° line could not be observed [115]. The impedance spectra was obtained at 0.5 V (DC) by sweeping frequencies in the range of 100 Hz to 25 kHz with an amplitude of 10 mV. Galvanostatic EIS was implemented to determine the charge transfer resistance for the electrodes. For this, 50% humidified H_2/air were fed to the cell and the impedance spectra was obtained from 50 mA to 1 A at an amplitude of 10 mA RMS and a frequency range of 1 Hz to 10 kHz.

For CV and crossover tests, the cell temperature was kept at 30°C. Anode and working electrode (cathode) were fed with fully humidified hydrogen and nitrogen at the rate of 0.2 lpm and 0.005 lpm, respectively. The CV was performed by scanning the potential between 70 mV and 800 mV versus the reversible hydrogen electrode at a scan rate of 40 mV/s [74, 115]. 10 cycles of voltage scanning were performed. The initial two cycles were left out since in these cases, the voltage values differed from the other cycles and an average voltage from the remaining cycles was determined. The area of the CV plot representing hydrogen desorption, i.e., the region from 0.35 V to 0.1 V, was evaluated using trapezoidal rule and the electrochemical active area (ECA) was calculated using [115, 116]

$$ECA(\text{m}^2_{Pt}/\text{g}_{Pt}) = \frac{area(\text{mA/cm}^2 \times \text{V})}{0.210(\text{mC/cm}^2) \times Scan\ rate(\text{V/s}) \times Pt\ loading(\text{g/cm}^2)} \times 10^{-4}$$
(2.4)

where 0.210 mC/cm^2 Pt is the commonly assumed charge to remove a mono-layer of protons on Pt.

For crossover, chronoamperometry experiments at potentials upto 0.5 V (200 seconds per voltage) were performed and the current produced was observed over time at a cell temperature of 30°C using fully humidified hydrogen and nitrogen at the rate of 0.2 lpm and 0.005 lpm respectively. Improper handling of the membrane during its fabrication and assembly will result in formation of pinholes through which the hydrogen crosses over during the fuel cell operation. Increased crossover results in a lower fuel cell efficiency by increasing its overpotential [117]. The flux of hydrogen

crossing over (J_{x-over}) can be calculated at a specific voltage based on Faraday's law as follows [116]

$$J_{x-over} = \frac{I}{n.F} \tag{2.5}$$

where I is the crossover current produced at a specific voltage, n is the number of electrons for hydrogen oxidation reaction (2) and F is the Faraday constant (96485 C/mol). For a pristine cell, the measured crossover current remains at a constant low value whereas for a cell with pinholes, the crossover current increases over time with increasing voltage.

2.1.5 MEA assembly and testing

Galvanostatic polarization curves for the cell were obtained using a fuel cell test station (850e with back pressure unit, Scribner Associates). A fuel cell hardware with a 5 cm^2 single serpentine channel was used. Figure 2.8 shows the anodic and cathodic single serpentine channel bipolar plates used for the testing with marked inlets and outlets for the reactant gases. Type of channel configuration will affect the cell performance, especially at high overpotentials due to variations in the internal pressure gradients which will affect the oxygen partial pressure. Apart from single serpentine, parallel channel configuration has also been used for testing and will be discussed in the later chapters. The fabricated CCM was laminated using 3 mil lamination sheets to facilitate ease of handling and prevent membrane damage. Anodic and cathodic sides were properly marked prior to assembly as seen from Figure 2.6 (a). This is important especially when the Pt and Nafion loadings varied between the anodic and cathodic electrodes. The CCM was then sandwiched between two gas diffusion layers (GDLs) having a microporous layer (24BC, SGL SIGRACET) and 5 mil silicone gaskets. The thickness of the GDL was 235 μm. Figure 2.9 shows the cell assembly prior to connecting it to the test station for electrode testing. 48 inch-lb of torque was applied to each bolt and they were tightened in a star pattern to ensure pressure uniformity across the electrode surface. A pressure film (Prescale LLW, Fujifilm) was used to test for homogeneous compression of the membrane electrode assembly (MEA). Figure 2.10 shows the single cell assembly attached to the test station for controlling the reactant flow-rates, cell temperature and load variations. Once assembled, the cell was initially conditioned with H$_2$/air at 0.2/0.4 lpm respectively at 80% humidity and 80°C until the voltage at various currents reached steady state. The current was incrementally increased from 0.1, 0.25, 0.5, 1, 2, 3, 4 and 5 A with 1 hour per point upto 0.5 A, and 2 hours per point after that, with the total conditioning

duration for the cell to be around 13 hours. Conditioning ensured that the membrane was adequately humidified prior to testing. More details regarding the conditioning process is given in Appendix A.

The tests were then recorded at a temperature of 80°C and relative humidity (RH) values of 50%, 70% and 90% for the cell operating with hydrogen and air at ambient pressure. RH was varied by changing the temperature of the anodic and cathodic reactants passing through the humidifier while maintaining the cell temperature. Both the reactant gases were maintained at the same pressure while testing at higher system pressures. Polarization plots were also obtained using pure oxygen at the cathode. The reactants, i.e compressed air (ultra zero), hydrogen, oxygen and nitrogen (UHP 5.0) were obtained from Praxair. 1% oxygen and 10% oxygen were also used as reactants in order to vary the partial pressure of oxygen needed to extract the value of reaction order (γ). Polarization plots were obtained galvanostatically at a scan rate of 0.1 A/minute. 10 plots (5 forward and 5 backward sweeps) were obtained for each of the aforementioned conditions and an average curve showing a standard deviation of the five forward plots was obtained.

(a) (b)
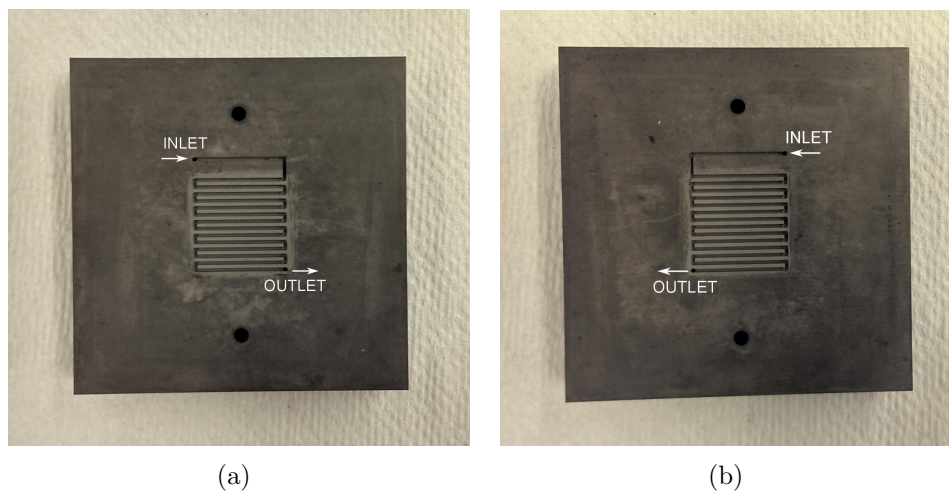
Figure 2.8 – Anodic and cathodic single serpentine bipolar plates

2.2   Results and discussion

5 cm^2 CCMs with NL of 10, 20, 30, 40 and 50 wt% for the cathodic electrodes were fabricated on a membrane using the inkjet printer. Each printed pass had a Pt loading of around 5 μg/cm^2. 5 passes were printed for both anode and cathode electrodes.
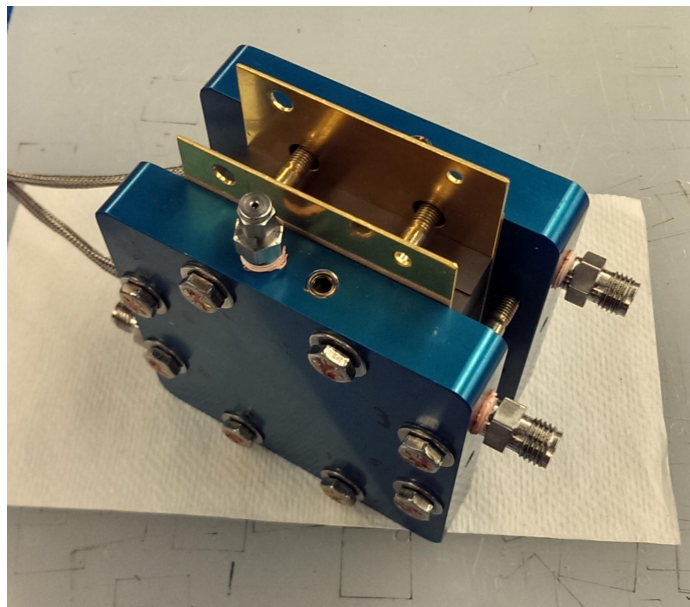
Figure 2.9 – Single cell assembly

Each electrode had a catalyst loading in the range of 0.025 - 0.03 $\text{mg}_{Pt}/\text{cm}^2$. Characterization of the CCMs using ex-situ SEM imaging and and in-situ electrochemical methods are discussed in this section. For comparison, a spray coated CCM having Pt loading of $0.1/0.4 \ \text{mg}_{Pt}/\text{cm}^2$ (anode/cathode) was also tested at similar conditions and results are compared.

In order to assess repeatability of the fabrication and testing process, two sets of 5 cm^2 CCMs of 20 wt% NL and 30 wt% NL were fabricated, assembled in a fuel cell using the same gaskets and GDL materials and tested. The change in current density for the two samples at 0.5 V was around 30 mA/cm^2 for the case of 30 wt% NL and 60 mA/cm^2 for the case of 20 wt% NL. The repeatability was considered acceptable given the uncertainties associated with fabrication, cell assembly and testing. Under the assumption that the repeatability for other cases will be similar and due to time restrictions, only one sample each was fabricated and tested for the remaining cases of 10 wt% NL, 40 wt% NL and 50 wt% NL and the results are reported.

2.2.1 Electrode micro-structure

Micro-structure characterization was performed using SEM imaging of the CLs and ink composition analysis.

Figure 2.10 – Fuel cell test station with the attached cell assembly

2.2.1.1 SEM analysis

Figure 2.11 (a) shows an SEM image of the top surface for the inkjet printed CCM. As seen in the Figure 2.11 (a), no micro-cracks were observed on the fabricated layers. Figures 2.11 (b-d) show the top views of CCMs with different NL. The size of the particles and aggregates appears to increase with higher NL. This is in contrast to Xie et al. [48] who report a decrease in aggregate size with increasing ionomer content. The ink preparation method used here might explain this discrepancy. Xie et al. [48] state that the increased ink volume for higher ionomer loadings result in more dispersed catalyst aggregates. In this work however, the solid content (Pt/C + ionomer) to dispersion media ratio was kept constant. Increase in aggregate size

might be due to a higher Nafion film thickness around the particles for 50 wt% NL CCM.

Figure 2.12 shows a proposed schematic of the effect of NL on the microstructure. As the NL increases, the thickness of the ionomer film around the particles increases and previous carbon particles that appeared as individual particles start to form larger aggregates. Assuming the catalyst layer can be idealized as a collection of carbon particles bound and completely surrounded by ionomer, the thin film surrounding the ionomer can be estimated using the geometrical relationship presented by Secanell et al. [98]. Assuming an agglomerate size of 150 nm and that 10% of the volume of the agglomerates is taken by ionomer, the thin film surrounding the agglomerate is estimated at 1.10, 8.28, 16.64, 26.64 and 38.97 nm in thickness for 10, 20, 30, 40 and 50 wt% NL CCMs respectively. The increase in Nafion film thickness and coalescence between agglomerates would increase local (micro-scale) mass transport resistances as some Pt particles are now away from the gas/ionomer interface. Further as the NL increases, the secondary pore size and porosity decreases thereby reducing the gas transport of the electrode also at the macro-scale [101]. Both processes should result in a decrease in cell performance at high NL. For the thin electrodes studied, i.e., 1-2 μm however, macro-scale transport losses should be minimized unless complete blockage of the secondary pores takes place. Increased micro-scale losses however should be observable since they increase with respect to conventional electrodes because, at the same current density, the reduced number of active sites in this low loading electrodes will result in higher reaction rates per platinum site.

CL thickness was determined using image analysis of the SEM images using *ImageJ* software. CL thicknesses for each NL sample were measured from 15 locations of the SEM images and an average value with the standard deviation is reported. Figure 2.13 shows the freeze-fractured cross-section SEM of CCMs. A relatively uniform layer and a good adhesion with the membrane is observed. Insignificant change in the CL thickness is observed for the NLs tested. Table 2.2 gives the values for the measured CL thicknesses for the various Nafion loading samples. CL thicknesses were measured to be between 1.5 and 2 μm. The CL thickness of the 10 wt% NL sample is estimated to be also in the range of 1.5 - 2 μm. The thickness for the spray coated sample is estimated to be approximately 10 μm.
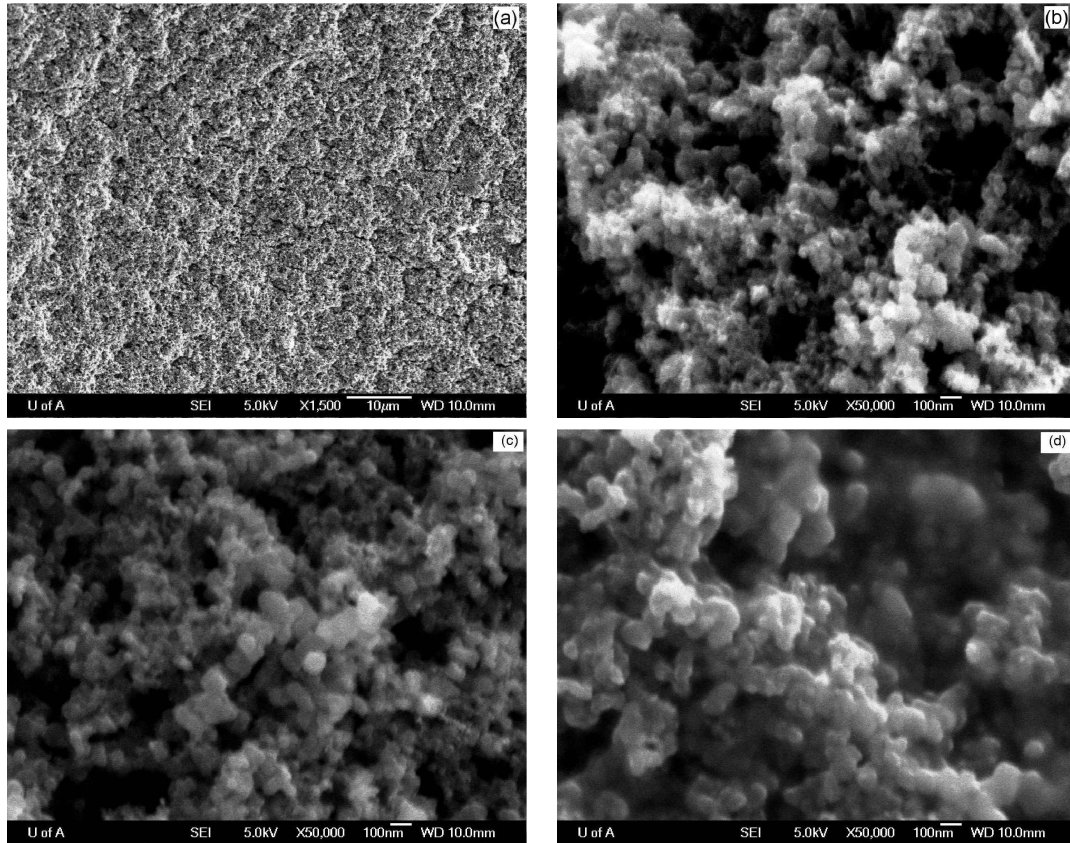
Figure 2.11 – Top view of the CCMs, (a) Surface structure - no micro-cracks observed (b-d) 20, 30 and 50 wt% Nafion loading CCMs. The particle size appears to increase with increasing ionomer content
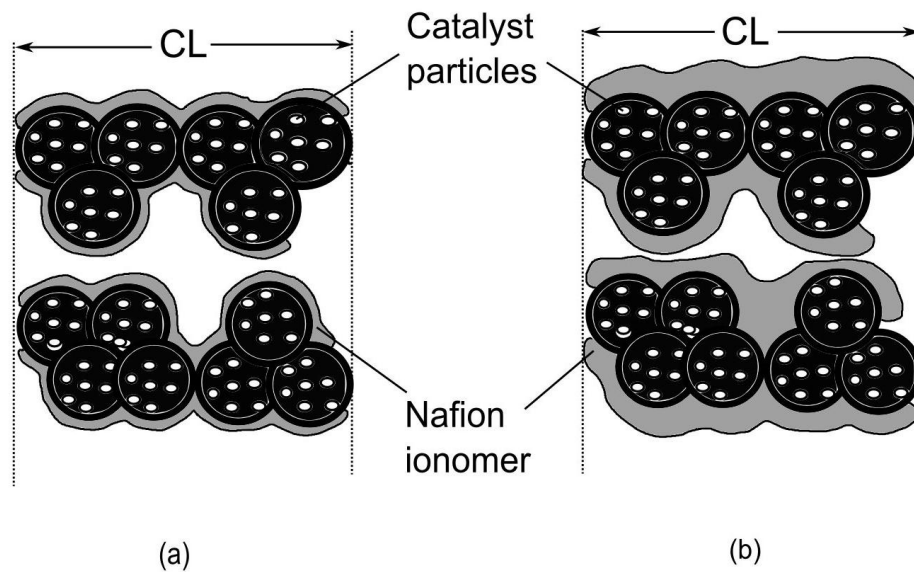
Figure 2.12 – Schematics showing the effect of Nafion loading on CL microstructure. (a) Lower NL (b) Higher NL. The CL thickness remains the same with increasing NL, however the gas diffusion resistance increases
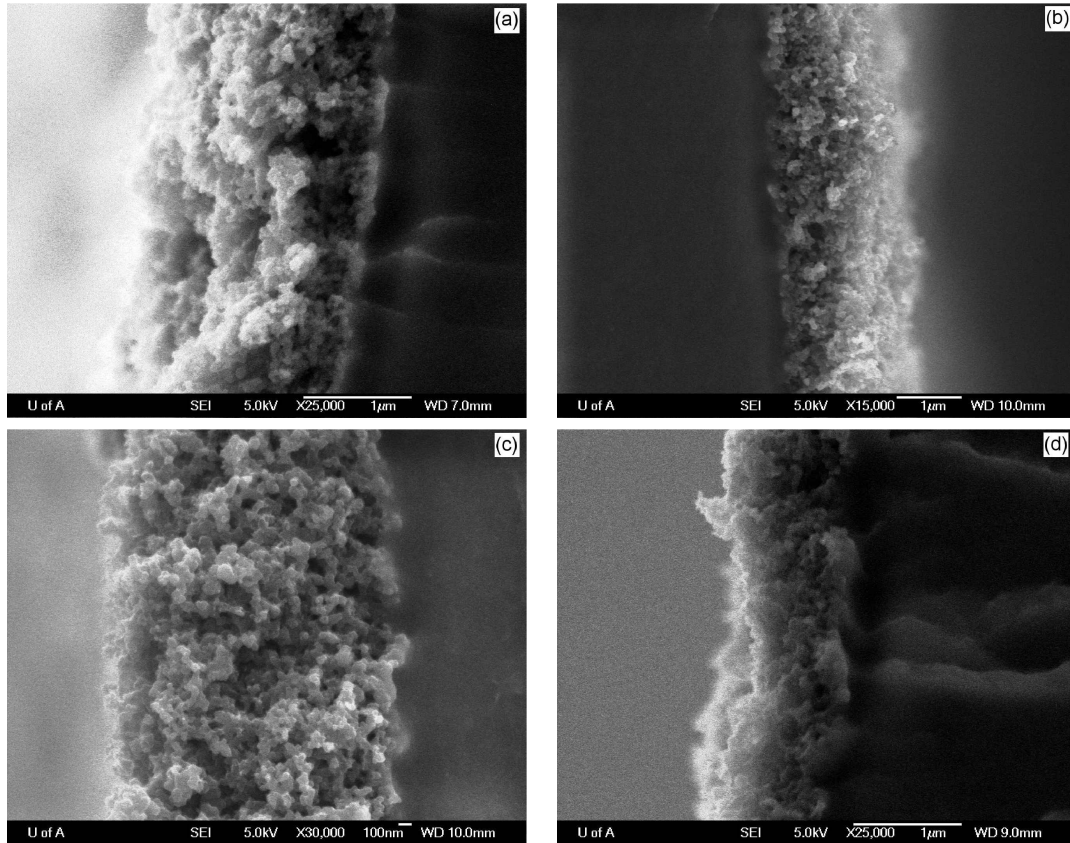
Figure 2.13 – Freeze-fractured side-view of the CCMs showing the CL thickness (a) 20 wt% NL (b) 30 wt% NL (c) 40 wt% NL and (d) 50 wt% NL. Thickness appears to be relatively constant with changing NL

Table 2.2 – Pt loading, CL thickness, active area and crossover data for the inkjet printed and spray coated CCMs

Nafion Content	I/C Ratio	Pt Loading (mg/cm^2)	Electrode Thickness(μm)	Active Area (m^2/g)	HOR Limiting current density @ 0.5 V(mA/cm^2)
10 wt%	0.14	0.026(estimated)	-	50	0.8
20 wt%	0.31	0.031 (XRF)	1.7±0.3	63	1.1
30 wt%	0.53	0.026(XRF)	1.8±0.3	65	0.5
40 wt%	0.83	0.027(XRF)	1.7±0.3	61	0.6
50 wt%	1.25	0.026(XRF)	1.7±0.4	56	0.8
spray coated CCM	-	0.1/0.4	~10	56	0.8

2.2.1.2 Electrode catalyst loading

The platinum loadings for the inkjet printed CLs are given in Table 2.2. XRF was used for measuring the Pt loading for the various NL samples. Gravimetric Analysis (GA) was used for the Pt loading measurement of 50 wt% NL sample. The Pt loading measured by GA was slightly lower at 0.022 mg_{Pt}/cm^2 than that measured using XRF at 0.026 mg_{Pt}/cm^2. This can be explained based on the thermal degradation of carbon and Nafion during GA as reported by Olga et al [118]. In order to evaporate glycerol, having a boiling point of 290°C, the GA sample was heat treated at 300°C for 3 hours. The carbon particles in the electrode in the presence of Pt which acts as a catalyst, start oxidizing to CO and CO_2 [118]. Decomposition of Nafion is also observed in presence of the catalyst at this temperature [118]. These changes in carbon and Nafion structures tend to lower the value of measured weight difference and ultimately the Pt loading value.

The Pt loadings values appear to be similar for all the samples irrespective of the Nafion content. It is hypothesized that this is because a fixed volume of ink for all the cases is maintained, that results in a similar particle concentration.

2.2.1.3 Electrode porosity

The porosity was estimated using the catalyst ink composition. Solid volume fraction (ϵ_S), electrolyte volume fraction (ϵ_N) and overall CL porosity (ϵ_V) were determined using the following relations [119]

$$\epsilon_S = \frac{m_{Pt}}{L}\left(\frac{1}{\rho_{Pt}} + \frac{1-Y_{Pt}}{Y_{Pt}\rho_C}\right) \tag{2.6}$$

$$\epsilon_N = \frac{m_{Pt}}{L}\frac{Y_{el}}{(1-Y_{el})Y_{Pt}\rho_N} \tag{2.7}$$

$$\epsilon_V = 1 - (\epsilon_S + \epsilon_N) \tag{2.8}$$

where m_{Pt} is the catalyst loading in g_{Pt}/cm^2, L is the catalyst thickness in cm, ρ_C, ρ_{Pt} and ρ_N are densities of carbon, platinum and Nafion taken as 1.69 g/cm³, 2 g/cm³ and 21.5 g/cm³ respectively. Y_{Pt} is the mass fraction of Pt on carbon support and Y_{el} is the NL in the CCM. The thickness values reported in Table 2.2 are used for calculations with a fixed Pt loading of 0.027 mg_{Pt}/cm^2. Figure 2.14 shows the effect of NL on the overall porosity of the CL. As the ionomer content in the CL increases with a relatively constant solid content mass fraction, the porosity decreases due to

the ionomer filling the secondary pores in the CL [55]. The porosity decreases from 57% for 10 wt% NL to 22% for 50 wt% NL. This decreased porosity for higher NL CCM results in increased mass transport losses at high overpotentials as evident from the performance plots describes later in the section.
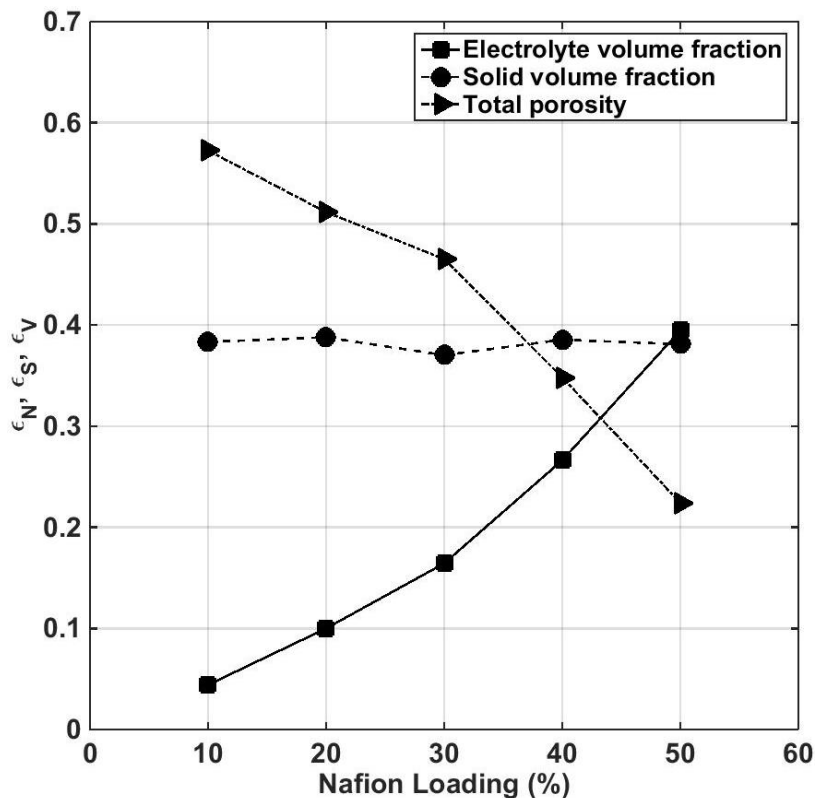
Figure 2.14 – Effect of Nafion loading on porosity in the IJP catalyst layers using data from Table 2.2

2.2.2 Electrode performance

Electrochemical characterization was carried out using a potentiostat and a fuel cell test station for determination of active area, electrode resistance and obtaining a polarization curve. In order to assess the maximum performance that could be achieved for the IJP CCMs, cell performance was obtained for the case of pure oxygen as the cathode feed at 0.2 slpm at 2 bar gauge pressure. The results are compared to conventional CCM at similar operating conditions.

2.2.2.1 Active area

Table 2.2 shows the active area values for the CCMs with NL ranging from 10 to 50 wt% corresponding to ionomer/carbon ratios of 0.14, 0.31, 0.53, 0.83 and 1.25, respectively. Figure 2.15 shows the cyclic voltammetry plots for the various NL CCMs. The active area for the CCMs with NL of 10, 20, 30, 40 and 50 wt% was found to be 50, 63, 65, 61 and 56 m^2/g respectively. The values appear to be similar in the range of 20 to 40 wt% NL with a slight drop for the 50 wt% NL case. The active area for the 10 wt% case on the other hand is lower in comparison. This can be attributed to a lower ionomer coverage of catalysts. It could have been further studied similar to the study reported by Iden [120]. A spray coated sample was also analyzed and the active area was found to be 56 m^2/g. These values for active area are slightly higher than those reported by Saha et al. [3] for their inkjet printed CCMs. This may be due to the difference in active area measurements (CO stripping vs. Hydrogen adsorption voltammetry), a different recipe for catalyst ink formulation and a lower wt% Pt on carbon catalyst. The variation in the active area for CCMs in the range of 20 - 50 wt% NL was not as prominent as those reported for the conventional CCMs [48, 51, 54]. This lack of dependence of the active areas with NL may be explained based on the electrode structure. Unlike conventional catalyst electrodes, very small variation in the primary Pt/carbon aggregate size and electrode thickness is observed in the inkjet printed layers. Using the same amount of dispersion media irrespective of the NL may help in similar Pt/carbon aggregate size. Furthermore, the electrolyte seems to evenly coat all particles providing access to most of the electrode pores. This equal aggregate size and Nafion dispersion resulted in similar electrode thicknesses for the 20 - 50 wt% NL electrodes thereby reducing the differences in interfacial zones for the different NL samples.

It was also observed that changing the type of dispersion medium for making the catalyst ink had an effect on the active area for the inkjet printed CCMs as well as their cell performance. This may be due to a combination of the change in aggregate size with the dispersion media type during ink formulation as well as speed of drying of the media after fabrication which would affect the electrode microstructure [100].

2.2.2.2 Hydrogen crossover

The membrane permeates a small amount of H_2 across. The electro-oxidation of diffused H_2 at the cathode results in an internal current and a mixed potential thereby reducing the open circuit voltage (OCV) from the expected value based on oxygen
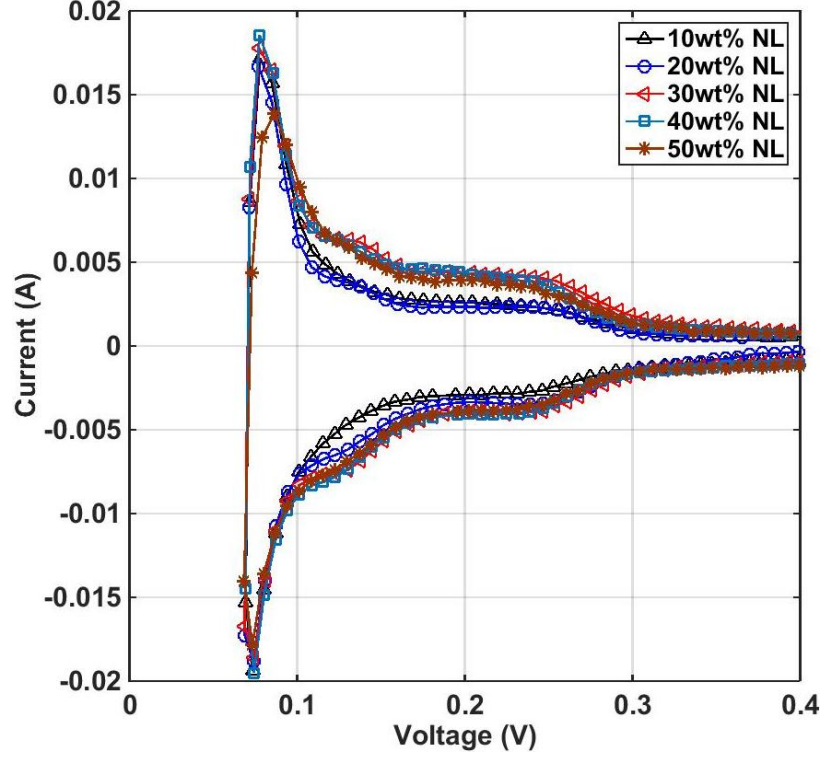
Figure 2.15 – Cyclic voltammetry plots for CCMs with ionomer loading from 10 to
50 wt% using scan rate of 40 mV/sec at 30°C (100% RH) using H$_2$/N$_2$

and hydrogen partial pressures on cathode and anode respectively. This produces a
limiting current density which ideally remains constant with an increase in applied
voltage during the chronoamperometry experiment. Table 2.2 gives the values for the
limiting current densities at 0.5 V for Hydrogen oxidation reaction (HOR) for the
different NL samples at 30 °C. The hydrogen crossover values for the inkjet printed
samples are low. Therefore the fabrication method does not seem to damage the
membrane.

Figure 2.16 shows the measured crossover current with time with voltage incre-
ments from 0.2 to 0.5 V for the case of a 40 wt% NL CCM. The crossover current is
small, indicating the absence of any major pinholes in the membrane. Based on Equa-
tion (2.5), the crossover flux of hydrogen was calculated to be 1.55×10^{-8} mol s^{-1}cm^{-2}.

Using simple Tafel kinetics, the loss in overpotential, η, related to the hydrogen
crossover current, i_x, can be evaluated as [31]

$$\eta = \frac{2.303RT}{\alpha F} log \left[\frac{i + i_x}{m_{Pt} A_{Pt} i_o} \right] \qquad (2.9)$$

39
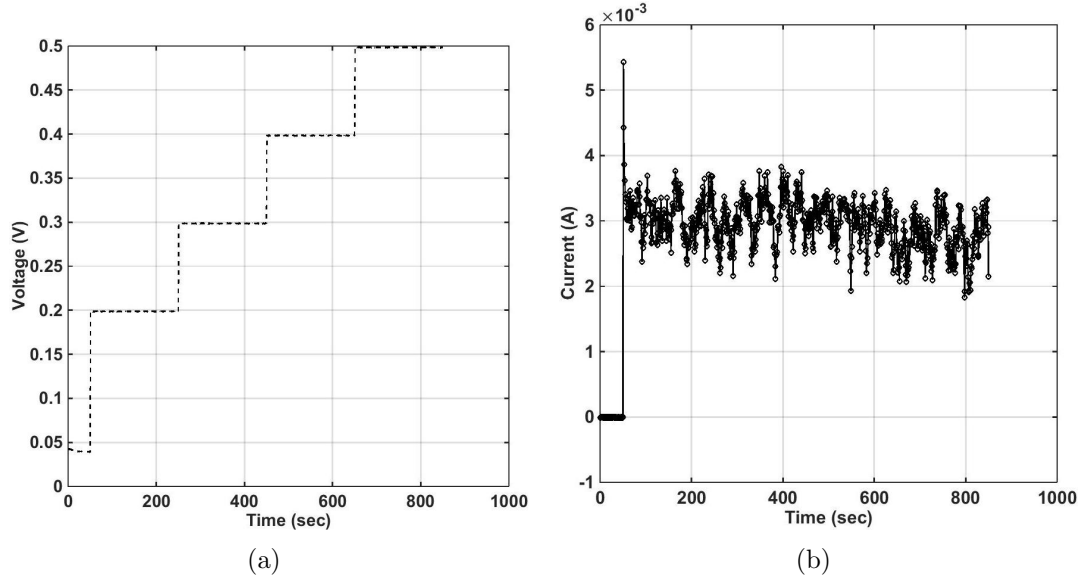
Figure 2.16 – Measured crossover current with time for the case of 40 wt% NL CCM at 30°C (100% RH) using H_2/N_2. The flux of H_2 crossover is calculated to be 1.55×10^{-8} mol s^{-1}cm^{-2} (a) Increasing voltage steps from 0.2 V to 0.5 V (b) measured crossover current

The charge transfer coefficient (α) was evaluated for each case based on the Tafel slope and the overpotential due to crossover was calculated to be 0.3 V, 0.29 V, 0.26 V, 0.27 V and 0.22 V for the IJP CCMs from 10 wt% to 50 wt% respectively.

2.2.2.3 Protonic and charge transfer resistance

The *in-situ* current interrupt method does not include the ohmic resistance of the electrodes due to their capacitive behavior [115]. Hence, in order to quantify the effect of ionic resistance with the changing NL of the IJP electrodes, potentiostatic EIS using H_2/N_2 at 50% and 0% (anode and cathode humidity) was used. The ionic migration through the catalyst layer is represented by the 45° slope at high frequencies, and can be used to quantify the resistance value for the electrodes [115, 121]. The protonic transport resistance in the electrodes, R_{CL} is given as [115]

$$R_{CL} = 3 \times \Delta Z_{real} \tag{2.10}$$

where ΔZ_{real} is the difference in the real impedance values for the projected 45° branch of the Nyquist plot, as shown in Figure 2.17(b). The high frequency x-intercept corresponds to the total of membrane and electronic resistance. Figure 2.17 (a) shows the Nyquist plots for the 30 wt% NL CCM at cathodic RH values from 0% to 50% (80°C). At higher RH values as evident from the figure, electrode protonic resistance

dropped and no longer corresponded to a 45° line needed for the quantification of the protonic resistance. Thus, a dry working electrode (0% RH) was used since only at this condition, a 45° line could be observed. The x-intercept is seen to decrease from 0% to 50% RH due to the reduction in the membrane resistance owing to increased hydration. The ohmic resistance of 40 mΩ for 30 wt% NL at 50% RH from EIS was slightly higher than that measured by the current interrupt method ($\sim$30 mΩ).

Figure 2.17 (b) shows the Nyquist plots for NL CCMs from 20 wt% to 50 wt% NL at 0% RH. The calculated values for the ionic resistances for the different samples are given in Table 2.3. The values corresponding to the 20, 30, 40 and 50 wt% NL CCMs are approximately 69, 60, 27 and 15 mΩ.cm^2. It can be seen that the ionic conductivity of the electrodes increase with increasing ionomer content, since the ionomer facilitates proton transfer across the electrodes.

(a)   (b)
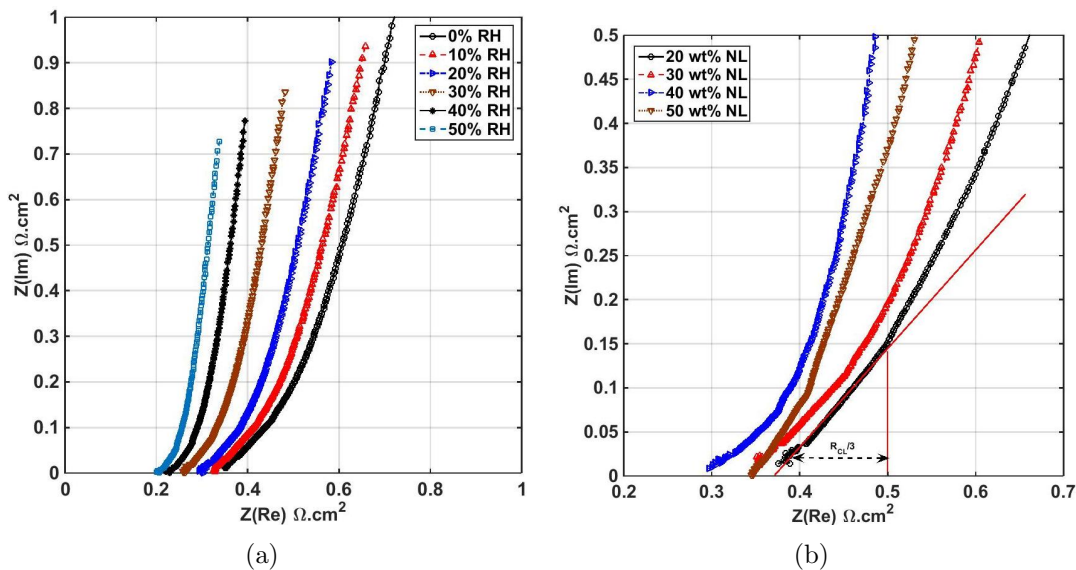
Figure 2.17 – Nyquist plots using potentiostatic EIS at a cell potential of 0.5 V at 80°C (Anodic RH of 50%) using H_2/N_2 at 0.1 lpm (a) Effect of cathodic RH from 0% to 50% for 30 wt% NL (b) effect of NL from 100 Hz to 25 kHz with cathodic RH of 0%

Figure 2.18 shows the galvanostatic EIS plot for the case of 10, 40 and 50 wt% NL CCM at currents of 10 mA/cm^2 and 200 mA/cm^2 using H_2/air (50% RH). The charge transfer resistance decreases with increase in overpotential and can be estimated based on the diameter of the semicircular loop that is obtained in the Nyquist plot. A fluctuation free semicircular plot suggests that it can be represented by a
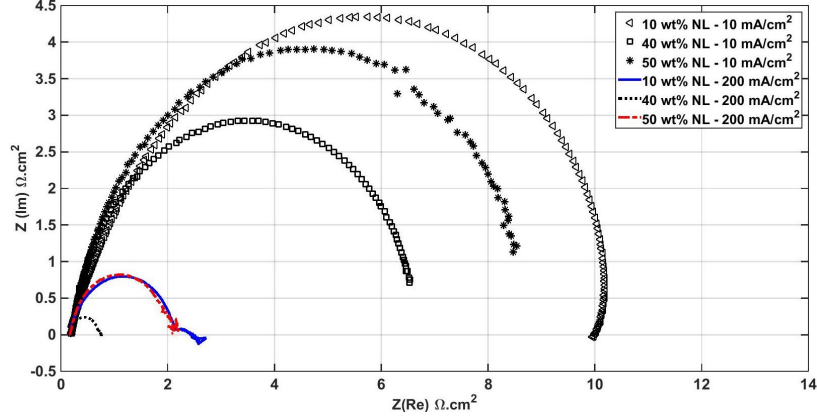
Figure 2.18 – Nyquist plots using galvanostatic EIS for the case of 10, 40 and 50 wt% NL CCMs corresponding to currents of 10 and 200 mA/cm^2 using H$_2$/air at 80°C (50% RH) from 1 Hz to 10 kHz

simple Randles circuit [122]. The charge transfer resistance decreases with increasing overpotential. The values for charge transfer resistance obtained at 10 mA/cm^2 (kinetic region) were 10, 6.5 and 8.5 Ω.cm^2 for NL values of 10, 40 and 50 wt%, respectively. These resistance values correspond well with the active area values for the cells since the charge transfer resistance should be related to the electrode active area. At 200 mA/cm^2, the charge transfer resistance of 40 wt% NL is lowest with absence of any low frequency feature suggesting that cathodic mass transport losses are minimal in this cell. The 10 wt% and 50 wt% NL CCMs show a higher charge-transfer resistance at this current density.

2.2.2.4 Electrode kinetics

In spite of fabricating the CCMs with similar Pt loadings, the oxygen reduction reaction (ORR) kinetics for the cells will depend on the amount of Nafion ionomer in the electrodes. Based on the simplified form of Butler-Volmer equation, we can write [13]

$$ln(i) = ln(i_0) + \frac{2.303}{b}\eta \tag{2.11}$$

The Tafel slope, b and the exchange current density, i_0 were evaluated based on the slope and intercept of the plot between overpotential, η and $ln(i)$ respectively and confirmed using $FCView$ data analysis software. For determination of the Tafel slope, first 5 points on the polarization curve (20-100 mA/cm^2) were considered. Figure 2.19 shows the Tafel plot for the various NL CCMs at 90% RH. The corrected voltage ($V_{corrected} = V_{cell} + R_i$) obtained from current interrupt measurements is used.
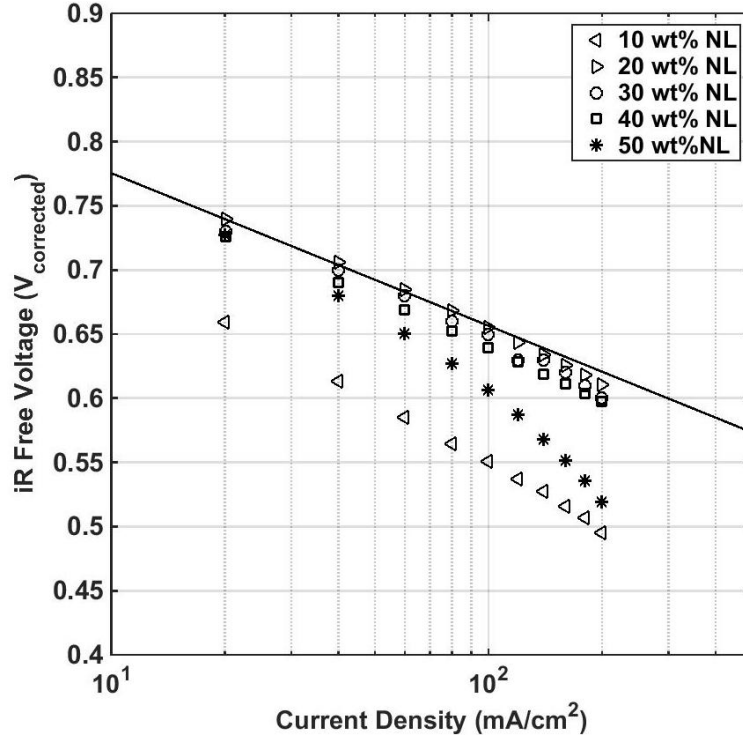
Figure 2.19 – Tafel plots for the various NL CCMs at 80°C (90% RH) using H_2/air at ambient pressure

Table 2.3 gives the evaluated values for b and i_0 for the different NL CCMs at the specified conditions. It can be seen that the values of Tafel slope are higher than those reported for conventional CCMs when operating with H_2/air at ambient pressure. This is most likely due to the transition in the oxygen reaction pathway. A change in Tafel slope from 60 mV/dec to 120 mV/dec has been observed experimentally [123–134] which is sometimes associated with mass transport losses. For the low Pt loading electrodes, b is measured at cell voltages below the transition overpotential, i.e., below around 0.75 - 0.8 V, since a higher overpotential is required to achieve current densities of the order of 10 mA/cm² as compared to the spray coated electrode. Also, a further increase in slope takes place for the IJP electrodes at higher currents due to transport losses. These results highlight the fact that there is a doubling of the Tafel slope at voltages of about 0.8 V that is independent on oxygen transport limitations. The Tafel slope decreased from 121 mV/decade to 77 mV/decade when operating with oxygen at 2 bar. At this higher pressure, between 20 - 100 mA/cm², the cell voltage was above 0.75 V, which is above the transition voltage of 0.9 - 0.75 V [135]. More details regarding the analysis of Tafel slope is discussed in chapter 3.

Table 2.3 – Kinetic parameters and protonic electrode resistances for different NL CCMs at 90% RH

Nafion Content	P_{O_2} (atm)	Tafel Slope (b, V/dec)	Exchange current density (i_o, A/cm$^2_{Pt}$)	Electrode resistance at 0% RH from EIS (mΩ.cm^2)
10 wt%	0.12	0.156	7.53×10^{-7}	-
20 wt%	0.12	0.127	2.56×10^{-7}	69
30 wt%	0.12	0.121	2.13×10^{-7}	60
40 wt%	0.12	0.124	2.7×10^{-7}	27
50 wt%	0.12	0.169	2.96×10^{-6}	15
30wt% (1.5 bar)	0.44	0.092	1.23×10^{-7}	-
30wt% - O_2	0.59	0.101	1.01×10^{-7}	-
30wt% - O_2 (2 bar)	2.59	0.077	5.44×10^{-8}	-

Considering overall ORR kinetics, we can write the Tafel equation as follows [31]

$$i = i_o^{ref} \left(\frac{P_{O_2}}{P_{O_2}^{ref}} \right)^{\gamma} exp \left(\frac{\alpha F}{RT} \eta \right) \tag{2.12}$$

where γ is the reaction order, P_{O_2} and $P_{O_2}^{ref}$ are the actual and reference oxygen partial pressures, η is the overpotential and α is the charge transfer coefficient. Taking logarithm on both sides and rearranging,

$$ln(i) = ln \left(\frac{i_o^{ref} exp(\alpha F \eta / RT)}{(P_{O_2}^{ref})^{\gamma}} \right) + \gamma ln(P_{O_2}) \tag{2.13}$$
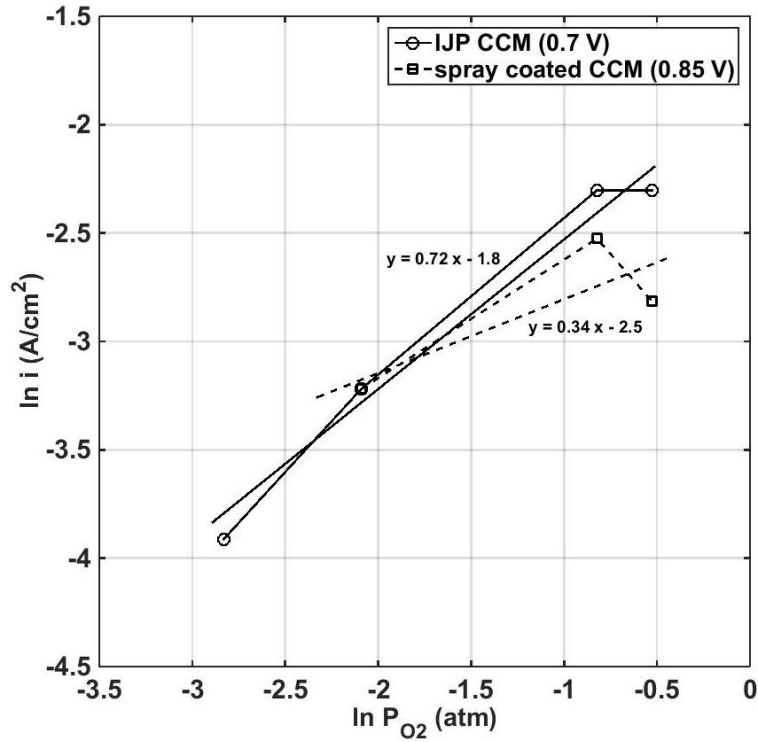
Figure 2.20 – Reaction order (γ) comparison for the IJP and spray coated CCMs at 80°C (70% RH) at voltages of 0.7 V_{iRFree} and 0.85 V_{iRFree} respectively

The first term on the right hand side is constant at a given value of η. Thus, the slope of the line obtained by plotting $ln(i)$ vs. $ln(P_{O_2})$ will give the value of γ. Figure 2.20 shows this plot for the case of inkjet printed 30 wt% NL CCM and the spray coated CCM at 70% RH and 80°C. For the inkjet printed CCM, data points for current density were obtained using 10% oxygen, air (ambient), air (1.5 bar) and pure oxygen as cathodic reactants at V_{iRFree} of 0.7 V. In these cases, the current density was between 20 to 80 mA/cm². For the spray coated CCM all except the 10% oxygen

were used as reactants at 0.85 V_{iRFree}. These values of voltages corresponded with the kinetic regions of the polarization plots for the given cases. The values of γ_{IJP} and γ_{SC} for the IJP CCM and spray coated CCM are calculated to be 0.72 and 0.34 respectively. Differences in these values suggests variation in the rate determining step in the ORR mechanism for the two cases. However, as described in chapter 3, the measured total reaction order at 0.75 V_{iRFree} is observed to be close to one for both IJP and spray coated electrodes.

2.2.2.5 Performance at different operating conditions

Figure 2.21 (a-c) shows the cell performance for the case of 10, 20, 30, 40 and 50 wt% Nafion loadings at 50%, 70% and 90% RH respectively. Relative humidity and Nafion loading affect both electrolyte hydration state and the effective gas transport in the electrodes in case of flooding. The performance for all the NL CCMs is seen to improve with RH from 50% to 90%. Minimal variation in performance for the CCMs between 20 to 40 wt% NL can be seen unlike that for conventional electrodes. The IJP CCMs did not show any apparent sign of flooding at high RH unlike the NSTF electrodes [62].

The performance in the kinetic region is very similar for the case of 20 - 50 wt% NL CCMs as there are minimal variations in the active area values. The 10 wt% NL CCM shows a substantial increase in performance in the kinetic region when the RH is increased. This may be due to an increase in the number of active catalytic sites as the electrode is hydrated. For low ionomer loadings, the ionomer is likely not surrounding all the Pt particles. In this case, water might act as an electrolyte thereby activating Pt particles that would otherwise not be active.

Figure 2.22 shows the cell resistance obtained from the current interrupt method for different NL cases at 50, 70 and 90% RH. The electrodes are affected by reduced membrane hydration when the ionomer content is very low which is evident by the higher ohmic resistance and poor performance of the 10 wt% NL CCM at 50% RH. The performance dependence on RH is greater if the electrode ionomer content is lower. Thus, for the case of 10 wt% CCM, the performance change from 50% RH to 90% RH is more pronounced than observed for the case of 20, 30, 40 and 50 wt% CCM. In fact, the current density at 0.2 V for the 10 wt% NL doubled when the RH was increased from 50 to 90%. This can be mainly due to the increased active area and reduced proton transport losses because of increased hydration in the electrodes and membrane.
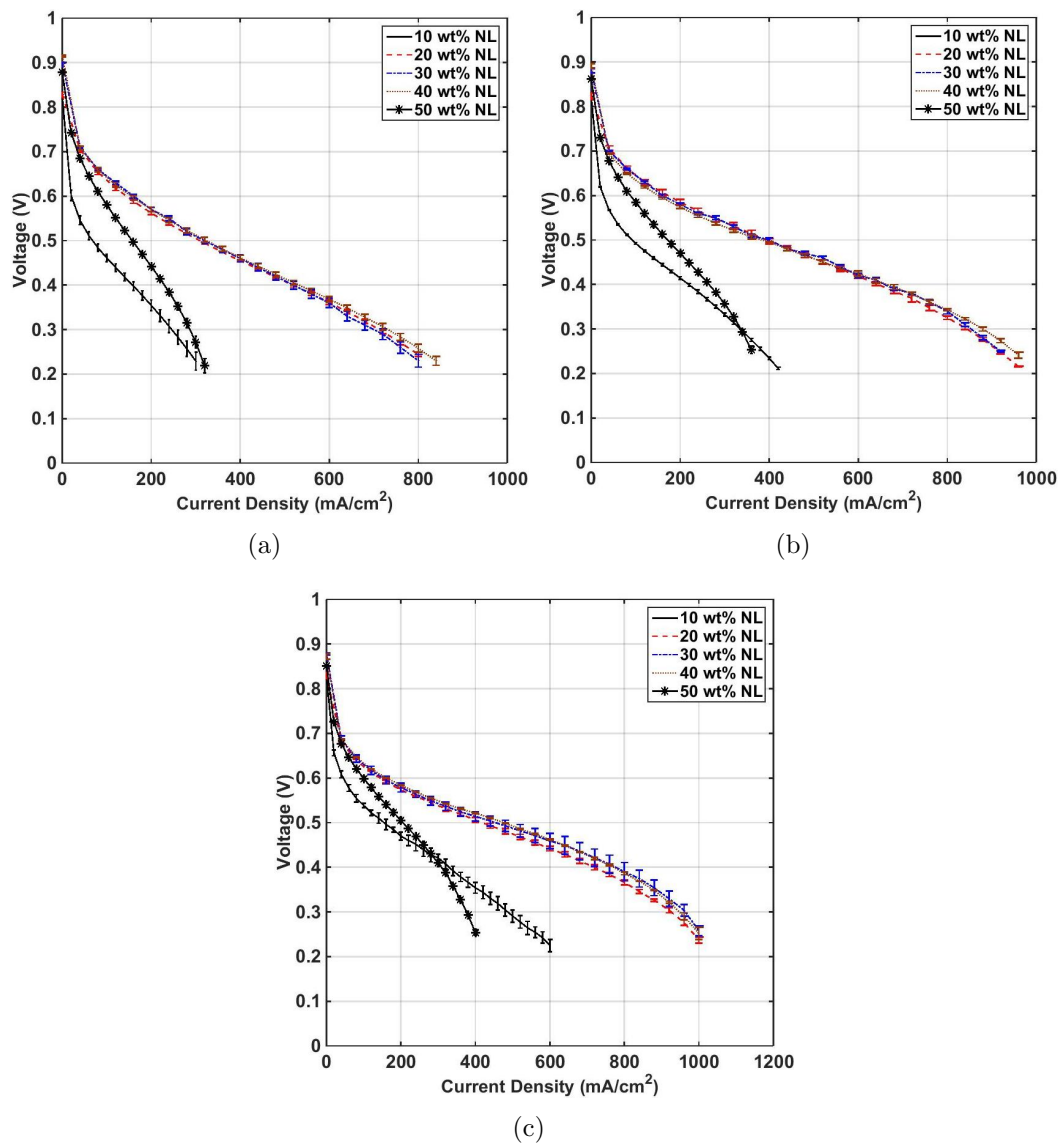
Figure 2.21 – Effect of Nafion loading on cell performance using H_2/air at ambient pressure (a) 50% RH (b) 70% RH (c) 90% RH

The sensitivity to RH on NL is minimized when the NL is between 20 and 40 wt%. Due to the reduced thickness of the electrodes with NL between 20 wt% and 40 wt%, the proton transport and mass transport losses might be very similar at the macro-scale and that the electrodes might be limited mainly by micro-scale interfacial transport losses or the kinetics of the reaction due to the low Pt loading [42, 76]. Lack of sensitivity to Nafion loading indicates that the interfacial resistance is not likely due to transport in the bulk film but due to either dissolution of oxygen in Nafion
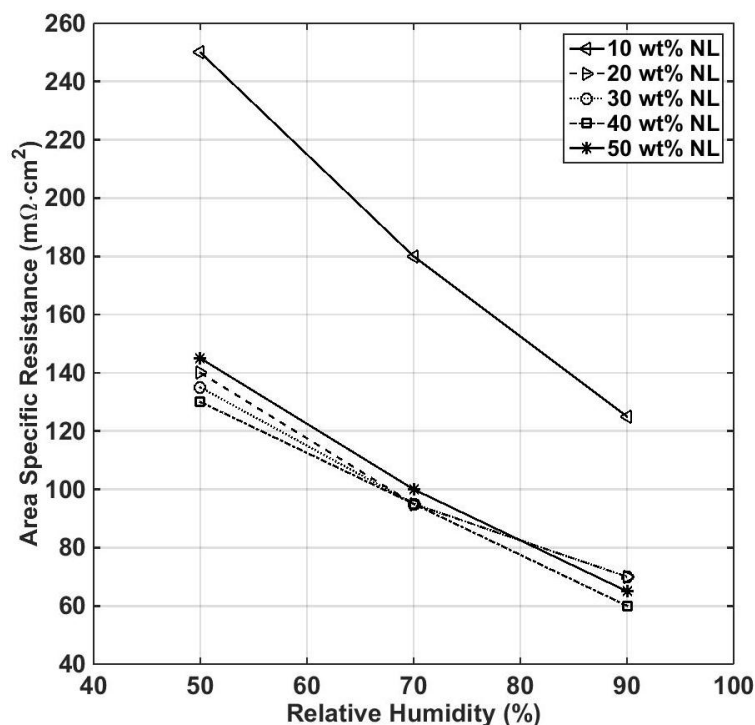
Figure 2.22 – Effect of NL on ohmic resistance (obtained from current interrupt method) at different humidity values at 80°C

or poisoning of the catalyst. As the NL increases to 50 wt%, electrode porosity reduces because of the increase in the ionomer volume fraction and probably ionomer film thickness around the particles. This hinders the effective oxygen diffusion at the cathode reducing the cell performance due to increased mass-transport losses. It was also observed that there was a drop in OCV for the cells as the RH increased from 50% to 90%.

Figure 2.23 shows the voltage variations at current densities of 0.2, 0.4, 0.6, 0.8 and 1 A/cm² for NL of 10, 20, 30, 40 and 50 wt% for 50% and 90% RH. Similar voltage variations were observed at 70% RH as well. The samples that could not reach the given current densities are given a value of zero. It can be seen from the figure that unlike Xie et al [48] who observe the effect of Nafion on cell performance over entire range of the polarization plot for their conventional CCM, the IJP CCMs in the range of 20 - 40 wt% NL seem to be independent of NL from 0.2 A/cm² (kinetic region) to 1 A/cm² (mass-transport region). This low sensitivity to NL towards cell performance of the electrodes is likely due to the shorter transport pathway necessary for both protons and oxygen in the macro-scale.
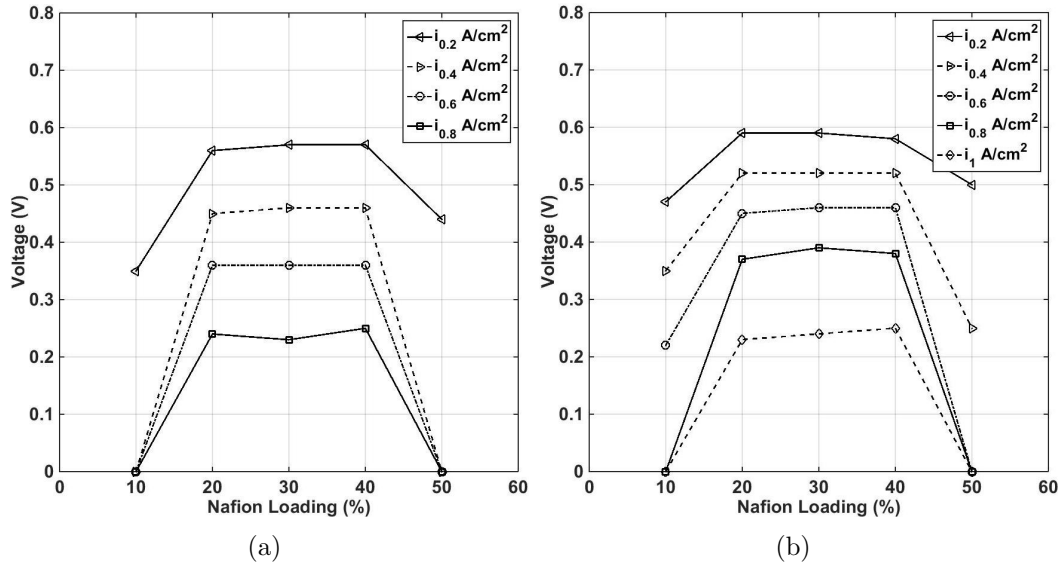
Figure 2.23 – Voltage variations at current densities of 0.2, 0.4, 0.6, 0.8 and 1 A/cm^2 for NL of 10, 20, 30, 40 and 50 wt% at 80°C. (a) 50% RH (b) 90% RH
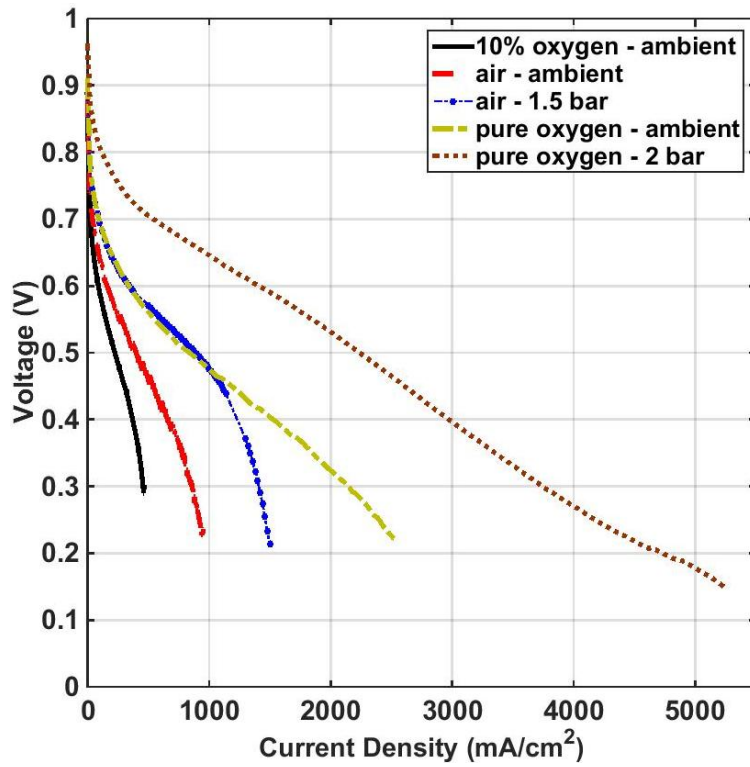
Figure 2.24 – Performance of 30 wt% NL CCM at various operating conditions

Figure 2.24 shows the polarization plot of a 30 wt% NL CCM under various effective oxygen partial pressures from 0.07 bar to 2.7 bar at 70% RH and 80°C. Using pure oxygen and a higher system pressure of 2 bar, the low loading inkjet printed CCMs exhibit a current density greater than 5 A/cm^2 without any apparent mass transport limitations, due to the absence of vertically decreasing voltage at high current densities. This is likely due to improved micro-scale oxygen transport or kinetics since macro-scale charge and mass transport resistances are low due to the reduced thickness.

2.2.3 Comparison with conventional CCM

The IJP CCMs were compared to a spray coated CCM having a cathodic Pt loading of 0.4 mg/cm^2. The spray coated CCM was tested in the same test station using the same GDLs and hardware. Due to the much lower Pt loading compared to the spray coated CCM, the IJP CCM prepared in-house performs poorly in the kinetic region as expected. The OCV for the IJP CCM is lower, even though similar crossover currents are observed when compared to the spray coated sample, thereby showing that low loading electrodes might be more susceptible to crossover. Unlike the inkjet printed thin CCMs, the current density observed at around 0.2 V for the case of a thicker spray coated CCM is lower at higher operating RH (comparing the 50% and 90% RH conditions) as shown in Figure 2.25. At similar voltage values, the current density for IJP CCM increased from 840 mA/cm^2 at 50% RH to 1020 mA/cm^2 at 90% RH. On the other hand, the current density for the spray coated CCM decreased from 1540 mA/cm^2 to 1420 mA/cm^2 from 50 % to 90% RH. Therefore, the trade-off between flooding and high electrolyte conductivity for thin IJP CCMs are different than that observed for conventional electrodes.

Figure 2.26 shows the performance comparison at 80°C and 70% RH at ambient and 1.5 bar cell pressures. The low Pt loading and high Tafel slope at voltages below 0.7 V both combine to produce the low kinetic performance for the IJP CCM. However, it is apparent that the gain in performance with increased cell pressure is higher for the IJP CCM as compared to the spray coated CCM. Figure 2.27 shows the normalized current density change (change in i from ambient to 1.5 bar gauge pressure to i at ambient pressure) with voltage for the two cases. At 0.5 V, the increase in current density with back pressure, Δi for the IJP CCM was 460 mA/cm^2 as opposed to 180 mA/cm^2 for the spray coated CCM at the same conditions. It has been unclear as to what was causing such a performance increase with increased
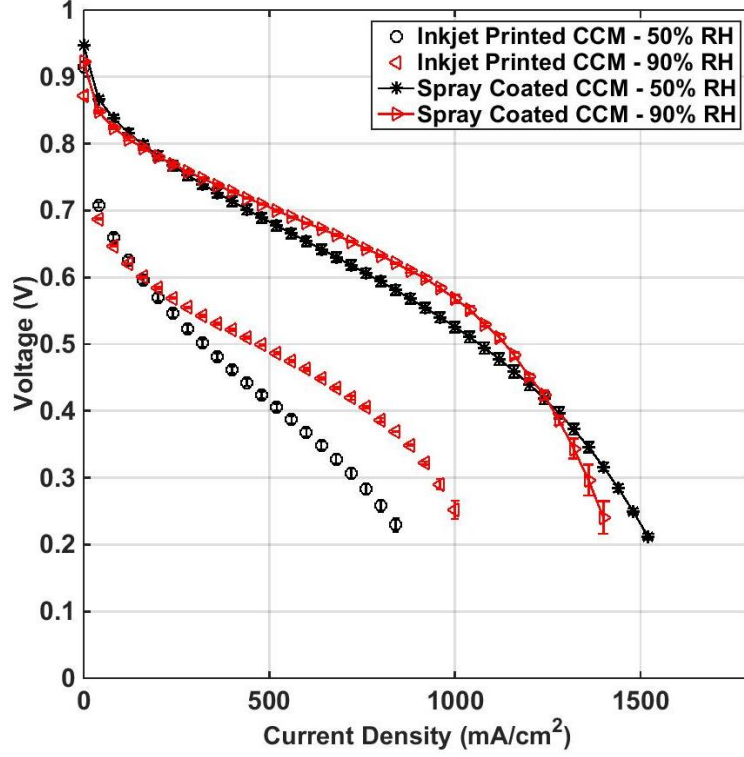
Figure 2.25 – Performance comparison between spray coated and inkjet printed (40 wt% NL) CCMs at 50% and 90% RH using H_2/air at ambient pressure (80°C). Current density at 0.2 V decreases with RH for the thicker spray coated CCM while it is seen to increase for the IJP CCM

pressure specifically for the case of IJP electrodes. To understand the reason for this, a detailed kinetic analysis for IJP electrodes is presented in chapter 3.

The specific mass activity (MA) is the amount of current per gram of the catalyst and can be calculated from the following relation,

$$MA = \frac{i(A/cm^2)}{m_{Pt}(g/cm^2)} \tag{2.14}$$

where i is the current density and m_{Pt} is the catalyst loading. Figure 2.28 shows a comparison between the mass activities of IJP and spray coated CCMs. It can be seen that even though the spray coated CCM produces more current at ambient operating pressure, the amount of current per gram of Pt is much higher for the inkjet printed CCM. The amount of current per gram of Pt is almost ten times higher at 3.76×10^4 A g^{-1} at high current densities due to the reduced thickness of IJP electrodes and enhanced mass and proton transport at higher current densities. A thinner CL result in higher proton and oxygen transport across the CL thereby increasing the electrolyte potential and oxygen concentration at the Pt surface and thus increasing the Pt activ-
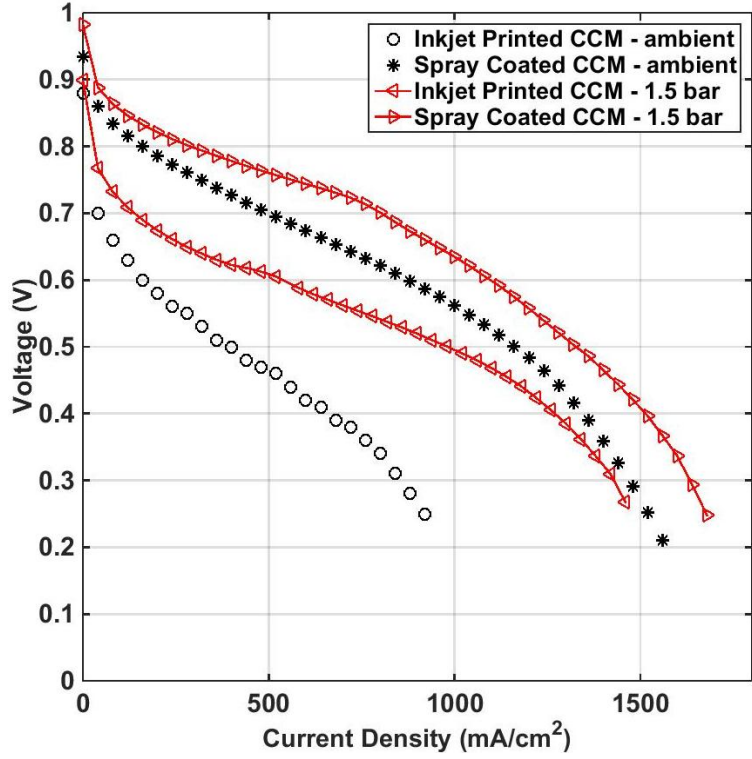
Figure 2.26 – Performance comparison between spray coated and inkjet printed CCMs (70% RH, 80°C) using H_2/air at ambient and 1.5 bar gauge pressure

ity. For the spray coated CCM operating at mass-transport limited conditions, only the Pt at GDL|CL interface is utilized at higher current densities thereby lowering catalyst utilization. [7]
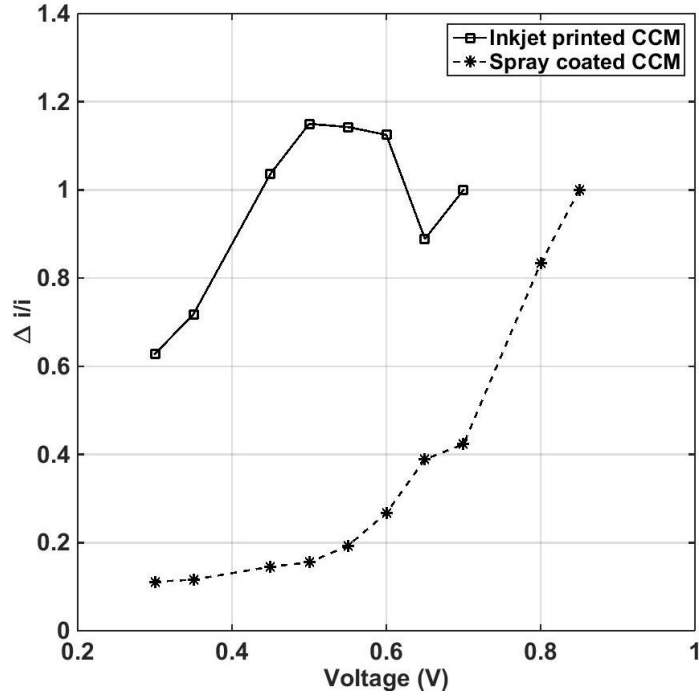
Figure 2.27 – Change in current density from ambient to 1.5 bar gauge pressure for inkjet printed and spray coated CCMs at 70% RH, 80°C. ΔI is higher for the case of inkjet printed CCM
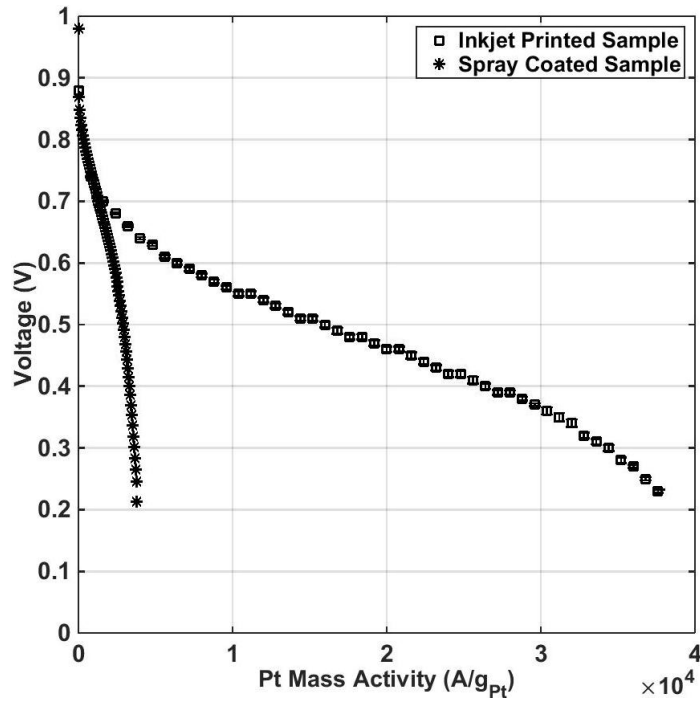
Figure 2.28 – Specific mass activity comparison of spray coated and inkjet printed CCMs (70% RH, 80°C) using H_2/air at ambient pressure (70% RH, 80°C)

Table 2.4 – Comparison of the reported values for peak Pt utilization for low loading CCMs

Fabrication method	Pt loading (mg cm^{-2})	Operating temperature (°C)	Operating gauge pressure (bar)	Feed gas	Peak cathodic Pt utilization (kW g$_{Pt}^{-1}$)	Reference
Sputtering	0.005	21	ambient	H$_2$/O$_2$ (humid)	23	[41]
Sputtering	0.01	80	3.8-3.1	H$_2$/O$_2$ (humid)	40	[64]
Electrospray	0.01	70	3.4	H$_2$/O$_2$ (dry)	60	[136]
Inkjet printing	0.02	60	0.35	H$_2$/air (humid)	9.4	[3]
Inkjet printing	0.026	80	ambient	H$_2$/air (humid)	12.4	This work
Inkjet printing	0.026	80	2	H$_2$/O$_2$ (humid)	47.6	This work
Inkjet printing	0.014	80	2	H$_2$/O$_2$ (humid)	63.8	This work

Table 2.4 gives the summary of the reported values for peak specific power density ($kW \ g_{Pt}^{-1}$) for some of the low Pt loading electrodes available in literature. This value was obtained by normalizing the maximum power produced by the electrodes with their Pt loadings. Operating parameters such as the cell temperature, pressure and the cathodic oxygen concentration vary between the reported values and they strongly influence the Pt utilization. As seen in the Table 2.4, the peak specific cathodic power density for the inkjet printed CCMs, prepared in-house, tested at ambient pressures using H_2 and air is 12.4 kW g_{Pt}^{-1}. When operating with pure oxygen at 2 bar gauge pressure, the peak specific power density rises to 47.6 kW g_{Pt}^{-1}. An IJP CCM with 3 printed layers ($\sim$0.014 mg/cm^2) was also tested using fully humidified H_2/O_2 at 2 bar gauge pressure and the peak Pt utilization was found to be 63.8 kW g_{Pt}^{-1}. These values represent one of the highest reported values in PEFC literature.

2.3   Conclusions

Thin, low Pt loading catalyst layers were fabricated for both anodic and cathodic electrodes using the piezoelectric inkjet printing having a Pt loading of 0.026 mg/cm^2. Micro-structure characterization revealed that electrode thickness was 1.5 - 2 μm and that particle size increased with NL. This increase in particle size was thought to be due to the increase in ionomer film thickness surrounding the catalyst particles. Estimation of porosity for the different NL CCMs showed a decrease from 0.57 to 0.22 as the Nafion loading in the electrodes increased from 10 wt% to 50 wt%. A kinetic analysis showed that the Tafel slopes for the electrodes were found to be approximately 120 mV/dec at current densities where mass transport losses are not important suggesting that the commonly observed doubling of Tafel slope below around 0.75 V is not due to mass transport limitations, but to a change in the reaction mechanism in the ORR [135].

A parametric study of Nafion loadings from 10 - 50 wt% revealed that the CCMs have a very small sensitivity to ionomer loading between 20 and 40 wt%, thereby highlighting that a trade-off between oxygen and proton transport does not exist. Unlike conventional CLs, the thin, low loading electrodes appear to be independent on NL over the entire range of polarization curve (kinetic, ohmic and mass-transport regions). These results would suggest that IJP electrodes are mainly limited by either catalyst kinetic losses or micro-scale transport losses.

Thin, low loading catalyst layers fabricated using inkjet printing electrodes show

an increased catalyst mass activity of almost ten times when compared with a conventional spray coated CCM at high current densities due to the improved proton and oxygen transport across the CL. Since low loading electrodes are mainly kinetically limited, a substantial increase in their performance can be obtained at higher oxygen partial pressures.

Chapter 3

Analysis of kinetic parameters and oxygen transport resistance

In the previous chapter, thin, low Pt loading IJP electrodes were characterized. Comparing to a conventional spray coated electrode, the low performance of the IJP electrodes in the kinetic region was primarily identified to be due to their lower Pt loading. In order to improve the electrode kinetics, inkjet printed electrodes with Pt loadings ranging from 0.014 mg/cm² to 0.113 mg/cm² were fabricated by increasing the number of deposited passes from 3 layers to 20 layers and characterized. Section 3.1 describes the experimental methods for ink preparation, CCM fabrication and characterization techniques used. Section 3.2 includes the results and discussion on kinetic parameters including active area, Tafel slope and oxygen reaction order and how they compare with the literature data. This section also includes the evaluation of oxygen transport resistance from limiting current density experiments. Concluding remarks are given in Section 3.3.

3.1 Materials and methods

3.1.1 CCM preparation

A similar procedure to the one reported previously was followed to formulate the catalyst inks and fabricate the CCMs, however a lower boiling point solvent was used to aid in the drying process [74]. The catalyst, 20% Pt/C on Vulcan XC carbon black (Hi SPEC 3000, Alfa Aesar), was mixed with ethylene glycol and Isopropanol ($\geq$99.5%, Fisher Scientific) and bath sonicated for 30 minutes (Branson-1800). 5 wt% of Nafion

---

ionomer solution (Ion Power) was added drop-wise to the ink during sonication. The Nafion loading was kept constant at 30 wt% (ionomer/carbon = 0.54). The ink was then probe sonicated (S-4000, Q-Sonica) for 15 minutes (2 min. ON, 1 min. OFF) to further help in breaking the aggregates. Finally, the ink was left on the magnetic stirrer to homogenize the suspension prior to its use.

CL fabrication was carried out using a commercial inkjet printer (Dimatix-2831, Fujifilm). 5 cm^2 CLs were printed directly on the Nafion membrane acting as a substrate (NR-211 from Ion Power as received). The Pt loading on the cathodic electrodes was varied by changing the number of printed passes. CLs with 3, 5, 10, 15 and 20 layers (L) were fabricated corresponding to cathodic Pt loadings of 0.014, 0.026±0.005, 0.056±0.012, 0.080±0.019 and 0.113±0.026 mg/cm^2 respectively. The anodic Pt loading was fixed at 0.026±0.005 mg/cm^2 (5L). Once both anodic and cathodic electrodes were fabricated, the CCMs were dried in the oven at 80°C for a few hours to evaporate the solvents, boiled in deionized water for around 3 hours and stored for further use. Pt loading of the CCMs was measured using gravimetric analysis, and confirmed by X-ray fluorescence (Themo Scientific, Niton XL3t) for several samples. The average values and standard deviations are obtained from three independently fabricated samples. For comparison, a spray coated electrode is used. The spray-coated electrode had a cathodic Pt loading of 0.4 mg/cm^2 and used a 46% Pt/C catalyst (TEC10E50E, TKK) over NR-211 membrane [27].

3.1.2 Ex-situ characterization

Microstructure characterization of the electrodes was carried out using field emission scanning electron microscope (SEM) imaging (6301 - F, JEOL). Sample preparation involved freeze-fracturing the CCMs in liquid nitrogen before mounting them on SEM stubs for imaging. A cross-sectional image of the freeze-fractured samples gave an estimate of the CL thickness. A mean value of the thickness with the standard deviation from 15 locations was reported.

Density of Vulcan XC-72 carbon black needed to estimate the catalyst layer porosity was evaluated by using a mercury intrusion porosimeter (Poremaster 33, Quantachrome Instruments). Details regarding the experimental procedure have been described in Chapter 2. The averaged density value of carbon black was found to be 1.69±0.21 g/cm^3 based on 4 independent tests. This value of density was used for calculating the electrode porosities.

3.1.3 In-situ characterization

Electrochemical characterization was carried out using a potentiostat (VersaStat 4, Princeton Applied Research) and a fuel cell test station (Scribner Associates 850e system with back pressure unit). Cell performance was tested using flow-field plates with parallel channel configuration. Cyclic voltammetry (CV) and chronoamperametry experiments were conducted to measure the active area and hydrogen crossover of the cell (further details regarding the experimental parameters can be found in Ref. [74]). Galvanostatic polarization plots (scan rate of 0.1 A per point) were recorded at a cell temperature of 80°C at 50%, 70% and 90% RH. Six plots (three forward and three backward sweeps) were obtained for each of the aforementioned conditions. Tests were performed at a constant stoichiometic ratio of 10 with a minimum flow-rate of 0.2/0.4 slpm for anode and cathode respectively. The oxygen partial pressure was varied by using reactants having different oxygen concentrations, i.e., 1% oxygen (balance - N_2), 10% oxygen (balance - N_2) and ultra-zero compressed air (Praxair Inc.) as well as by increasing the cell pressure from 50 to 150 kPa (gauge) when operating with air. When operating at high cell pressures, both anodic and cathodic pressures were maintained at the same value. Table 3.1 shows the values of p_{O_2} calculated for the different cathodic reactants and operating conditions. The partial pressure of oxygen decreases from 50% to 90% relative humidity due to the increasing water vapor pressure in the system.

Table 3.1 – Oxygen partial pressure (p_{O_2}, kPa) with varying cathodic reactant and RH at 80°C

Cathodic reactant	50% RH	70% RH	90% RH
1% Oxygen (bal. N_2)	0.778	0.694	0.602
10% Oxygen (bal. N_2)	7.78	6.94	6.02
Air (ambient)	16.35	14.57	12.64
Air (50 kPaG)	26.98	25.21	23.28
Air (100 kPaG)	37.62	35.85	33.92
Air (150 kPaG)	48.27	46.48	44.56

Limiting current density experiments were carried out using hydrogen and 1% oxygen (bal. N_2) as the anodic and cathodic reactants. A constant stoichiometic ratio of 5 at 1 A was used, corresponding to a cathodic flow-rate of 3.9 slpm at 90% RH (details regarding the calculation for stoichiometic ratio is given in Appendix A). Voltage was scanned from 0.35 V to 0.05 V in steps of 25 mV (15 min./point) and the current was recorded at each point.

For each Pt loading, at least three independently fabricated samples were tested for each of the conditions discussed above, and an average value with error bars showing one standard deviation are reported.

3.2 Results and discussion

3.2.1 Microstructure characterization

Figure 3.1 shows the top and cross-sectional SEM images of CLs with varying Pt loadings. Figure 3.1 (a) shows the top surface of a 5L CCM where the porous structure consisting of catalyst particles can be seen. Figure 3.1 (b-d) shows the freeze-fractured side images of the 5L, 10L and 15L electrodes respectively. Evaluated thickness values for each of these electrodes is given in the figure. Figure 3.2 shows the variation in thickness along with its standard deviation with respect to Pt loading. It can be seen that the CL thickness appears to increase non-linearly with the number of deposited layers from 1.9±0.4 μm for 5 layers to 5.5±0.9 μm for 20 layers along with an increase in the standard deviation. Table 3.2 gives the values of Pt loadings and corresponding CL thicknesses. Doubling the number of deposited layers did not double the electrode thickness. This is thought to be due to the type of fabrication method used here. The deposition technique of inkjet printing may cause compactness with increasing number of printed passes. This resulted in a reduction in porosity as the Pt loading increased. Further work on improving the electrode pore-distribution and porosity at higher loadings using inkjet printing is needed.

CL porosity was estimated based on the ink composition, Pt loading and CL thickness values using the relationships given by Wang et al. [119]. Densities of Nafion and Pt are taken to be 2 mg/cm^2 and 21.5 mg/cm^2 respectively. The density of Vulcan carbon calculated using mercury intrusion porosimetry was found to be 1.69±0.21 g/cm^3. Table 3.2 gives the values of the calculated CL porosities for the different electrodes. The porosity decreased from 0.51 to 0.27 as the number of printed passes increased from 3L to 20L. For a cathodic Pt loading of 0.025 mg/cm^2, Owejan et al. [1] reported a CL thickness value of 11±1.2 μm using 5% Pt/C catalyst. This corresponds to a CL thickness of 2.75±0.3 μm when considering a 20% Pt/C catalyst. For this work, the measured value for a 5L CCM with similar Pt loading is 1.9±0.37 μm. In another case, Yu and Carter [137] reported a porosity value of 68.1% for their electrodes with ionomer/carbon ratio of 0.5. The higher value may partly be

(a)

(b)

(c)

(d)
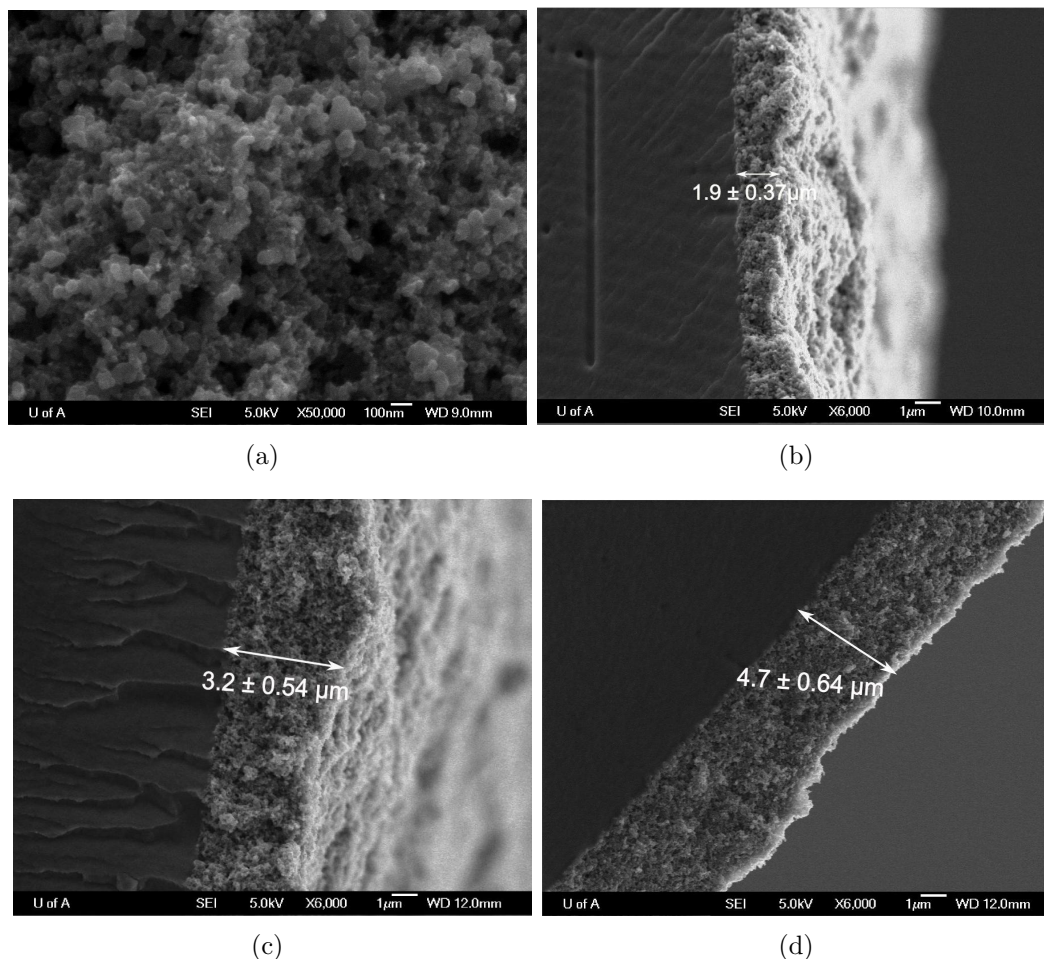
Figure 3.1 – SEM images of the IJP CCMs. (a) top surface of the CL (b-d) freeze-fractured side view images of CL samples showing thicknesses for the case of 5L, 10L and 15L samples respectively

due to the type of fabrication method used and partly due to the higher value of carbon density (2.2 g/cm^3) assumed in their case [137]. Gode et al. [138] reported electrode porosity and thickness values of 52% and 7.6 μm respectively for an electrode with Pt loading of 0.11 mg/cm^2 using 20% Pt/C catalyst. In our case, a similar Pt loading (0.113 mg/cm^2) and catalyst type produced electrodes with porosity and thickness values of 0.27±0.12 and 5.5±0.9 μm respectively. The comparison of CL thicknesses and porosities with other reported values may suggest that the type of fabrication method used in this work results in CLs with reduced thickness compared to conventional fabrication techniques.
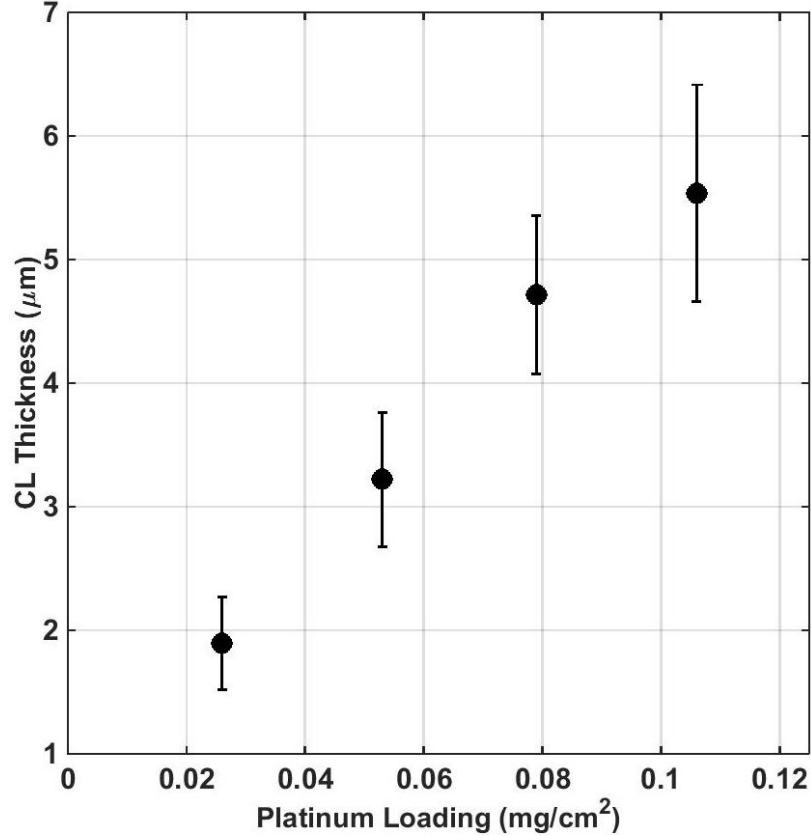
Figure 3.2 – Variation of CL thickness with Pt loading from 5L to 20L. A non-linear increase in thickness with the number of deposited layers suggests decreasing porosity

3.2.2 Performance dependence on Pt loading

Figure 3.3 show a plot of the corrected voltage (V_{iRfree}) with current density for the different Pt loadings at 50%, 70% and 90% RH, 80°C. The performance trends appear to be similar for all the three RH cases. In the kinetic region, electrode performance increased with Pt loading. The performance increase was substantially reduced above 0.056 mg/cm² and did not change after 0.08 mg/cm². In the transport limiting region, the performances of the 3L and 5L CCMs were low, whereas they appear to be fairly similar between 15L and 20L CCMs.

Figure 3.4 shows the variation of voltage with Pt loading for the inkjet printed samples at 90% RH and at current density values of 0.1 A/cm² and 1 /cm². For comparison, data from literature on the effect of Pt loading is shown in the figure. The measured voltage values varied in each case due to differences in the electrode operating conditions. The reported values of operating cell temperature and pressure

Table 3.2 – Inkjet printed electrode microstructure parameters

Number of printed layers	Platinum loading (mg/cm^2)	CL thickness (μm)	CL porosity
3	~ 0.014	~ 1	0.51
5	0.026±0.005	1.9±0.4	0.50±0.10
10	0.056±0.012	3.2±0.5	0.37±0.12
15	0.080±0.019	4.7±0.6	0.39±0.09
20	0.113±0.026	5.5±0.9	0.27±0.12

were 80°C and 150 kPa for the case of Owejan et al. [1], 35°C and 101 kPa for the case of Qi et al. [2] and 60°C and 135 kPa for the case of Saha et al. [3]. As seen in Figure 3.4, increase in the measured cell voltage with increasing Pt loading is substantial at low loading values below around 0.05 mg/cm^2. The threshold Pt loading is identified to be 0.08 mg/cm^2 (15L) for the IJP electrodes in this work. This value for the case of 20% Pt/C catalyst is in agreement with Qi and Kaufman [2] who observe a sharp performance increase from 0.022 to 0.083 mg/cm^2 after which the performance increase slowed down. Similar trends can be observed from the data of Owejan et al. and Saha et al. [1, 3], however the threshold Pt loading varied in these cases. Differences may arise from the fact that different catalyst types were used in these works, a factor which is known to affect the optimal Pt loading value [2].

3.2.3 Analysis of kinetic parameters

For the IJP electrodes, a reduced dependence of performance with Pt loading is observed in the kinetic and mass transport region. The plateau obtained in the mass transport region can be rationalized based on increased thickness and reduced porosity of the electrodes. To try and understand the reason for this plateau in performance gain in the kinetic region, analysis of kinetic parameters was carried out.

3.2.3.1 Electrochemical active area

Figure 3.5 shows the CV plots for CLs with 5, 10 and 15 deposited layers. The electrochemical active area was calculated based on the area under the curve with voltage range from 0.4 V to 0.1 V (hydrogen adsorption region) and assuming a charge of 210 μC/cm^2 to remove a mono-layer of protons from a smooth Pt surface [74]. An average value of the active area is given in Table 3.3 for the different Pt loadings. The overall active area increased from 88 cm$^2_{Pt}$ to 228 cm$^2_{Pt}$ as the Pt loading increased from 0.026 to 0.113 mg/cm^2. The specific active area per gram of Pt however decreased from 66±8 m^2/g to 40±3 m^2/g , suggesting that the catalyst availability dropped
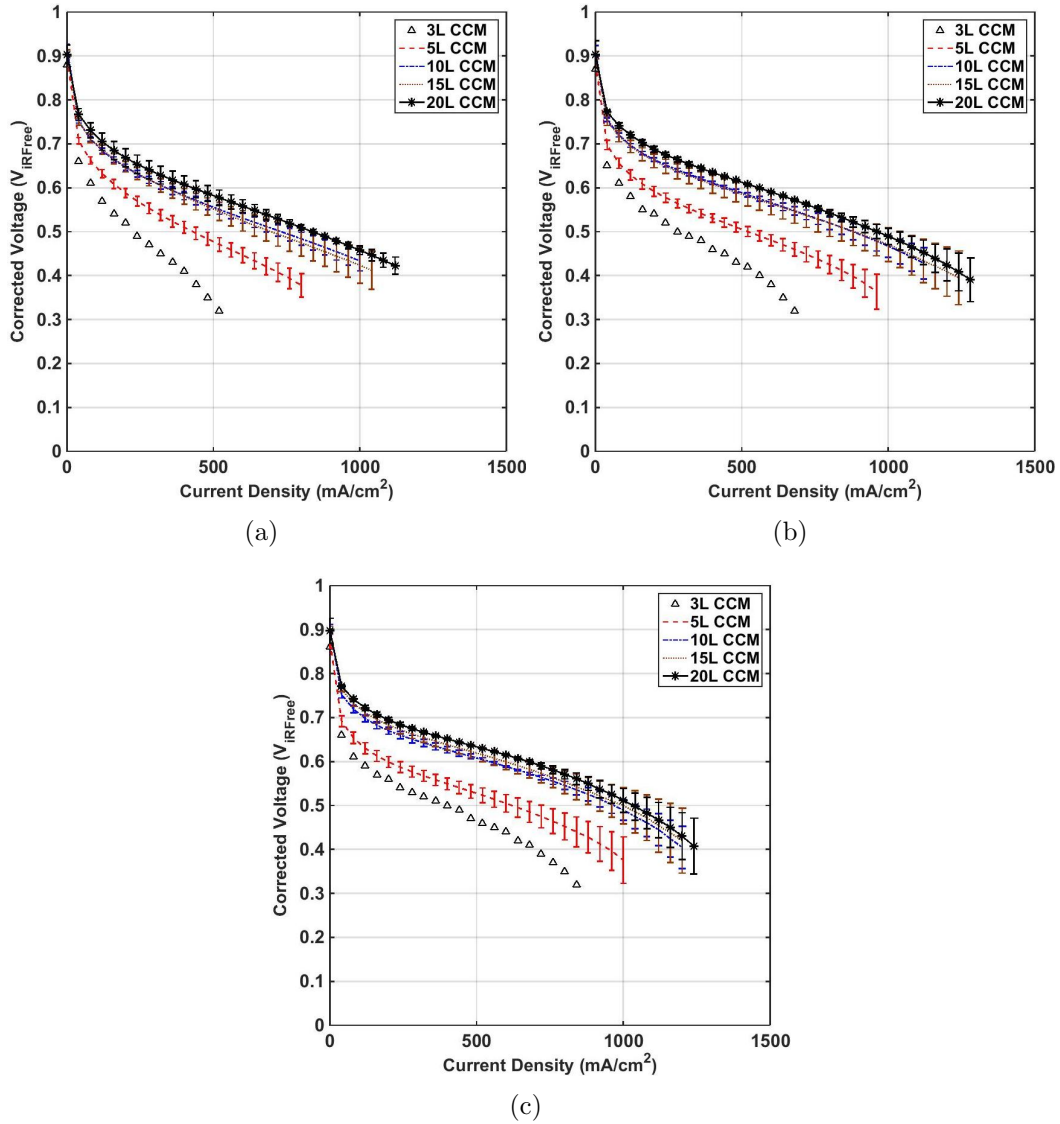
Figure 3.3 – Polarization plots at 80°C and ambient pressure for the different Pt loading cases using parallel channel configuration with H_2/air at a constant stoichiometic ratio of 10 with resistance corrected voltage (V_{iRfree}) (a) at 50% RH (b) at 70% RH (c) at 90% RH

with Pt loading. The measured active area values are in agreement with previously reported active area values for inkjet printed electrodes, e.g., 33.9 to 45.7 m^2/g [3].
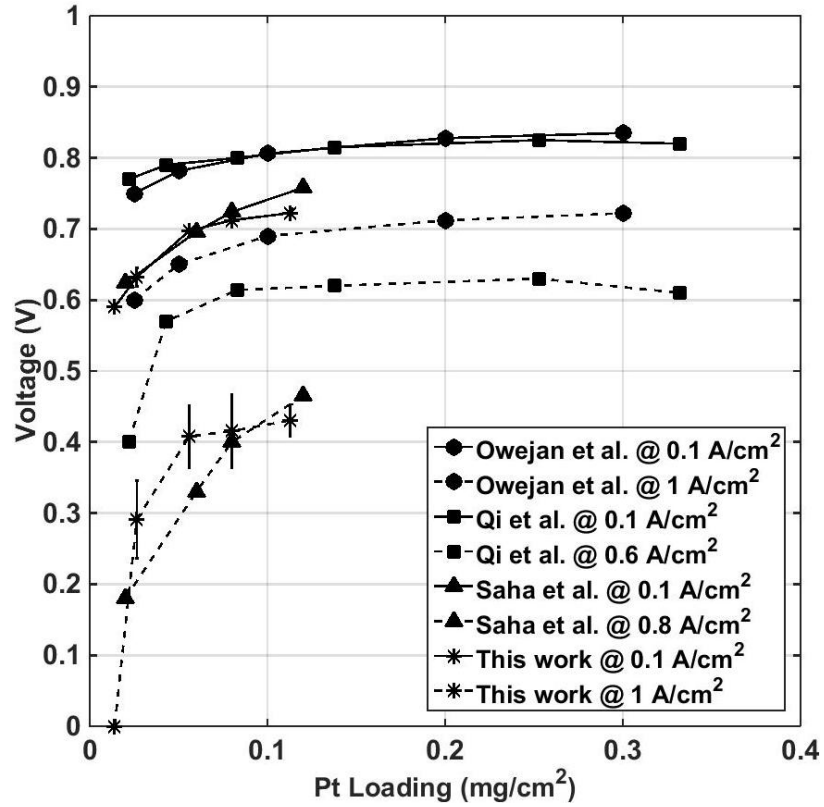
Figure 3.4 – Voltage variation for the IJP CCMs at 0.1 and 1 A/cm^2 at 90% RH, 80°C and ambient pressure. For comparison, literature data from Owejan et al. [1], Qi et al. [2] and Saha et al. [3] is shown at two current densities. The reported values of operating cell temperature and pressure are 80°C, 150 kPa for Owejan et al. [1]; 35°C, 101 kPa for Qi et al. [2] and 60°C, 135 kPa for Saha et al. [3]
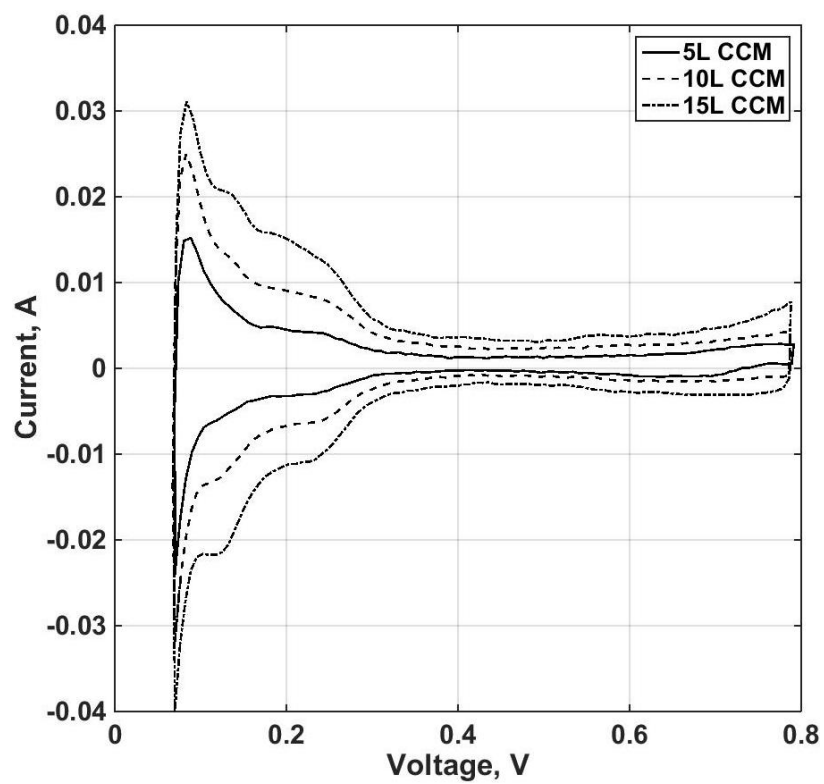
Figure 3.5 – Cyclic voltammetry plots for 5L, 10L and 15L electrodes at 30°C using fully humidified H_2/N_2

Table 3.3 – Kinetic parameters for the CLs with different Pt loadings operated at a constant stoichiometric ratio of 10 with parallel channel configuration using H_2/air at ambient pressure at 90% RH

Platinum loading (mg/cm^2)	Open cell voltage (V)	Active area (m^2/g)	Tafel slope (b, V/dec)	Charge transfer coefficient (α)	Exchange current density (i_o, A/cm$^2_{Pt}$)	Total reaction order ($m|_{0.75V_{iRfree}}$)
0.026±0.005	0.88±0.02	66±8	0.123±0.002	0.56±0.01	3.72±0.66×10^{-7}	1.02±0.18
0.056±0.012	0.90±0.01	54±6	0.104±0.003	0.67±0.02	1.46±0.08×10^{-7}	0.99±0.01
0.080±0.019	0.90±0.01	52±3	0.097±0.007	0.70±0.04	9.79±3.60×10^{-8}	1.03±0.13
0.113±0.026	0.92±0.01	40±3	0.093±0.001	0.74±0.01	5.97±0.38×10^{-8}	0.99±0.04
0.4 (SC)	0.92±0.05	49±8	0.068±0.001	1.00	1.44×10^{-9}	1.00

Saha, Kriston, and Cho et al. [3, 26, 139] also reported a decrease of specific active area with increased loading. Owejan et al. [1] on the other hand did not observe this decrease when the CL thickness was maintained constant. Therefore, the reduction in the active area might be fabrication specific and in this case, it might be due to the compaction of the layer with increased printer passes that reduce the accessibility of Pt to ionomer. The spray coated CCM exhibited a higher active area as compared to the inkjet printed CCMs. This may be due to the variation in the porosity and pore-distribution of the electrode structure because of the fabrication technique used.

Hydrogen crossover current was found to be between 2 - 4 mA/cm^2 at 0.5 V corresponding to a crossover flux between 1.03×10^{-8} and 2.07×10^{-8} mol/cm^{-1}s^{-1}. Variation in Pt loading was not found to affect the crossover value. The protonic electrode resistance obtained using potentiostatic EIS at 0% cathodic RH was found to increase from 66 mΩ.cm^2 for the 5L CCM to around 210 mΩ.cm^2 for the 20L CCM.

3.2.3.2 Tafel slope

The evaluation of electrode kinetics was carried out by testing CCMs with varying Pt loading at different oxygen partial pressure cases. All the p_{O_2} cases studied are given in Table 3.1. The Tafel slope, b, was evaluated by taking the first 5 points on the polarization curve (20-100 mA/cm^2; except when using 1% O$_2$ where the range was 5-25 mA/cm^2). Resistance corrected voltage, V$_{iRfree}$ obtained from current interrupt method was used for the analysis of the Tafel slopes. The value of resistance from current interrupt method was found to be comparable to that obtained at the high frequency intercept while performing EIS. The exchange current density, i_o and charge transfer coefficient, α was obtained from the intercept and slope of the plot between overpotential, η and $\ln(i)$ respectively. For the evaluation of i_o, η is defined with respect to the theoretical open cell voltage (OCV) that is based on the Nernst potential.

The kinetic parameters, Tafel slope, exchange current density, charge transfer coefficient and the OCV values for different Pt loading electrodes at 90% RH when operating with air (p_{O_2} = 12.6 kPa) are given in Table 3.3. The Tafel slope decreased from 123 mV/dec for the case of 5L CCM to 93 mV/dec for the case of 20L CCM. Figure 3.6 shows the Tafel plot for the case of a 20L CCM at different oxygen partial pressures. Figure 3.7 shows the variation in Tafel slope with Pt loading at the four p_{O_2} values. Unlike Subramanian [134] who report no dependence of Tafel slope on p_{O_2}, the Tafel slope of the IJP electrodes was found to decrease with increasing p_{O_2} and Pt loading. At p_{O_2} of 44.5 kPa, a drop in Tafel slope from around 120 mV/dec

to 80 mV/dec is observed followed by a constant value thereafter as the Pt loading increased from 0.026 mg/cm^2 to 0.056 mg/cm^2. The Tafel slope for the spray coated sample with a cathodic Pt loading of 0.4 mg/cm^2 was found to be lower than for the IJP samples. The Tafel slope for the spray coated CCM decreased from 0.092 V/dec to 0.064 V/dec as p_{O_2} increased from 0.6 kPa to 44.5 kPa.
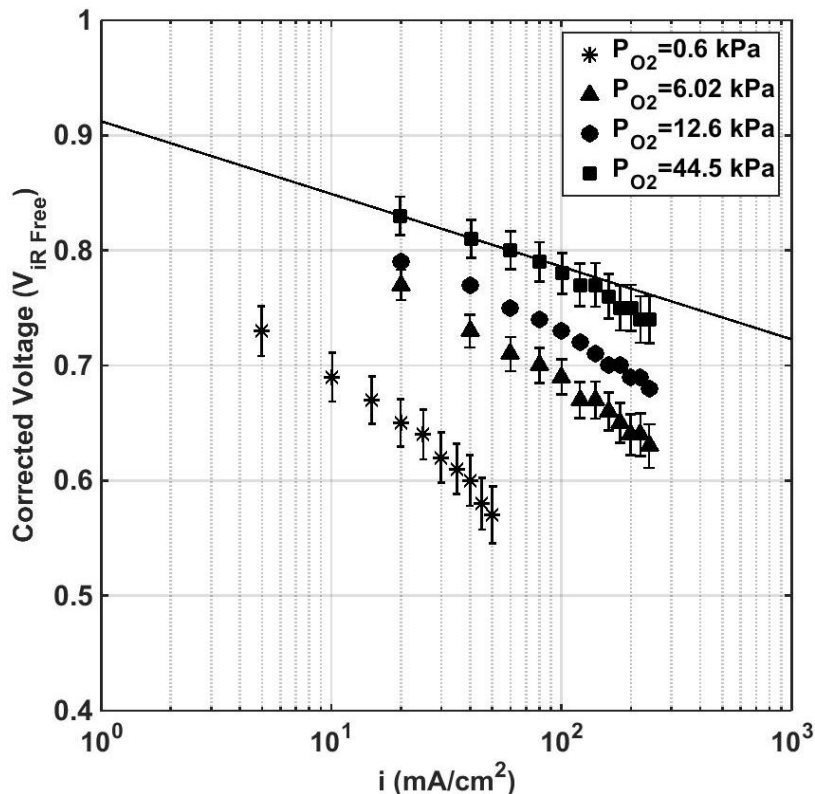
Figure 3.6 – Tafel slope analysis at 90% RH for the case of CL with 0.113 mg/cm^2 Pt loading (20L)

The change in Tafel slope from 120 mV/dec to 80 mV/dec observed in this work is likely due to a transition in oxygen reaction pathway. Evidence for the existence of a doubling of the Tafel slope has been observed experimentally over several decades [123–134], however the transition has usually been observed at high cell current and, therefore it has sometimes been attributed to mass transport. These results show that the transition from 60 mV/dec to 120 mV/dec is not controlled by mass transport but by overpotential. In the case of low loading electrodes, i.e, reduced active area, at low oxygen partial pressures, high overpotentials are required in order to achieve current densities of the order of 10 mA/cm^2, e.g., Figure 3.6. In this situation, the Tafel slope is recorded at a cell voltage below the transition overpotential, i.e., 0.7 to 0.9 V, and therefore only the so-called high current region of the Tafel

69
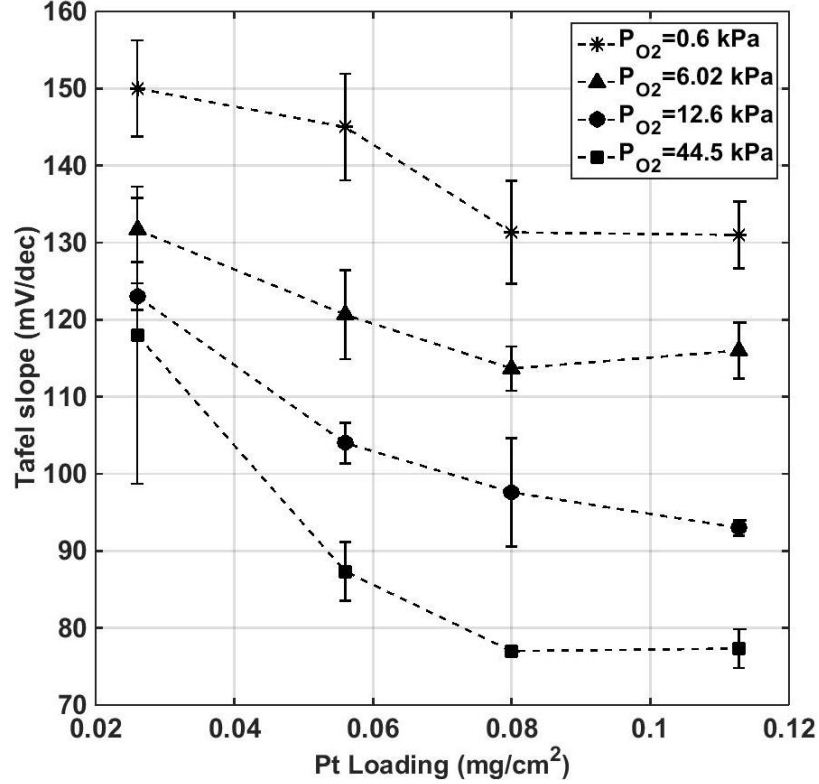
Figure 3.7 – Variation of b with Pt loading for p_{O_2} values of 0.6 kPa, 6 kPa, 12.6 kPa and 44.5 kPa

plot is accessible. These results provide further evidence of a changing Tafel slope indicating a transition in the oxygen pathway at a voltage in the range of 0.7 to 0.9 V.

It is interesting to note that previous studies with low loading electrodes, such as Kriston et al. [26] and Saha et al. [3], did not observe a changing Tafel slope. Instead, they observed a Tafel slope of 65 - 75 mV/dec and no change with Pt loadings. The reason for the difference is likely to be that they conduced their experiments at a higher oxygen partial pressure. Based on the reported operating conditions, their p_{O_2} values are 103 kPa for the case of Kriston et al. [26] and 24.5 kPa for the case of Saha et al. [3]. At high oxygen partial pressures, a constant Tafel slope with loading in the range of 70-90 mV/dec is also observed in this work.

Table 3.3 also shows the calculated exchange current densities, i_o, and charge transfer coefficients, α for all the tested CCMs. i_o decreased from $3.72\pm0.66\times10^{-7}$ to $5.97\pm0.38\times10^{-8}$ while α increased from 0.56 to 0.74 as Pt loading increased from 0.026 to 0.113 mg/cm^2 for the IJP CCMs. For the 20L CCM, the value of i_o is in the same order of magnitude to that reported by Neyerlin et al. [31] for their electrode

with a loading of 0.2 mg/cm^2 i.e., $2.47\pm0.3\times10^{-8}$ A/cm$^2_{Pt}$.

In the previous analysis, the cell voltage was not corrected for cross-over current, even though it can significantly lower the cell voltage. However, it is of interest to study the loss in cell voltage due to crossover in each case. Considering simple Tafel kinetics, the loss in overpotential, η, related to the hydrogen crossover current, i_x, can be calculated as [31]

$$\eta = \frac{2.303RT}{\alpha F} log \left[\frac{i + i_x}{m_{Pt}A_{Pt}i_o} \right] \tag{3.1}$$

where α is the transfer coefficient, m_{Pt} is the Pt loading in mg/cm^2, A_{Pt} is the electrochemical active area in cm^2/mg, i_o is the exchange current density in A/cm$^2_{Pt}$, and F is the Faraday constant (96,485 C/mol e$^-$). At open cell voltage, the overpotential associated with the crossover current of 3 mA/cm^2 is calculated to be 0.33 V, 0.29 V, 0.28 V and 0.28 V for 5L, 10L, 15L and 20L CCMs respectively based on the values given in Table 3.3.

3.2.3.3 Oxygen reaction order

We previously reported that inkjet printed electrodes showed an increased sensitivity to operating pressure as compared to conventional electrodes [7, 74]. The section above also highlights that low loading electrodes might operate in a different oxygen reaction pathway due to their low initial cell voltage. This might influence the observed MEA reaction order to oxygen. The sensitivity of the cell performance to oxygen partial pressure can be measured at a constant overpotential, η (giving a value of kinetic reaction order, γ) or at a constant V_{iRFree} voltage (giving a value of total reaction order, m) [31]. In this work, the focus is towards the latter case. The reaction order, m, is obtained at a constant cell voltage using [31]

$$m = \left(\frac{\partial lni}{\partial lnp_{O_2}} \right)_{V_{iRfree},T} \tag{3.2}$$

where i is the current density at a constant voltage and temperature. The reaction order was extracted from the slope of the line based on the plot of $\ln(i)$ vs. $\ln(p_{O_2})$ [74].

Figures 3.8 and 3.9 show the changes in the average current density values along with standard deviation at each p_{O_2} at 90% RH and voltages of 0.75 and 0.7 V$_{iRFree}$ respectively. Based on the figure, a linear relationship is observed for both the cases with a slope between 0.8 and 1 for the inkjet printed electrodes.
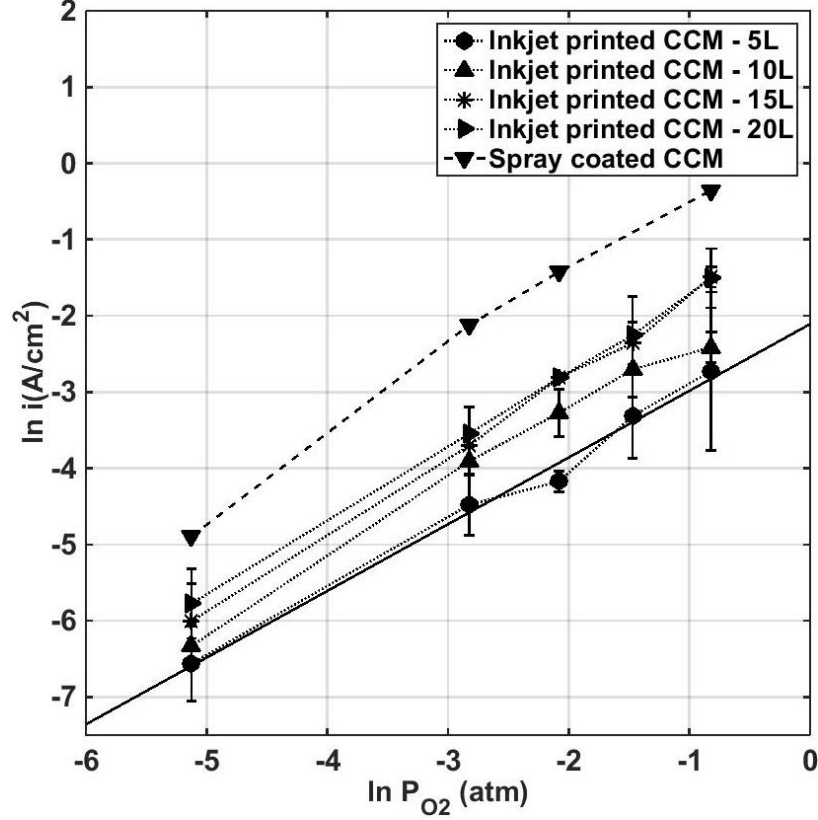
Figure 3.8 – Sensitivity of the cell performance to oxygen partial pressure changes for the case of inkjet printed and spray coated CCMs at 0.75 V_{iRFree} at 90% RH

In order to determine the kinetic reaction order, the overpotential at the electrode must be estimated. This estimation is however challenging due to the effect of crossover. In this work, the overpotenial is calculated using,

$$\eta = E_{th} - E_{cell} - \eta_{crossover} \tag{3.3}$$

where $\eta_{crossover}$ is the overpotential due to hydrogen crossover calculated using equation (3.1) while E_{th} and E_{cell} are the theoretical and measured cell voltages. E_{th} was calculated from the Nernst equation for each value of p_{O_2}. At a constant overpotential of 0.15 V_{iRFree}, the kinetic reaction order, γ was thus evaluated at the respective E_{cell}. The value of γ was found to be 0.68±0.14, 0.78±0.03, 0.80±0.08 and 0.84±0.08 for the case of 5L, 10L, 15L and 20L inkjet printed electrodes respectively at 90% RH. The kinetic reaction order can also be obtained using thermodynamic arguments as discussed in ref. [31], using the relationship between m and γ as $m=\gamma+\alpha/4$. Based on this relation, γ for the IJP electrodes appear to be between 0.6 and 0.85. Given that the overpotential has been estimated based on crossover, the total reaction order

72
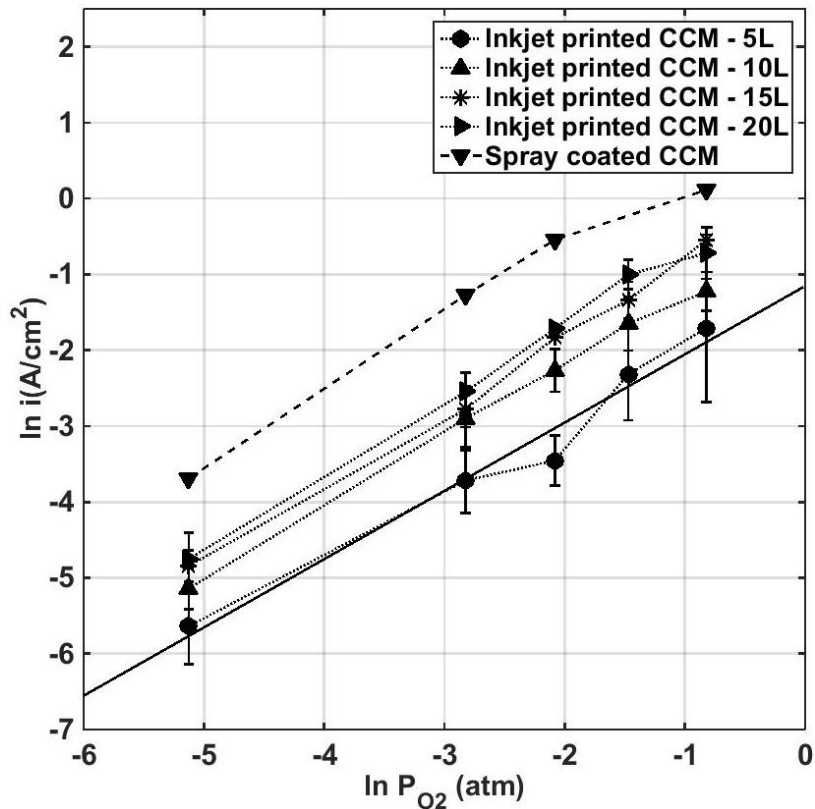
Figure 3.9 – Sensitivity of the cell performance to oxygen partial pressure changes for the case of inkjet printed and spray coated CCMs at 0.7 V_{iRFree} at 90% RH

results are more accurate.

Since no literature data on reaction order values for low Pt loading MEAs was found, the values of m obtained in this work were compared to the ones reported by Neyerlin et al. [31] and Subramanian et al. [134] for MEAs with higher Pt loadings. Table 3.3 provides values of the reaction order for the inkjet printed electrodes at a constant voltage of 0.75 V_{iRfree}. For an MEA with a conventional electrode with a Pt loading of 0.2 mg/cm^2, Neyerlin [31] reported a total reaction order of 0.79±0.02 for an MEA. Subramanian et al. [134] did not report individual reaction orders for their low Pt loading (0.06 mg/cm^2) and high Pt loading (0.4 mg/cm^2) samples, and an average value for m is given as 0.81±0.03 considering simple Tafel kinetics. The values of m measured for conventionally fabricated MEAs in the literature are in reasonable agreement with the observed values for m in this work. Discrepancies may arise from the variation in the type of catalyst, Pt loading and operating conditions used. The IJP electrodes show a similar reaction order to conventional spray coated

73

electrodes. This value shows that the reason for our previous observations showing that low loaded electrodes were more sensitive to an increase in the total cell pressure [7, 74] were not the result of a changing reaction order. It therefore appears that the reason for the observed increased performance with total pressure when compared to spray coated samples was the change in Tafel slope with increased oxygen partial pressure observed in Figure 3.7.
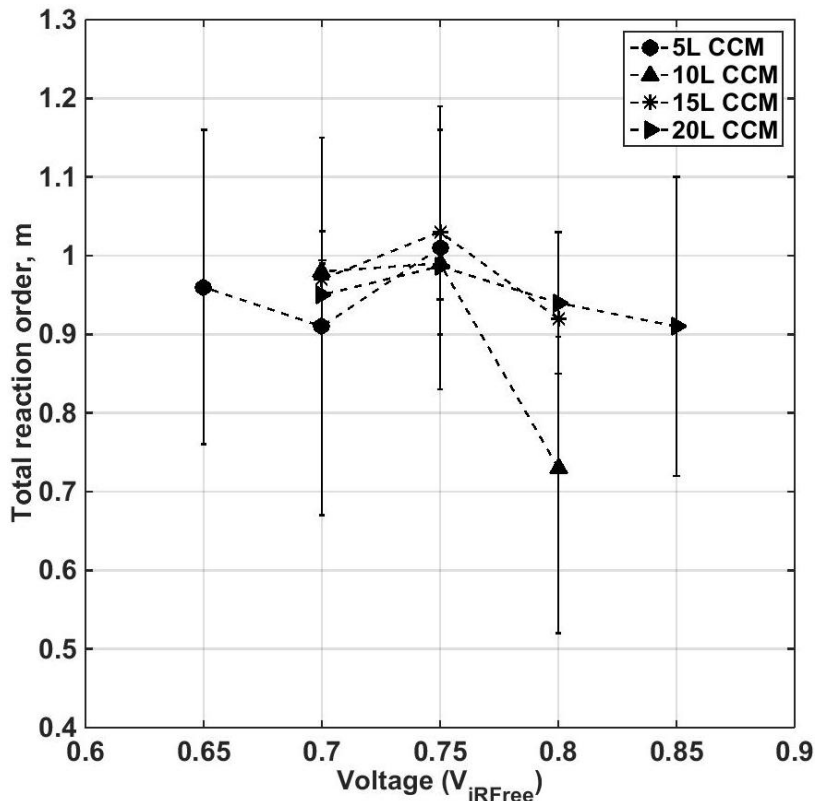
Figure 3.10 – Change in the total reaction order, m with voltage for the different Pt loadings at 90% RH, 80°C

Figure 3.10 shows the variation of m with the overpotential (between 0.85 and 0.65 V_{iRFree}). An average value of m with a standard deviation from three tested samples for each Pt loading is given. To avoid regions with mass-transport losses, the oxygen reaction order for cell voltages below 0.7 V_{iRFree} was not measured for the case of 10L, 15L and 20L CCMs. The 5L CCM could not reach higher potentials of 0.8 and 0.85 V_{iRFree} due to its reduced loading and thus, it was computed between 0.65 and 0.75 V_{iRFree} where the current density is below 0.5 A/cm^2. Figure 3.10 shows that, considering the error bars, m is nearly one for 10L, 15L and 20L electrodes except for the 10L electrode at a higher cell voltage. There have been contradicting trends

74

reported in the literature for the variation of the reaction order with overpotential [124, 134, 135, 140, 141]. Data from Markiewicz [141] and Parthasarathy [124], who used ex-situ techniques for determination of the reaction order, show that its value is either invariant or increases with cell voltage, respectively. In-situ measurement techniques used by Subramanian [134] and Uchimura [140] show that γ decreases with increasing cell voltage (V_{iRFree}). The apparent kinetic reaction order was reported to increase from 0.55 to 0.7 as the potential decreased from 0.875 to 0.65 V [134].

3.2.4   Oxygen transport resistance

Local mass transport losses have been considered responsible for the low performance of low loading electrodes, therefore this local transport resistance was measured for the inkjet printed electrodes with varying loading at different relative humidity conditions. The total oxygen transport resistance, R_{total}, at limiting current, i_{lim}, i.e., when the oxygen concentration at the catalyst surface approaches zero, is given as [42, 78]

$$R_{total} = \frac{4Fc_{O_2}}{i_{lim}} = \frac{4F}{i_{lim}} \frac{p_{O_2}}{RT} \tag{3.4}$$

where c_{O_2} is the gas channel oxygen concentration and i_{lim} is the measured limiting current density as discussed below. The limiting current was obtained using 1% oxygen as the cathodic reactant. Average limiting current with error bars showing the standard deviation obtained by testing three samples for the 5L, 10L, 15L and 20L electrodes at 50, 70 and 90% RH are shown in Figure 3.11.
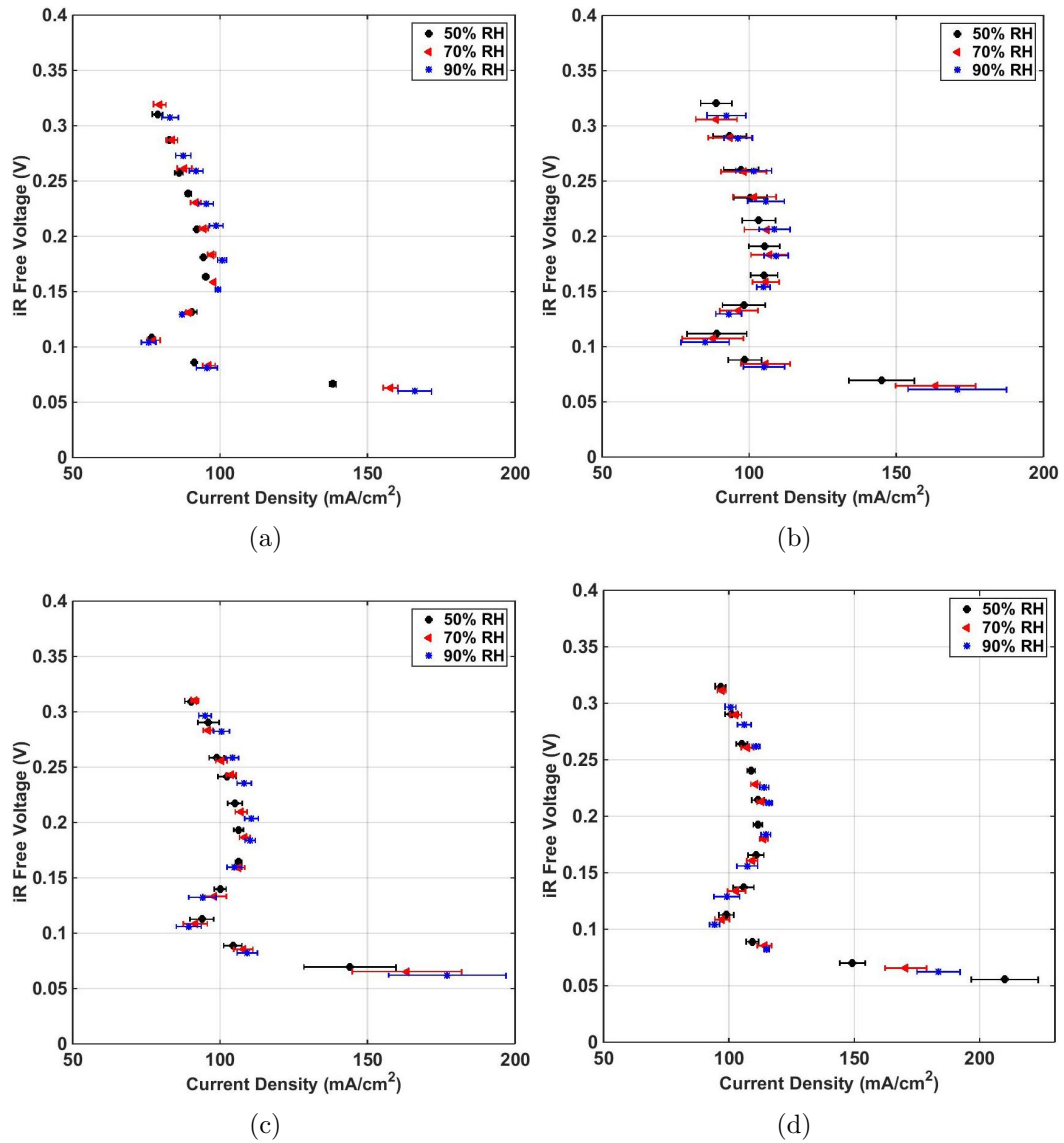
Figure 3.11 – Evaluation of limiting current density for the CCMs at 50, 70 and 90% RH. Error bars show the standard deviation from three tested samples (a) 5L CCM (b) 10L CCM (c) 15L CCM (d) 20L CCM

Between 0.2 and 0.1 V, the current density appears to decrease. This phenomenon has been observed in literature for conventionally fabricated electrodes and is believed to be the result of transition from a four electron process to a two electron process due to the formation of peroxide instead of water [42, 142, 143]. The transition in the electron transfer mechanism is not only a modification of the kinetics but also of the amount of current produced for the same oxygen flux. Assuming a limiting oxygen flux, N_{lim}, if the number of electrons produced at the Pt site is 4, then the amount of current produced per mole of oxygen would be $i_{lim} = 4FN_{lim}$. But if part of the reaction proceeds through a 2 electron pathway, the current produced will be reduced to $2FN_{lim}$. Therefore, even though the kinetics are not important because they are fast enough to consume all the oxygen that reaches the reaction site, the number of electrons produced will have an impact on the current. Below 0.1 V, the current density increases due to hydrogen evolution reaction [42]. For this study, the limiting current was specified to be the maximum current that was obtained above 0.1 V. A similar procedure has also been followed by Greszler et al. [42] for the measurement of their limiting currents.

Table 3.4 – Limiting current density (mA/cm^2) variation with Pt loading and RH

Pt Loading (mg/cm^2)	50% RH	70% RH	90% RH
0.0265	90.8±7.6	94.6±5.7	97.4±5.7
0.056	105.9±4.9	108±6	109.4±4.4
0.080	106.9±1	108.3±1.8	110.7±2.2
0.113	112.5±2.7	113.9±1.6	115.8±1.3

Table 3.4 shows the limiting current densities obtained for the different Pt loading cases at 50%, 70% and 90% RH. i_{lim} appears to increase with RH even though p_{O_2} decreases from 0.78 kPa to 0.6 kPa (from 50% to 90% RH). The reason for this may be linked to changes in the oxygen transport in the ionomer with RH.

Figure 3.12 shows the total transport resistance evaluated from Equation (3.4) vs. inlet humidity for the cases with varying Pt loading. For comparison, data from Nonoyama et al. [4] is also shown in the figure. Even though the electrode type and operating conditions are different, the same trend is observed. The total transport resistance for the inkjet printed electrodes decreased with increasing RH. From 50% to 90% RH, R_{total} decreased from 1.13 to 0.81 s/cm for 5L CCM, 0.97 to 0.72 s/cm for 10L CCM, 0.96 to 0.71 s/cm for 15L and 0.9 to 0.68 s/cm for the case of 20L CCM. In comparison, R_{total} decreased from 0.89 to 0.79 s/cm as RH increased from
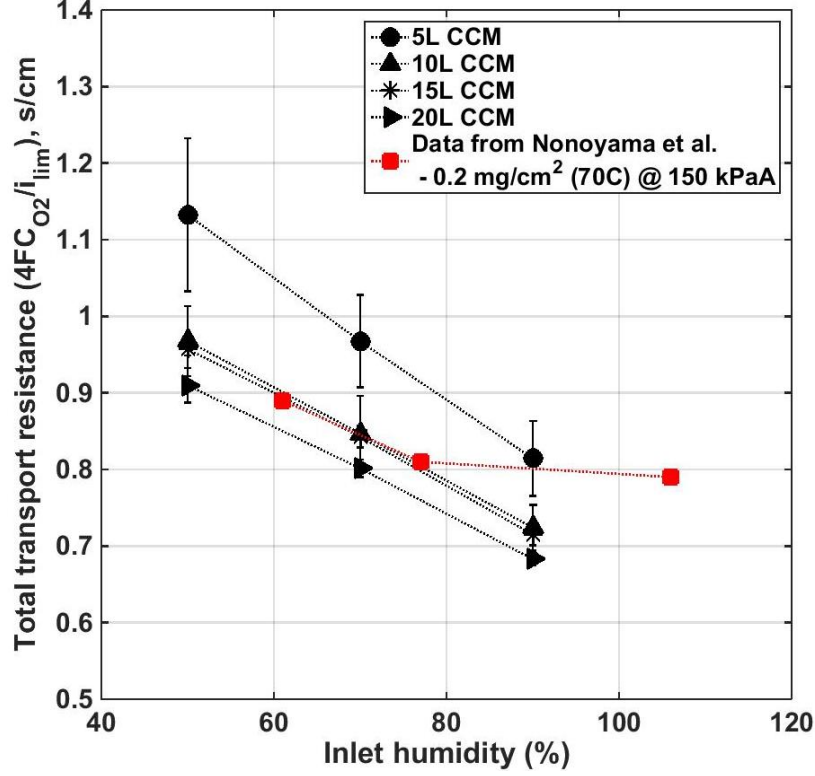
Figure 3.12 – Total oxygen transport resistance (R_{total}) calculated from Equation (3.4) vs. RH for the inkjet printed CCM and its comparison to the literature data from Nonoyama et al. [4]

61% to 106% based on the data from Nonoyama et al. [4].

The transport resistance near the Pt surface, i.e., local oxygen transport resistance, $R_{O_2}^{Pt}$ is related to R_{total} by the following relationship based on the analysis of Greszler et al. [42]

$$R_{total} = R_{Ch} + R_{DM} + \frac{R_{O_2}^{Pt}}{f_{Pt}} \left(\frac{h}{\psi} \right) coth \left(\frac{h}{\psi} \right) \tag{3.5}$$

where R_{Ch} and R_{DM} are the transport resistances through the flow-channels and gas diffusion media, f_{Pt} is the roughness factor which is given as the product of the Pt loading and electrochemical active area, h is the electrode thickness and ψ is a quantity with units of length represented as [42],

$$\psi = \sqrt{D_{O_2}^{eff} \frac{h R_{O_2}^{Pt}}{f_{Pt}}} \tag{3.6}$$

For the various IJP electrodes, Figure 3.13 shows the variation of the dimensionless term (h/ψ)coth(h/ψ) with the local oxygen transport losses $R_{O_2}^{Pt}$, assuming the effective diffusivity ($D_{O_2}^{eff}$) to be 0.0241 cm^2/s [137]. It can be seen that (h/ψ)coth(h/ψ)
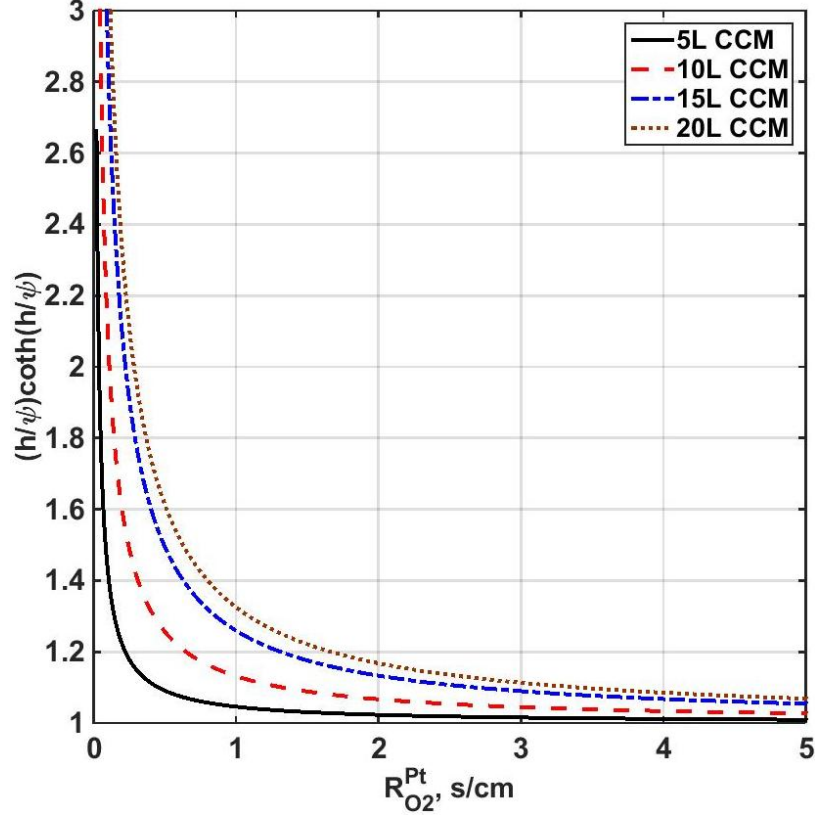
Figure 3.13 – Variation of $(h/\psi)\coth(h/\psi)$ with $R_{O_2}^{Pt}$ for the IJP CCMs considering a $D_{O_2}^{eff} = 0.0241$ cm^2/s

approaches unity as $R_{O_2}^{Pt}$ increases and can be neglected from the Equation (3.5), thus reducing it to [42]

$$R_{total} = R_{Ch} + R_{DM} + \frac{R_{O_2}^{Pt}}{f_{Pt}} \tag{3.7}$$

$R_{O_2}^{Pt}$ was obtained from the slope of the line based on the plot of R_{total} vs. $1/f_{Pt}$ as shown in Figure 3.14. Table 3.5 shows the average local transport resistance from three tested samples for the inkjet printed electrodes and local transport resistances reported in the literature for comparison along with the operating conditions for the cell. For the inkjet printed electrodes, the value of $R_{O_2}^{Pt}$ was found to decrease from 5.93±3.16 s/cm to 3.43±1.67 s/cm as RH increased from 50% to 90%. The values are in agreement with those reported by Greszler et al. [42] and Owejan et al. [1] who have reported $R_{O_2}^{Pt}$ to be 9.2 s/cm and 4.2 s/cm at 62% RH and 80% RH respectively. Therefore, the local mass transport resistances of inkjet printed electrode are similar to those of conventional electrodes. Regarding the drop in the oxygen transport resistance with RH, it might be associated with the changes in the oxygen interfacial resistance. In their recent study using MD/DFT simulations Jinnouchi et al. [83]
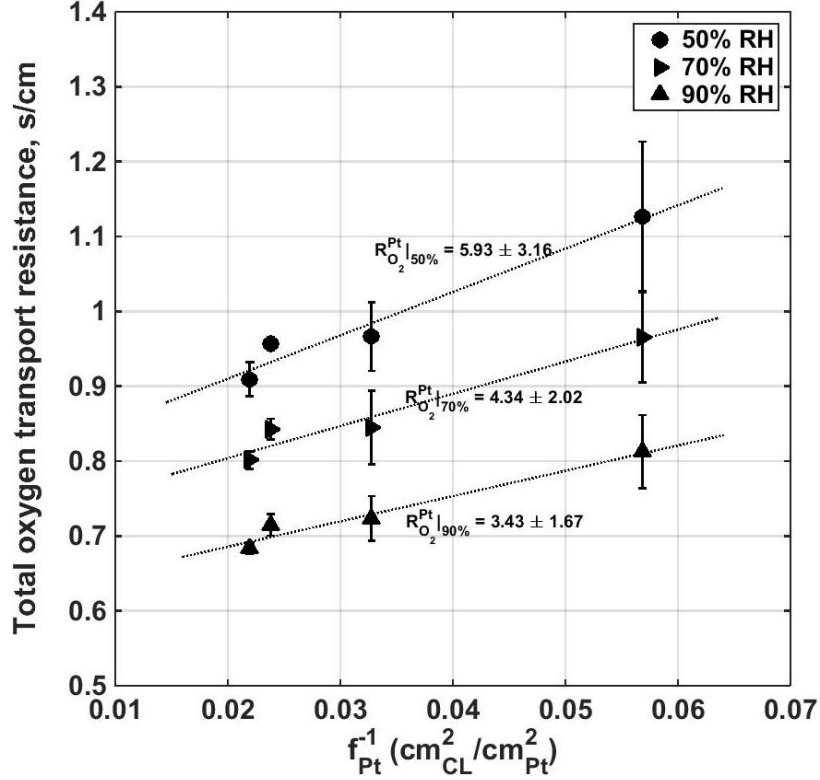
Figure 3.14 – Plot of R_{total} vs. $1/f_{Pt}$ at 50%, 70% and 90% RH. Slope of the lines give the value of $R_{O_2}^{Pt}$ at the respective RH

predicted that oxygen permeation through the ionomer film would not be dependent on water content. The measured reduced local resistance at high RH in this work appears to contradict the simulation results. Further study in this area is therefore necessary.

Table 3.5 – Comparison of local oxygen transport resistance $R_{O_2}^{pt}$ with data from literature

Research Group	$R_{O_2}^{pt}$ (s/cm)	Operating conditions
Greszler et al. [42]	9.2	110 kPaA, 62% RH
Owejan et al. [1]	4.2	110 kPaA, 80% RH
This work	5.93±3.16	101 kPaA, 50% RH
This work	4.34±2.02	101 kPaA, 70% RH
This work	3.43±1.67	101 kPaA, 90% RH

80

3.3 Conclusion

Inkjet printed electrodes with varying Pt loadings from 0.014 mg/cm^2 to 0.113 mg/cm^2 were fabricated and analyzed. Ex-situ characterization showed that the CL thickness increased from $\sim$1 μm to 5.5±0.9 μm with varying loading. Electrode porosity was found to drop from 51% to 27±12% with increasing Pt loading as the number of printed passes increased from 3 to 20 layers. The electrode active area decreased from 66±8 m^2/g to 40±3 m^2/g as the Pt loading increased from 0.026 to 0.113 mg/cm^2. The reduced porosity and active area with increased number of passes lead to a threshold on Pt loading above which gains in cell performance are substantially reduced.

A kinetic study showed that the Tafel slope increased with decreasing Pt loading and oxygen partial pressure. At high loading and oxygen partial pressures, the expected Tafel slope of 60-80 mV/dec was observed. At low loadings and low oxygen partial pressures however, the Tafel slope was measured to be over 120 mV/dec. At these conditions, the Tafel slope was obtained by fitting kinetic data at low current densities, but at cell voltages below 0.7 - 0.8 V$_{iRFree}$. At these cell voltage, the oxygen reduction reaction is known to change mechanism [123–134]. These results suggests that the change in Tafel slope might play a key role on limiting the performance of low loading electrodes.

A higher sensitivity to changes in total pressure in low loading electrodes compared to conventional electrodes have been observed before in this work [7, 74]. In order to understand the reason for the change in sensitivity, the total reaction order of varying loading IJP electrodes were measured. The reaction order was measured to be approximately one for all tested electrodes and similar to that of a spray coated electrode. The observed performance improvement with changes in total pressure for low loading electrodes is therefore not due to a change in reaction order. It is likely due to the observed decrease in Tafel slope with increased partial pressure.

The total and local oxygen transport resistance was also evaluated by carrying out limiting current experiments for the IJP electrodes. The total oxygen transport resistance increased with decreased loading as reported in previous publications [1, 4, 42]. The local transport resistance of the IJP electrodes at high relative humidity was also in agreement with those reported for conventional electrodes by Nonoyama et al. [4], Greszler et al. [42] and Owejan et al. [1]. Therefore, IJP electrodes do not show an

increased local oxygen transport resistance compared to conventional methods. In this work, the local transport resistance for the IJP electrodes was also measured at varying relative humidity and shown to decreased from 5.93±3.16 to 3.43±1.67 s/cm as the RH increased from 50% to 90%.

Based on the characterization studies, the performance of low loading electrodes appears to be limited by two mechanisms: (a) local oxygen transport resistance, and (b) reduced reaction kinetics due to its operation below 0.8 V. The latter can be mitigated by reducing crossover and increasing the cell operating pressure. Inkjet printed electrodes exhibit a lower performance than conventional low loading electrodes such as those in ref. [1]. The origin of the reduced performance is still uncertain, but possible reasons are: (i) operating conditions, e.g., Owejan et al. [1] operate with backpressures of 50 kPa(g) whereas the inkjet printed electrodes operate at ambient pressure (ii) low specific Pt area of inkjet electrodes (40-50 m^2/g for moderate loadings compared to conventional electrodes – Owejan et al. reported 60 to 80 m^2/g in Fig. 3a in ref. [1]); and, (iii) very low porosity of inkjet printed electrodes at higher Pt loadings (as low as 27% for moderate loadings). All these effects contribute to the 100-300 mV difference compared to conventionally fabricated electrodes as shown in Figure 3.4.

Chapter 4

Fabrication and testing of electrode coated membranes

The controlled deposition process of inkjet printing has allowed fabrication of low and medium Pt loading CLs as described in the previous chapters. Here, micro-porous layers of controlled thickness were fabricated over the CLs forming a novel electrode coated membrane (ECM) architecture. Section 4.2 describes the experimental materials and methods used for preparation and characterization of the electrodes. Section 4.3 discusses the SEM imaging of the fabricated ECM and MPLs and their performance and limiting currents at different operating conditions.

4.1 Introduction

As discussed in chapter 1, the microporous layer is an intermediate layer between the catalyst layer and gas diffusion layer intended for efficient water removal from the CL and to reduce the electronic contact resistance between the CL and GDL [11, 12]. Figure 4.1 shows the MPL location within the anodic and cathodic sides of the MEA.
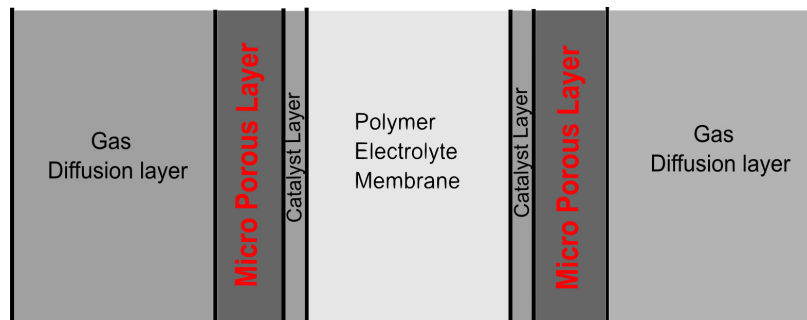
Figure 4.1 – Schematics showing the MPL within the membrane-electrode-assembly of PEFC

Since the MPL is usually fabricated over the GDL surface which has a higher porosity, it intrudes into the GDL pores resulting in a non-uniform thickness of the diffusion media [144]. In this work, the micro-porous layer is fabricated over the CL using inkjet printing. The controlled deposition technique allowed for a uniform and controlled thickness of the fabricated MPLs.

4.2 Materials and methods

4.2.1 Ink Preparation and MEA fabrication

The ink in this work is a modified version of the previously used recipe for catalyst ink preparation [74]. The ink consisted of 37.5 mg of the 40% Pt/C catalyst (Alfa Aesar) mixed with a 50/50 blend of propylene glycol and isopropanol (Fisher Scientific). Nafion ionomer (5 wt%, Ion Power) was added drop-wise during bath sonication of the ink to maintain a Nafion loading of 30 wt%. The ink was then placed in a waterbath and probe sonicated for 15 minutes. The water bath helped to prevent heating of the ink sample during the sonication process.

The carbon based ink for MPL fabrication was formulated by mixing 37.5 mg of Vulcan XC72R carbon black (Fuel Cell Store) with ethylene glycol, isopropanol and 30 wt% Nafion ionomer. The mixing and sonication was carried out similar to the catalyst ink recipe described before.

Details regarding the electrode fabrication process can be found in chapter 2. A commercially available Dimatix 2831 inkjet printer was used. The ink was filled in the printer cartridge and jetted over a Nafion membrane - NR211 (Ion Power). 10 passes of 5 cm^2 were printed on both sides of the membrane and the CCM was dried in the oven at 80±2°C for at least 3 hours. The electrode coated membrane consisted of 20 passes of the carbon/Nafion layer over the 10 passes of catalyst layer on both anodic and cathodic sides of the membrane. A cathodic ECM consisting of 20 passes of carbon layer only on the cathode electrode was fabricated and tested and the results showed a similar performance to the ECM. It was observed that printing the carbon layer over the CL or Nafion without removing the back-cover of the membrane resulted in membrane deformation and surface cracks during the deposition process. Thus, the back-cover of the membrane was removed prior to printing the carbon layers. After fabrication, the ECM was dried in the oven and stored for further use.

4.2.2 Microstructure and electrochemical characterization

Scanning electron microscopy (JEOL 6301F and Zeiss Evo MA10 SEM) was used for imaging the CL and MPL microstructure and thickness. Samples were freeze-fractured in liquid nitrogen prior to mounting them on the SEM stubs. Average thickness with a standard deviation from 15 different locations is reported. Pt loading and carbon loading was estimated from gravimetric analyses by using an Aluminum foil as a substrate. The weight difference before and after electrode fabrication was used to calculate the value of loading for each sample. The average CL Pt loading based on three measurements was found to be 0.10±0.01 mg$_{Pt}$/cm^2 after 10 printed layers whereas the average carbon loading for the MPL after 20 printed passes was measured to be 0.51±0.08 mg/cm^2. This value of carbon loading is very close to the optimal carbon loading of 0.5 mg/cm^2 in the micro-porous layer reported by Park et al. [145].

The porosity of catalyst layer was calculated using equations (2.6 - 2.8) given in chapter 2. Porosity of the carbon layers was evaluated using the following,

$$\epsilon_V = 1 - \left(\frac{m_C}{L} \cdot \frac{1}{\rho_C} + \frac{m_C}{L} \cdot \frac{Y_{el}}{1 - Y_{el}} \cdot \frac{1}{\rho_{el}} \right) \tag{4.1}$$

where m_C is the carbon loading in g/cm^2. Density of Nafion is taken as 2 g/cm^3, while the density of carbon, evaluated using mercury intrusion porosimetry, is 1.69 g/cm^3 (details regarding the experiment are given in chapter 2).

A Scribner Associates 850e fuel cell test station was used for obtaining galvanostatic polarization plots for the cells. The fabricated samples were sandwiched between either Sigracet 24BA or 24BC diffusion media by using 5 cm^2 single serpentine flow-field bipolar plates. The limiting current density experiments were performed using 5 cm^2 parallel flow-field plates for testing. After its assembly, the cell was conditioned using humidified H$_2$/air at 80°C at currents from 0.1 A to 5 A (conditioning protocol is given in Appendix A). Polarization plots were recorded galvanostatically at current intervals of 0.1 A/point (45 sec./point) at 50%, 70% and 90% relative humidity for H$_2$/air (0.2/0.4 slpm) at a cell temperature of 80°C and at 60°C for 50% and 90% RH cases. Three forward and three backward sweeps for the polarization plots at each operating condition were measured and an average of the three forward plots was obtained. Limiting current density experiments were carried out using hydrogen and 1% oxygen (bal. N$_2$) as the reactants at a stoichiometric ratio of 5 at 1 A. Voltage was scanned from 0.3 V to 0.03 V in steps of 25 mV (10 min./point) and the current

was recorded at each point.

The Tafel slope, b was evaluated using *FCView* software and confirmed by evaluating the slope based on a plot of $\ln(i)$ vs. η. The initial five current density points of the iR corrected polarization plot were used to determine the Tafel slope. Electrochemical impedance spectroscopy (EIS), cyclic voltammetry and chronoamperametry tests were performed using a potentiostat (Versastat 4, Princeton Applied Research) in order to quantify the electrode and proton transport resistance, electrochemical active area and hydrogen crossover respectively. The experimental parameters used for testing were the same as described in chapter 2.

4.3   Results and discussion

Two type of electrodes were fabricated, (a) catalyst coated membrane with 10 printed layers at anodic and cathodic electrodes tested using a 24BA and 24BC GDLs and (b) an electrode coated membrane consisting of 10 layers of the catalyst ink and 20 layers of carbon/Nafion ink that was tested using a 24BA GDL. Electrodes tested using 24 BA as the diffusion media are denoted as CCM24BA whereas those tested using 24 BC as the diffusion media are denoted as CCM24BC. In order to test the repeatability, three samples each of ECM, CCM24BA and CCM24BC were fabricated and tested for each of the conditions and the average plot with the error bars representing the standard deviation is reported.

4.3.1   Ex-situ SEM analysis

Figure 4.2 shows the microstructure of the fabricated samples. The top surface of the catalyst layer consists of evenly distributed Pt/C particles binded with the Nafion ionomer. Figure 4.2 (b) shows the freeze-fractured side image of the CL. The CL thickness is found to be 3.4±0.6 μm. Figures 4.2 (c) and (d) show the side view images of 20 and 40 printed carbon layers over Nafion with the measured thickness values of 5.6±0.5 μm and 10.9±0.3 μm respectively. These images show that it is possible to fabricate MPLs with a controlled thickness using the inkjet printing technique. Figure 4.2 (e) shows the SEM image of the electrode coated membrane. The catalyst layer and carbon layer could be distinguished here and have been denoted in the figure.

Figure 4.3 shows the back-scattered image of the electrode coated membrane.

(a)

(b)

(c)

(d)

(e)
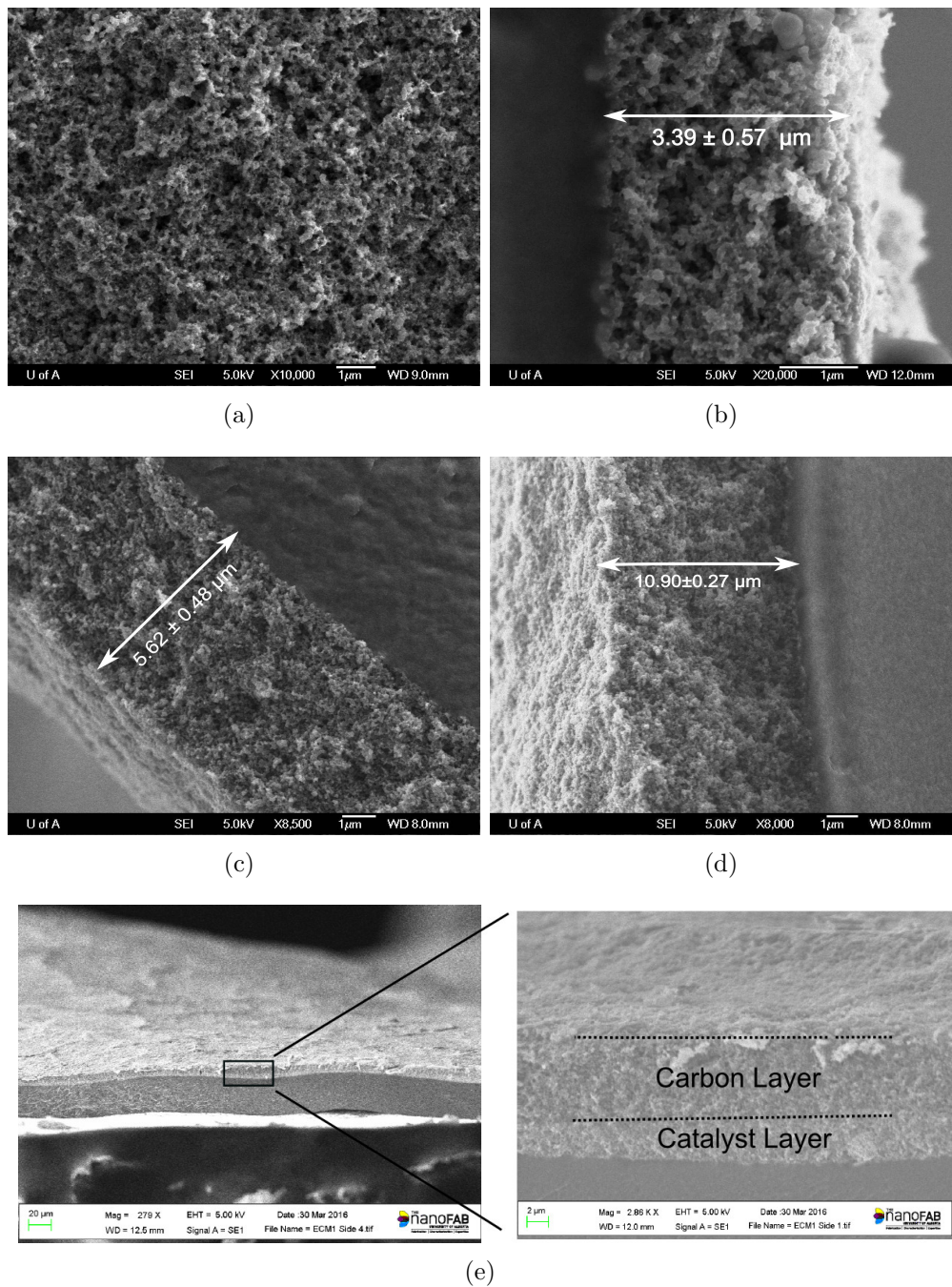
Figure 4.2 – SEM image of the inkjet printed electrodes (a) top surface of the catalyst layer (b) catalyst coated membrane after 10 printed passes (c) carbon coated membrane after 20 printed passes (d) carbon coated membrane after 40 printed passes (e) cross sectional image showing the electrode coated membrane

Since, the heavy Pt particles back scatter the electrons more strongly than rest of the elements in the microstructure, the CL can be identified by a bright band in the back-scattered mode.
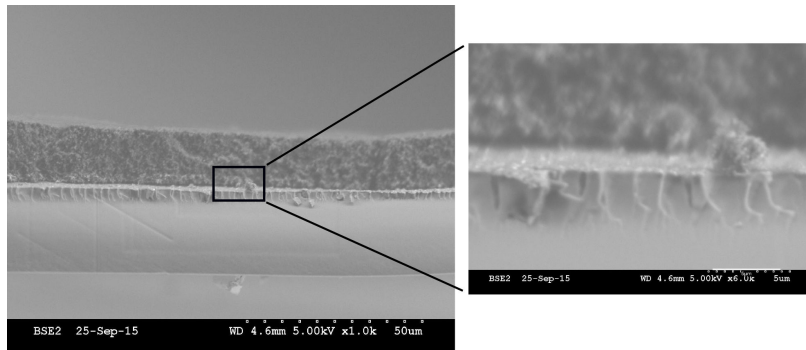
Figure 4.3 – Back-scattered SEM image of the ECM

Table 4.1 gives the thickness and porosity values of the fabricated microstructures. Porosity of the CL after 10L was 0.56±0.07. For the case of carbon layers, there was a slight drop in the thickness with increasing number of passes, as evident from the values given in the table. Based on a measured carbon loading of around 0.026 mg/cm^2 per printed passes, the porosity of the 20L and 40L carbon layers was found to be 0.26±0.07 and 0.24±0.02 respectively. The total thickness of ECM was found to be 10.4±1.7 μm. The thicknesses of the CL and carbon layer in the ECM were found to be 3.6±0.9 μm and 6.8±0.8 μm respectively and its porosity was calculated to be 0.47±0.18.

Table 4.1 – Microstructural parameters

Inkjet printed microstructure	Thickness (μm)	Porosity
10L catalyst layer	3.4±0.6	0.56±0.07
20L carbon layer	5.6±0.5	0.26±0.07
40L carbon layer	10.9±0.3	0.24±0.02
electrode coated membrane	10.4±1.7	0.47±0.18

4.3.2 In-situ analysis

4.3.2.1 Electrochemical measurements

Table 4.2 shows the average active area, Tafel slope, exchange current density, crossover, OCV and resistances for the tested electrodes. The H_2 crossover at 0.5 V was less than 1 mA/cm^2 for all the electrodes. Corresponding with the variation in crossover,

the OCV for CCM24BC was found to be the highest at 0.91±0.01 and lowest for ECM at 0.87±0.01. Active area values of the ECM and CCM24BC are similar and higher than that of CCM24BA. Since the Pt loading in all the three cases were similar, the difference in active area may be related to the accessibility of the catalyst for the reaction. The active area values appear to be lower than the one reported in chapter 3 for a similar Pt loading. The difference in the type of catalyst used, i.e., 20% Pt/C vs. 40% Pt/C may explain this discrepancy. The measured active area values for the ECM and CCM24BC are similar to the value reported by Saha et al. [3] for their IJP electrode with a Pt loading of 0.12 mg/cm^2 using 40% Pt/C (33.9 m^2/g). Measured Tafel slopes at 90% RH are lowest for CCM24BC and higher for the ECM and CCM24BA which is indicative of the higher kinetic performance of CCM24BC compared to the others. The measured exchange current density at 90% RH was highest for CCM24BA followed by ECM and CCM24BC. The electrode resistance was measured from EIS using 0.1 slpm H$_2$/N$_2$ at the anode and cathode respectively. The cathodic humidity was set at 0% RH in order to achieve the 45° slope at high frequencies needed for quantification of the protonic resistance. The calculated electrode resistance for the three samples are given in the table 4.2. The electrode resistance of ECM was found to be 114 mΩ.cm^2 whereas for CCM24BC, it was around 75 mΩ.

EIS was also used to observe the impedance response at a current of 200 mA/cm^2 using H$_2$/air at 50% and 90% RH, 80°C. For all the cases, a fluctuation free semi-circular Nyquist plot was obtained suggesting that it is representative of a simple Randles circuit. The high frequency x-intercept of the real impedance indicates the ohmic resistance of the cells [116]. At 50% RH, the values were found to be 42, 63 and 34 mOhm whereas at 90% RH, the values obtained were 25, 40 and 19 mOhm for the case of ECM, CCM24BA and CCM24BC respectively. These values were in reasonable agreement with the ones obtained using current interrupt method as discussed further. The charge transfer resistance, R$_{ct}$ at 90% RH was found to be 101 mΩ, 120 mΩ and 111 mΩ for the ECM, CCM24BA and CCM24BC respectively. The higher value of R$_{ct}$ for CCM24BA is most likely due to its lower measured active area.

4.3.2.2   Electrode performance comparison

Figures 4.4 and 4.5 show the average polarization plots and the current interrupt resistances for the three cases at 90% and 50% RH respectively with the error bars representing one standard deviation from three tests for each sample. For the polar-

Table 4.2 – Comparison of kinetic parameters for the case of ECM, CCM24BA and CCM24BC

Type of electrode	Hydrogen crossover current @ 0.5 V (mA/cm^2)	Open cell voltage (V)	Active area (m^2/g)	Tafel slope at 90% RH, 80°C (mV/dec)	Exchange current density at 90% RH (A/cm$^2_{Pt}$)	Electrode resistance (mΩ.cm^2)
ECM	0.99±0.18	0.87±0.02	32±5	115.66±5.32	2.52±1.30×10^{-7}	104±12
CCM24BA	0.90±0.16	0.90±0.01	27±5	115.10±5.44	2.58±0.18×10^{-7}	126±25
CCM24BC	0.69±0.06	0.91±0.01	33±3	101.53±6.11	1.38±0.53×10^{-7}	78±8

ization plots, iR compensated voltage from the current interrupt resistance is plotted against the current density. At low current densities, the performance of ECM and CCM24BA was lower than that of CCM24BC. The low kinetic performance of CCM24BA may be related to its lower active area, however a reason for the low kinetic performance of the ECM compared to CCM24BC could not be identified since the Pt loading and active area of both were similar.

At high current densities representing mass transport region of the polarization plot, ECM shows a better performance than the other electrodes. As compared to CCM24BA, the presence of a micro-porous carbon layer between the CL and GDL in the ECM results in better water management in the CL and consequently better reactant transport. As compared to CCM24BC, the through-plane transport resistance in the case of ECM is lower due to its reduced thickness.
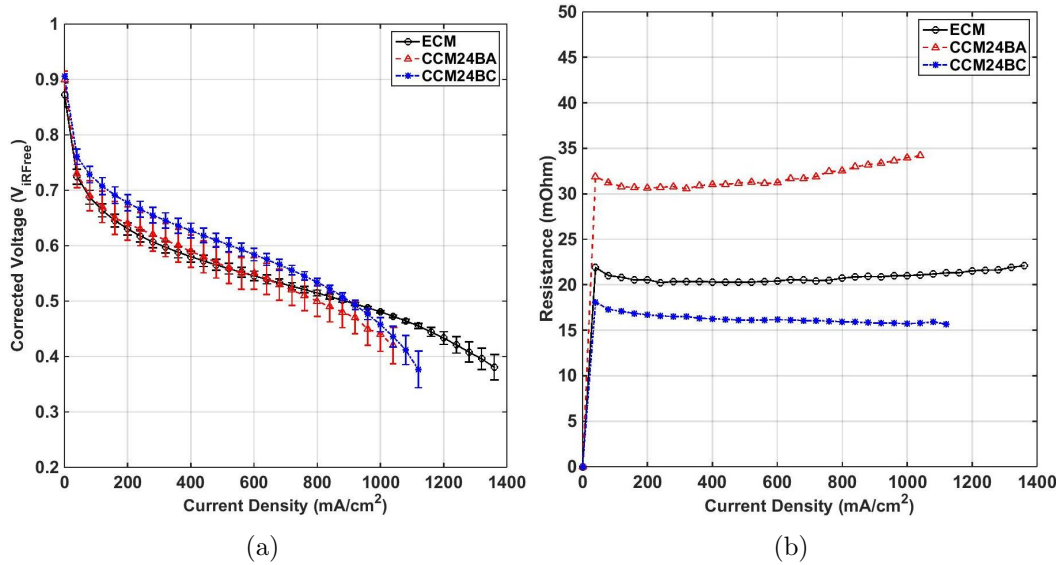
Figure 4.4 – Comparison at 90% RH, 80°C (a) average polarization plots (b) average ohmic resistance obtained from current interrupt

As seen from the Figures 4.4 (b) and 4.5 (b), the resistance for the case of CCM24BA is higher than that of ECM and CCM24BC, whereas CCM24BC shows the lowest resistance of the three. Higher value of resistance for CCM24BA may be related to the type of diffusion media used. The lack of an MPL in CCM24BA may result in lower contact points between the CL and the gas diffusion layer and thus increasing the electrical resistance. For the case of ECM, the contact resistance is lower as compared to CCM24BA but higher than CCM24BC, where the MPL and

91
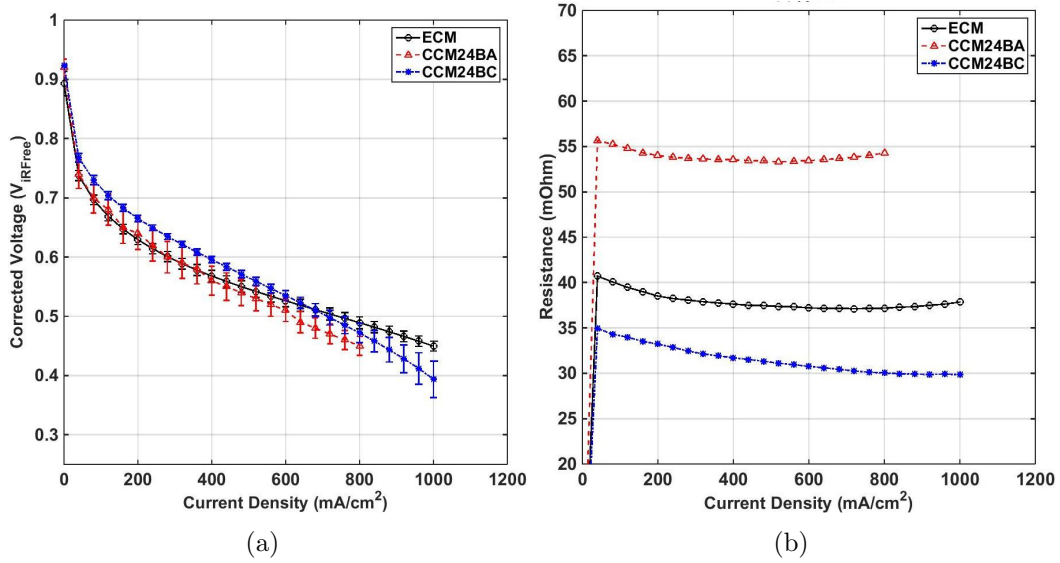
Figure 4.5 – Comparison at 50% RH, 80°C (a) average polarization curves (b) average ohmic resistance obtained from current interrupt

GDL are incorporated in the same diffusion media. Lowering the RH from 90% to 50% caused an increase in the resistance for all the samples which is due to reduced hydration in the membrane.
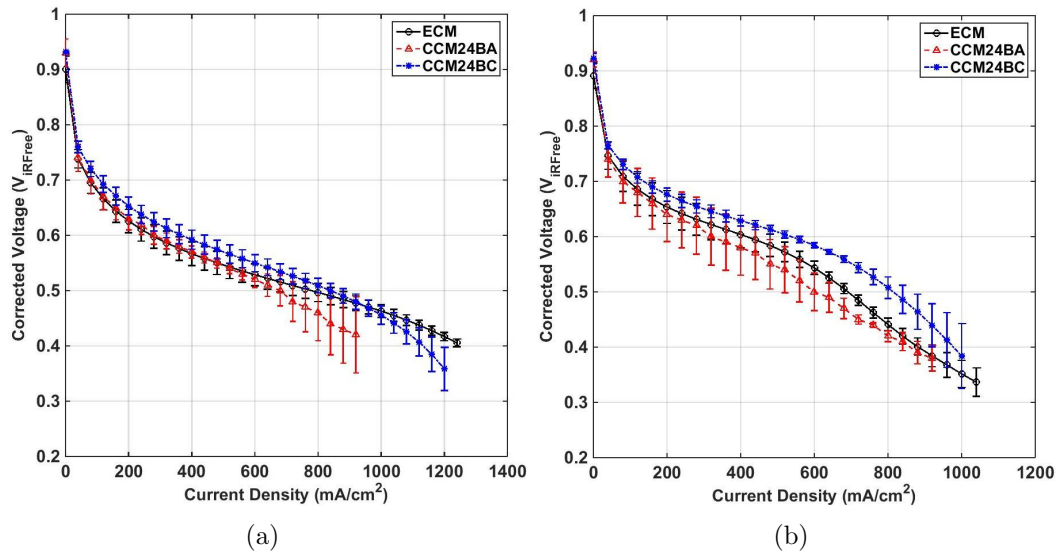
Figure 4.6 – Performance comparison at 60°C (a) 50% RH (b) 90% RH

Figure 4.6 shows the performance comparison at 60°C. At 50% RH, similar trends to that observed in Figure 4.5 (a) are seen. However, at 90% RH, i.e., at very wet

conditions, the performance of ECM in the high current density region is similar to CCM24BC. A reason for this may be related to the type of binder used in the carbon layer. Unlike the PTFE based micro-porous layer used in CCM24BC, the carbon layer in ECM contains Nafion ionomer as the binder. The sulphonic side chains in the Nafion have strong affinity to water molecules and may cause water buildup in the micro-porous layer under very wet conditions. This may cause transport losses as observed in Figure 4.6 (b) for the case of ECM. Ahn et al. [96] studied the effect of Nafion loading in the MPL and found that MPL incorporating 10 wt% Nafion loading showed the best performance. Therefore, reducing the amount of Nafion loading in the carbon layer of the ECM may help to improve its performance especially under very wet conditions.

4.3.3   Oxygen transport resistance

Experiments to measure the limiting current density, i_{lim} were performed using 1% oxygen as the cathodic reactant and parallel flow-field plates at high stoichiometic ratio of 5 at 1 A to minimize pressure losses across the channels. Figure 4.7 shows the plot of limiting currents at 50%, 70% and 90% RH and 80°C. For all the three cases, the current density profile is similar to the one observed in chapter 3 for the electrodes with varying Pt loading. The maximum current above 0.1 V was taken to be the limiting current at the respective operating condition.

The value of i_{lim} increases with increasing RH. From 50% to 90% RH, i_{lim} increased from 116.8±7.9 mA/cm² to 123.2±4.6 mA/cm² for the case of ECM, from 111.6±3.6 mA/cm² to 117.2±7.3 mA/cm² for the case of CCM24BA and from 98.1±2.8 mA/cm² to 103.0±4.3 mA/cm² for the case of CCM24BC. i_{lim} obtained for ECM and CCM24BA are higher than that obtained for CCM24BC. The total transport resistance for oxygen, R_{total}, was evaluated from i_{lim} based on equation (3.4) given in chapter 3. Table 4.3 gives the values of R_{total} calculated for the three cases. The value of R_{total} drops with RH and is lower for ECM and CCM24BA than CCM24BC. A lower value of R_{total} for ECM indicated better mass transport compared to the other two cases. The experimental observations illustrate that lowering the thickness of the carbon micro-porous layer helps to improve the reactant transport.

It is interesting to note that even though CCM24BA showed a higher limiting current under the testing conditions described above, its performance at high current densities when using air as the cathodic reactant was lower than others (Figure 4.4
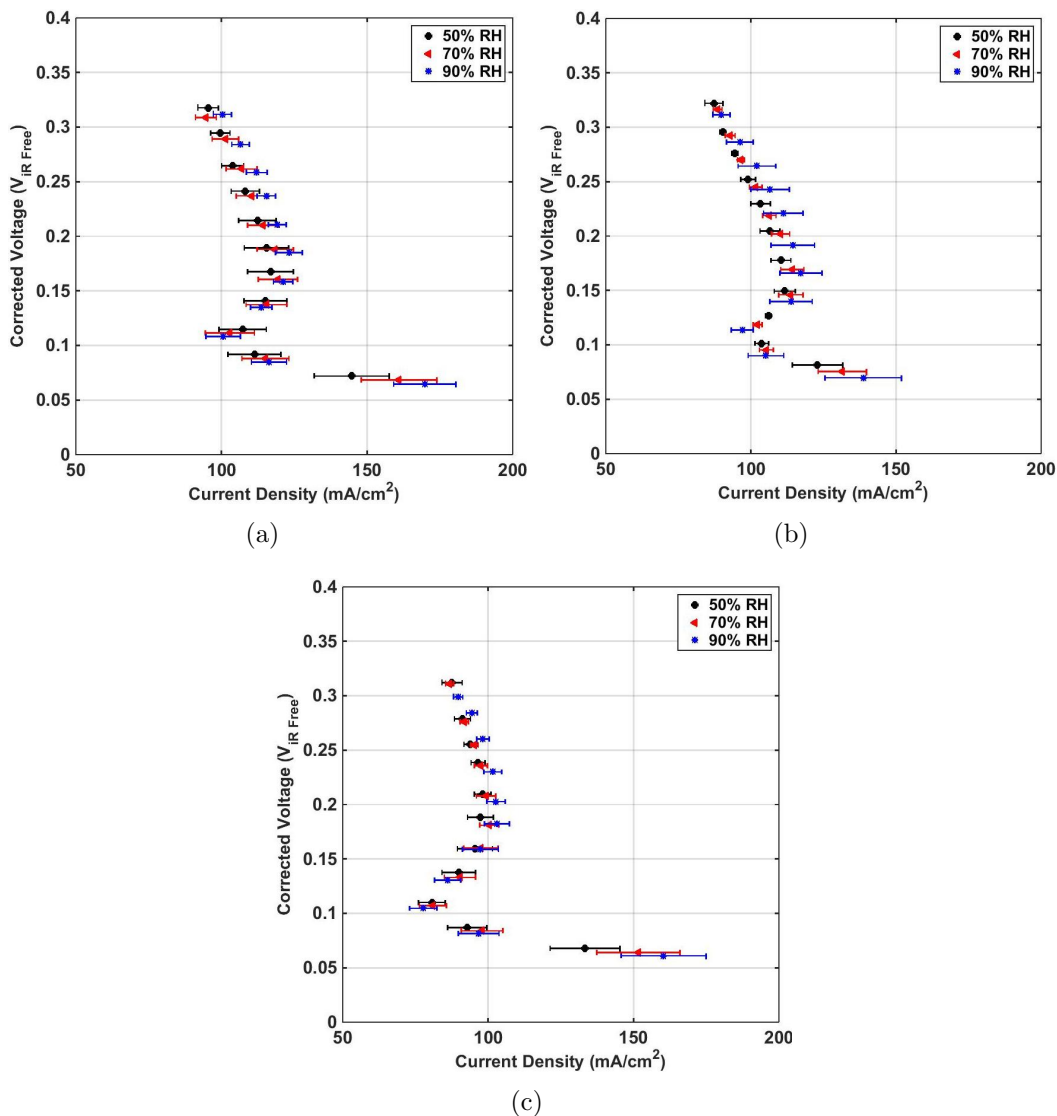
Figure 4.7 – Limiting current density at 50%, 70% and 90% RH, 80°C using 1% oxygen (a) electrode coated membrane (b) CCM24BA (c) CCM24BC

(a)). A reason for this might be because when using air as the reactant, electrodes can produce higher currents at a given voltage than that of 1% oxygen, as thus more water formation in the cathode. The lack of an MPL in CCM24BA may prevent the water from being removed effectively and causes a higher mass transport loss in such case.

Table 4.3 – Comparison of total transport resistance, R_{total} at 50, 70 and 90% RH

Type of electrode	R_{total} at 50%, (s/cm)	R_{total} at 70%, (s/cm)	R_{total} at 90%, (s/cm)
Electrode coated membrane	0.88±0.06	0.77±0.04	0.64±0.02
CCM24BA	0.92±0.03	0.80±0.03	0.68±0.04
CCM24BC	1.04±0.03	0.91±0.03	0.77±0.03

4.4   Conclusions

A novel electrode coated membrane architecture was fabricated using inkjet printing for both cathodic and anodic electrodes. A Nafion based carbon ink was formulated and deposited over the CL using the inkjet printing technique. The microstructure of the fabricated ECM was determined using SEM imaging. Compared to the standard electrode incorporating a commercial diffusion media, performance in the high current density region for the ECM was found to be higher due to the reduced thickness of its carbon micro-porous layer. Only under very wet conditions of 60°C and 90% RH, the ECM caused a drop in the mass transport region.

Limiting current density experiments using 1% oxygen were carried out in order to find the total transport resistance of oxygen at 50%, 70% and 90% RH. The higher limiting current for the ECM compared to CCM24BC translated to a lower transport resistance at all the tested RH conditions. Thus, inkjet printed carbon micro-porous layer fabricated directly over the CL helped to improve the performance in the mass transport region. This technique of MPL fabrication is not limited to IJP catalyst layers but can also be extended to conventionally fabricated CLs to provide better reactant transport at high current densities.

Chapter 5

Fabrication of patterned catalyst layers

This chapter describes the feasibility of using inkjet printing to fabricate patterned catalyst layers. Section 5.1 gives a brief overview of the available literature on patterned electrode structures and the motivation for its study. Section 5.2 discusses the procedure for ink preparation, fabrication and characterization whereas section 5.3 discusses factors affecting the minimum resolution of the printer, optical microscopy and SEM imaging of the patterned electrodes and a preliminary comparison of the electrochemical performance between patterned and non-patterned electrodes.

5.1 Introduction

Chapter 3 described the fabrication and testing of electrodes with increasing Pt loadings. In order to improve electrode performance at low current density, the Pt loading was increased by increasing the number of deposited layers over the membrane surface. This increased the cell performance in the lower current density region but the limiting current dropped due to increased electrode thickness. This can be seen in Figure 5.1 which shows the polarization plot for 10L and 20L CCMs (corresponding to Pt loadings of approx. 0.056 mg/cm^2 and 0.113 mg/cm2 respectively). Here, the kinetic region for the higher Pt loading CCM is greater, however the mass transport region suffers. This drop in the current density for thicker CCMs is mainly believed to be due to the increased macro-scale mass transport losses in the electrodes.

Implementing patterning to improve mass transport and water management is-
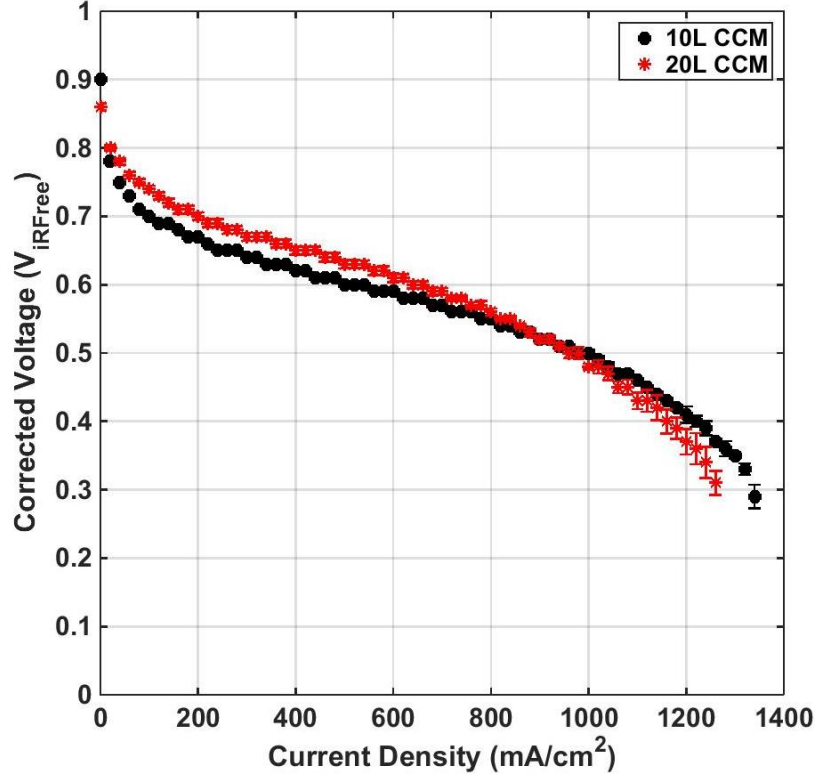
Figure 5.1 – Polarization plots for 10L and 20L inkjet printed CCMs at 90% RH and 80°C. Increased thickness and reduced porosity induces mass transport losses in the 20L CCM at high current densities

sues has been dealt with by membrane and electrode modifications [69, 146–149]. Aizawa and Gyoten [146] used thermal lithography to create micro-pillar structures on the cathodic side of the membrane. Catalyst layers were then deposited on these patterned PEMs and tested. The experimental results and numerical simulations revealed that the patterns helped to reduce proton transport resistance and mass transport losses in the cathode CL. Koh et al. [147] fabricated CLs over a patterned Nafion membrane and reported an increase in the electrochemical active area and the performance of the cells over using a non-patterned membrane. Therdthianwong et al. [148] studied the effect of hydrophobic and hydrophilic parts (using PTFE) in the catalyst layer by using checker board and strip patterns. They found that the catalyst loading patterns were only effective when the electrode thickness was around 50 microns and that patterning did not influence the cell performance when the Pt loading/CL thickness was smaller. Deshmukh et al. [149] used soft lithography to micro-pattern the electrodes on the membrane surface. Although the performance was lower, the patterned electrodes showed reduced sensitivity to temperature and relative humidity variations due to better water management across the electrodes.

Malevich et al. [69] studied the effects of patterned electrodes on the PEMFC performance using inkjet printing. Difficulties in fabricating sharp patterns were identified. The performance of the non-patterned CCM was higher than the patterned CCMs, however this was likely due to its higher Pt loading. It was observed that the patterns strongly influenced the electrode active surface area.

This chapter focuses on the suitability of inkjet printing technology for patterning the fuel cell electrodes. It has been hypothesized that patterned electrodes will help in reducing the mass-transport losses at the macro-scale by having pathways for the reactant gas and water transport across the electrodes. The printer resolution was tested initially by printing various patterns using two printer cartridges having drop volumes of 1 pL and 10 pL corresponding to a nozzle diameter of 9 μm and 21 μm respectively. The maximum resolution was found to be a function of nozzle diameter, substrate used, number of active nozzles during the fabrication process, droplet spacing and number of printed layers. Preliminary performance of the patterned CCMs was compared to that of the non-patterned CCMs using polarization plots.

5.2   Materials and methods

5.2.1   Ink preparation

The catalyst ink was prepared by mixing 20 wt% Pt/C (Alfa Aesar), 5 wt% Nafion ionomer solution (Ion Power), isopropanol and ethylene glycol in the amounts necessary to achieve the desired ionomer loading. The Nafion loading was kept fixed at 30 wt%. The ink was then sonicated using a probe sonicator and a sonication bath which helped in homogenizing the suspension. It was then filled in a printer cartridge and jetted over a Nafion membrane (NR 211, Ion Power). The Dimatix 2831 Fujifilm printer was used for the electrode printing process. Two different cartridges having a nozzle diameter of 9 and 21 μm corresponding to theoretical drop volumes of 1 pL and 10 pL were used for fabrication. The same ink formulation was used for both cartridges.

After one side of the membrane was printed, the CCM was dried in an oven overnight before printing the other side. Once both the electrodes were fabricated and dried, the CCM was boiled in deionized water for 3 hours before storing for further use. The printed CCM had an area of 5 cm^2 and each printed pass from the 10 pL cartridge corresponded to a Pt loading of around 5 μg/cm^2 which was measured using

X-ray fluorescence technique (Niton XL3t, Thermo Scientific). Pt loading was also evaluated using gravimetric analysis using pre-weighed Aluminium foil as a substrate and an average value based on three sample readings was taken. Depending on the desired Pt loading, a number of printed passes were deposited over the membrane with a waiting time of 20 seconds between each printed pass. In order to maintain a similar Pt loading for the patterned CCMs, the passes were increased accordingly in order to compensate for the lack of covered sites over the membrane. To evaluate the cathodic performance, the anodic electrode was kept fixed at a Pt loading of approximately 0.026 mg/cm^2 while the loading on the cathodic electrode was increased to around 0.08 mg/cm^2 and 0.113 mg/cm^2 and the results were compared to non-patterned CCMs. Patterned electrodes containing 46.8% PtC catalyst (Tanaka, Japan) were also fabricated and the results were compared to non-patterned electrodes having a similar Pt loading.

5.2.2 Electrode characterization and testing

The CL microstructure and thickness was determined using a scanning electron microscope (JEOL 6301 F, field emission SEM). The samples were freeze-fractured in liquid nitrogen before mounting them over SEM stubs. The patterns were also analyzed used a digital microscope (USB2, Westover Scientific) and the images were analyzed using the micron imaging software.

CV and chronoamperametry tests were performed for quantification of active area and hydrogen crossover. A potentiostat (VersaStat 4, Princeton Applied Research) was used for the measurements. The anode (hydrogen electrode) was the reference and counter electrode while the cathode was the working electrode during testing. For CV and crossover tests, the cell temperature was kept at 30°C. Both, anode and cathode were fed with fully humidified hydrogen and nitrogen at 0.2 slpm and 0.005 slpm respectively. The CV was performed by scanning the voltage between 70 mV and 800 mV versus the reversible hydrogen electrode at a scan rate of 40 mV/s. The area of the CV plot representing hydrogen desorption, i.e. the region from 0.35 V to 0.1 V; was evaluated as the electrochemical active area. For crossover, chronoamperametry experiments were performed and the crossover current was reported at 0.5 V. The protonic resistance through the electrodes was obtained by implementing electrochemical impedance spectroscopy. 0.1 slpm of dry N_2 was fed through the cathode and 0.1 slpm of hydrogen at 50% RH was fed on the anodic side with a cell temperature maintained at 80°C. Dry gas at the cathode was used to increase the electrode

resistance since at higher humidity, the expected 45° line could not be observed [115]. The impedance spectra was obtained at 0.5 V (DC) by sweeping frequencies in the range of 100 Hz to 25 kHz with an amplitude of 10 mV.

Galvanostatic polarization curves for the cell were obtained using a fuel cell test station (850e, Scribner Associates) with 5 cm² single serpentine channels. The inkjet printed CCMs were sandwiched between two gas diffusion layers containing a microporous layer (SGL SIGRACET 24BC). Once the cell was assembled, it was conditioned with H_2 and compressed air at 0.2/0.4 slpm respectively at 80% humidity and 80°C to humidify the membrane (Conditioning protocol used is given in Appendix A). Performance tests were then recorded at 80°C and humidity values of 50%, 70% and 90% for the cell operating with hydrogen and air at ambient pressure as well as at 1.5 bar back pressure. 1% oxygen (bal. Nitrogen) was also used as the cathodic reactant in order to test at transport limiting conditions. Polarization plots were obtained galvanostatically at a scan rate of 0.1 A/minute. An average curve showing a standard deviation of the three plots for the same sample was obtained.

5.3   Results and discussion

5.3.1   Electrode pattern resolution

In order to assess the resolution of the inkjet printer, the fabrication of lines of various thickness were studied over a Teflon surface using a printer cartridge of 10 pL. Figure 5.2 shows microscopic images of the fabricated lines. Table 5.1 shows the measured thickness of the printed lines. In order to assess the effect of number of working nozzles and the number of passes on the line resolution, four cases were studied. One and five passes were printed with 1 and 16 nozzles and the measured width is given for each case. Lines as thin as 20 μm could be printed wherein the theoretical and actual widths were in reasonable agreement. As the number of passes increased, the lines appeared to be thicker than expected by the printer settings probably due to spreading of the ink drops. The difference between the theoretical and actual line width appeared to increase with increasing number of passes and higher working nozzles. For the case of a theoretical line width of 100 μm, when using 16 nozzles and 1 pass, the measured line width was higher than expected due to uneven spreading of the drops on Teflon. Nafion membrane was also used as a substrate for drop deposition. However, lines appeared more uneven with higher thickness values than those on Teflon. A reason for this may be associated to the difference in surface energies

between Teflon and Nafion as well as the fact that Nafion may absorb some of the solvents in the ink during the deposition resulting in a reduced print resolution. Based on this analysis, it is clear that patterns in the μm size can be fabricated.

(a) (b) (c) (d)
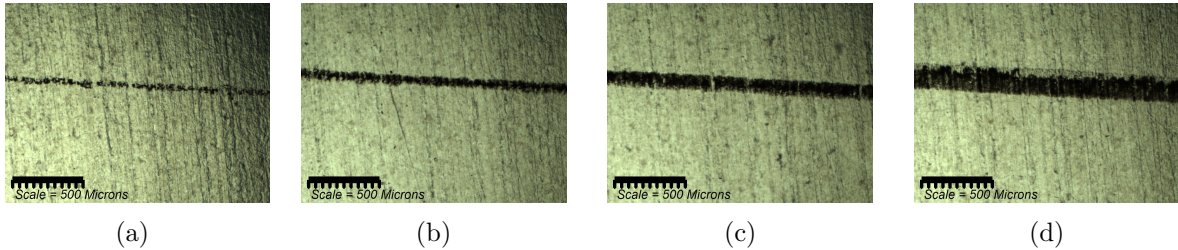
Figure 5.2 – Microscope images of the deposited lines using inkjet printing using 1 working nozzle and 1 pass: (a) 20 μm; (b) 60 μm; (c) 100 μm; (d) 160 μm

Table 5.1 – Thickness of fabricated lines - Comparison between theoretical and measured values for 10 pL cartridge

Working nozzles and passes	Theoretical line width (μm)			
	20	60	100	160
1 nozzle+1 pass	33.5 ±7.5	63.6±5	102.3±8.4	184.5±9.1
1 nozzle+5 passes	47.5±2.6	125.4±17.3	170.1±12.8	191.5±3
16 nozzle+1 pass	32.2±5.1	72.8±6	192.3±4.6	278.3±4
16 nozzle+5 passes	57.3±11.9	105.5±3.3	165.8±55	172±27

Once it was demonstrated that it was possible to deposit micro-scale lines using the inkjet printer, various patterns were analyzed. In order to study the minimum spacing between the patterns, 2 mm × 2 mm square patterns were fabricated with decreasing spacing between them in order to assess the printer resolution in 2D. The printing resolution was a function of nozzle diameter of the cartridge, number of active nozzles during printing and number of printed layers.

Figure 5.3 (a) shows the pre-defined pattern that was used for testing the resolution and Figure 5.3 (b) shows the actual pattern that was obtained after 5 passes. The 100 μm spacing did not appear to be distinguishable in the printed layers. By using a 1 pL cartridge for printing, the minimum distinguishable distance between the patterns decreased. Figure 5.4 shows the pattern that was obtained after 5 passes by using a 1 pL cartridge for printing. Distance between the printed patterns was easily distinguishable to be about 106 microns. However, due to its reduced nozzle size, the cartridge was prone to clogging and needed to be cleaned often while printing.

Further, since the droplets created were smaller in size, more passes were required to achieve a similar Pt loading, which may be time consuming and not commercially viable.

(a)

(b)
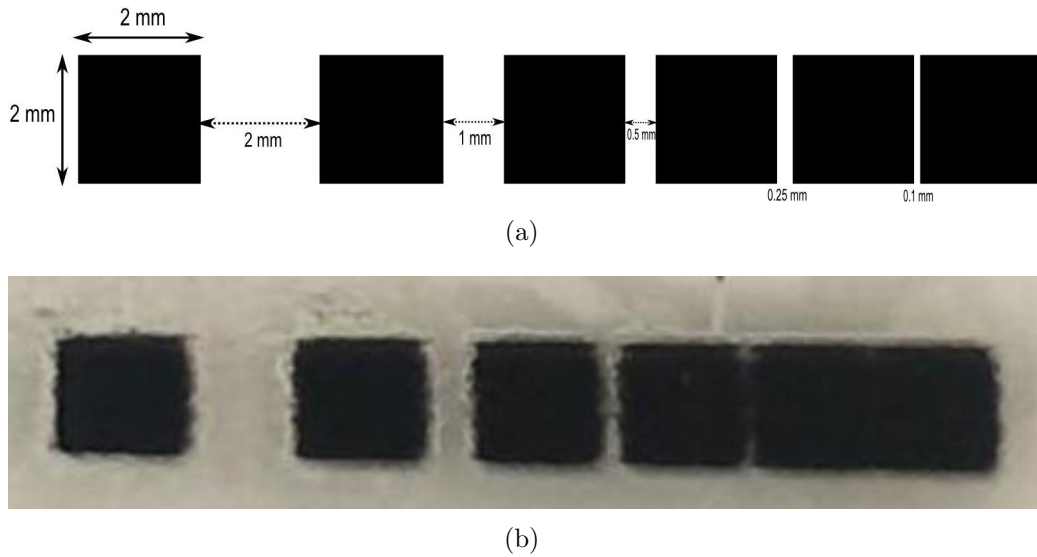
Figure 5.3 – Patterns with varying spacing to see the printer resolution: (a) Predefined pattern; (b) Actual printed pattern (with 1 nozzle and 5 passes)
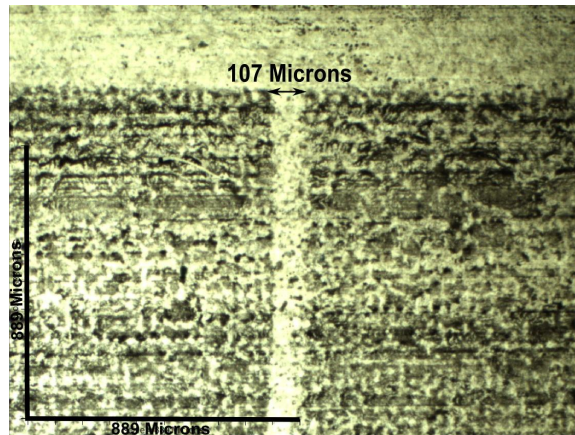
Figure 5.4 – Printed pattern after 5 passes using a 1 pL cartridge having a nozzle diameter of 9 μm. Pattern resolution appeared to increase compared to using a 10 pL cartridge

Table 5.2 shows the resolution of the printed patterns with varying the number of passes and number of working nozzles (1 and 16 working nozzles) for a theoretical separation distance of 500 μm. As the number of printed passes increased, the patterns merged due to spreading of the ink over the substrate. This can be observed from the decrease in spacing distance from 1 pass to 5 passes. Since in order

Table 5.2 – Printer resolution for pre-defined separation distances for the given jetting conditions for 10 pL cartridge over Teflon substrate

# working nozzles	# printed passes	Actual separation distance (for a pre-defined separation of 500 μm	Image
1	1	453±20	
1	5	275±42	
16	1	495±63	
16	5	318±61	
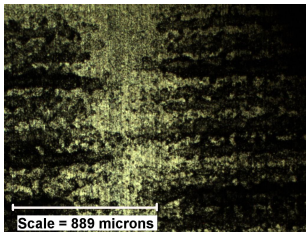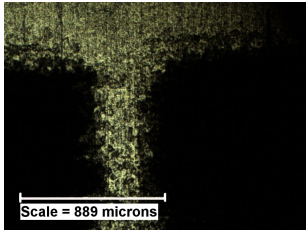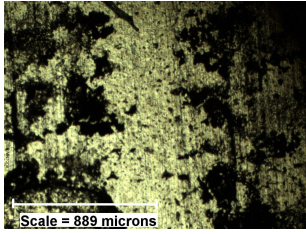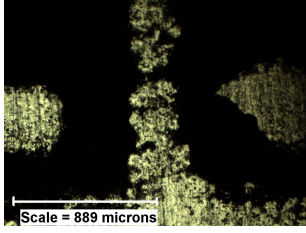
to achieve moderate Pt loadings, the number of passes have to be around 10 to 20, it was concluded that the highest resolution patterns with appropriate loadings was approximately 300 - 350 μm spacing between the features. Higher pattern resolution could be achieved by reducing the number of passes and using a smaller nozzle size for the printer cartridge, but at the cost of printing time.

Increasing the number of working nozzles did not significantly change the pat-

tern spacing as seen from the Table 5.2. Lower number of working nozzles helped in creating a well defined square pattern unlike the pattern created using all the 16 nozzles where the ink did not deposit over the entire pattern. Thus, depositing smaller amounts of ink over a period of time was better than depositing larger amounts in a short period.

Figure 5.5 (a) shows a pattern of 200 μm $\times$ 200 μm squares printed over Teflon surface. The patterns appear to be only slightly larger than the predicted dimension. Figure 5.5 (b) shows the patterns after decalling on a PEM surface. The process involved hot pressing the Teflon over membrane at 120 °C and 10342 kPa for 10 minutes. The patterns appeared to retain their shape well after decal transfer. The obtained results provide an accurate assessment of the maximum pattern resolution available with the inkjet printer and current ink composition.

(a)   (b)
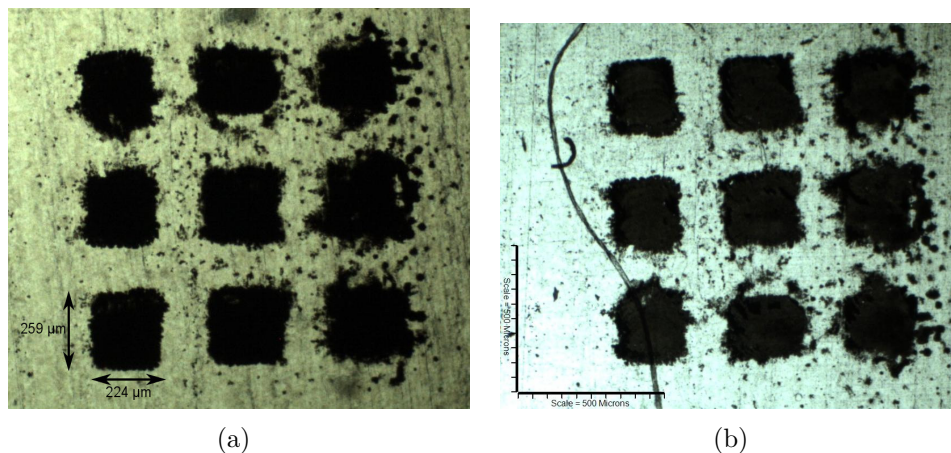
Figure 5.5 – 1 mm^2 patterned block. Each square has a theoretical dimension of 200 μm $\times$ 200 μm: (a) Patterns printed on Teflon. Dimensions of one of the measured square patterns is found to be 259 μm $\times$ 224 μm; (b) Pattern from (a) decal transferred over a PEM

5.3.2   Micro-structure characterization

The non-patterned and patterned CCMs were analyzed using SEM for their microstructure and CL thickness. Figure 5.6 shows the SEM images of the 15 layer non-patterned CCM. It can be seen from Figure 5.6 (a) that no micro-cracks are observed over the CL surface. Figure 5.6 (b) shows the CL microstructure where the individual catalyst particles can be seen to be around 60 -80 nm in diameter.

Cross-sectional image of the CL is shown in Figure 5.6 (c). The thickness appears to be uniform with a value of 4.9 ±0.38 μm.

(a)

(b)

(c)
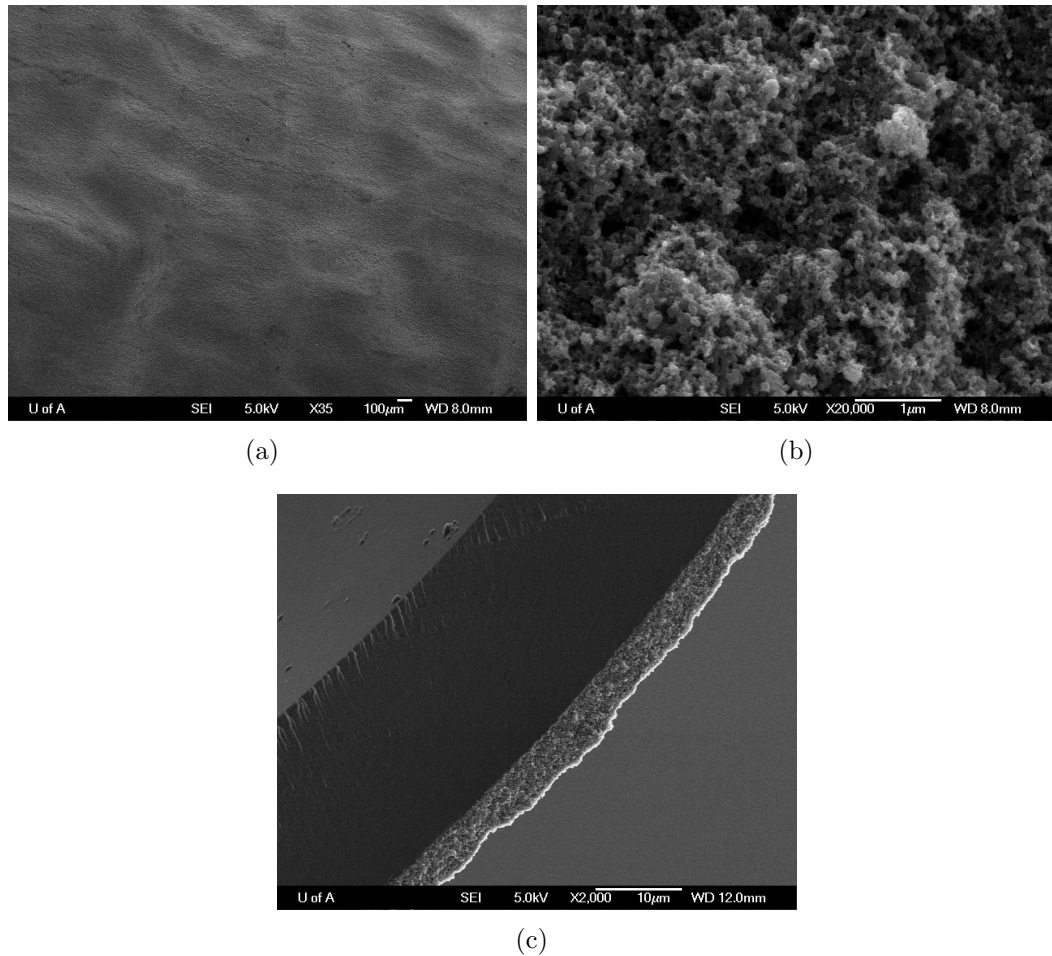
Figure 5.6 – SEM image of the inkjet printed non-patterned CCM: (a) Surface image; (b) Microstructure of the printed layer; (c) Cross-sectional image. CL thickness is around 5 μm

Figure 5.7 shows the SEM images of top view of patterned CCMs with micropores of 500 μm in length. Figure 5.7 (a) shows the image of 12 patterned layers printed over a membrane, Figure 5.7 (b) shows the image of 12 patterned layers over 5 non-patterned layers. The patterns appear to be more distinct when they were printed over a membrane, however a high hydrogen crossover was associated with these CCMs while testing probably due to more exposed membrane surface. The patterns lost their resolution when printed over a non-patterned catalyst layer. Figure 5.7 (c) shows the freeze-fractured side image of the patterned CCM. Unlike the non-patterned CL, a variation in the CL thickness can be observed which is a result of the patterns.
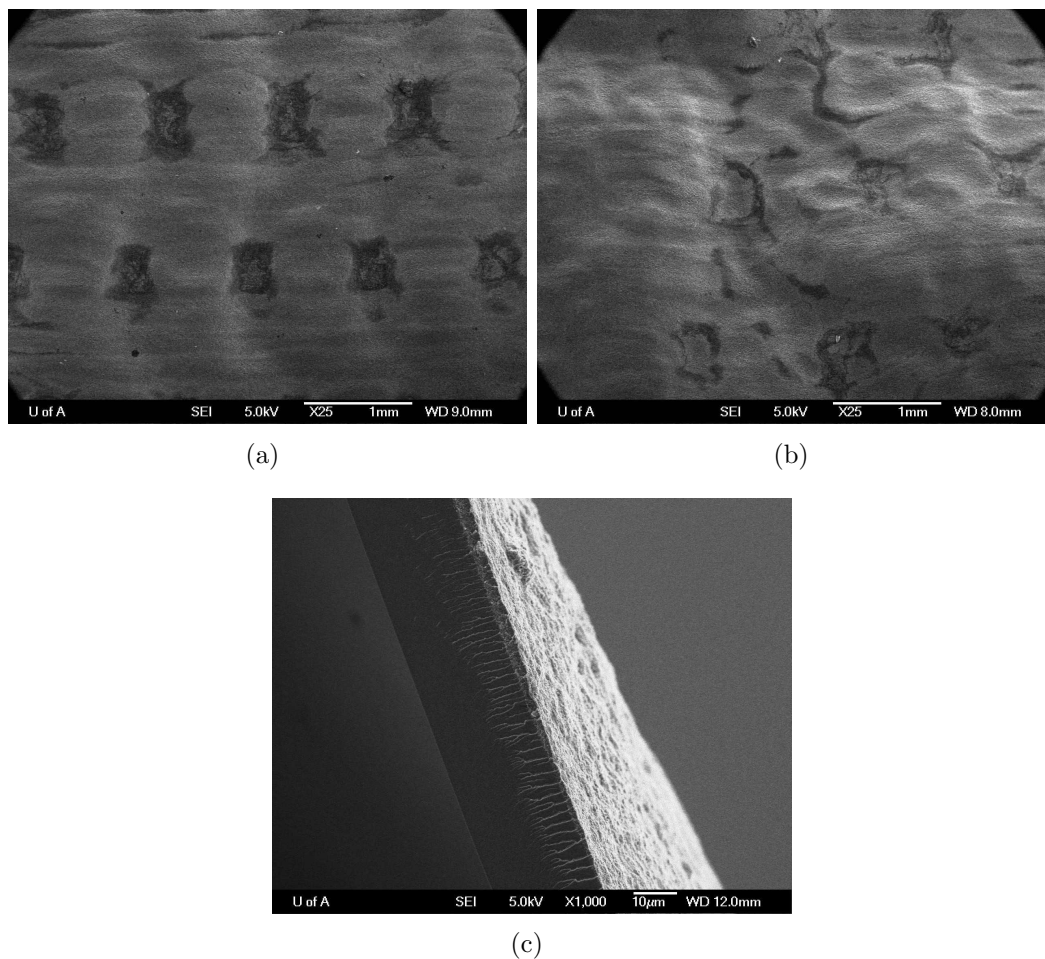
Figure 5.7 – SEM image of the inkjet printed patterned CCMs: (a) Surface image showing 12 passes of patterns printed directly over a membrane; (b) Surface image showing 12 passes of patterns printed over 5 passes of non-patterned CL; (c) Freeze-fractured side image of the patterned CCM showing variation in thickness due to the patterns

5.3.3 Electrochemical characterization

Patterning could be used in order to fabricate electrodes with macro-porosity. Therefore in addition to studying pattern resolution, uniform layers with equally spaced macro-pores were fabricated as shown in Figure 5.8 (a). These macro-pores are expected to improve gas transport in the electrodes and act as water reservoirs if the CL is hydrophobic. Figure 5.8 (b) shows a patterned electrode only in the channel region of the cell. This may help in improving the Pt utilization from the assumption that the diffusion flux of reactant gases in the channel region is higher than in the land region.

In order to reduce the H_2 crossover, non-patterned 5 layers were initially deposited over the membrane and the patterned layers were then fabricated over it. 12 and 18 patterned layers were deposited over the 5 non-patterned layers corresponding to a Pt loading of approx. 0.08 and 0.113 mg/cm² respectively when using 20 wt% PtC catalyst . Non-patterned CCMs were fabricated with similar Pt loadings and the results were compared.

<center>(a)   (b)</center>
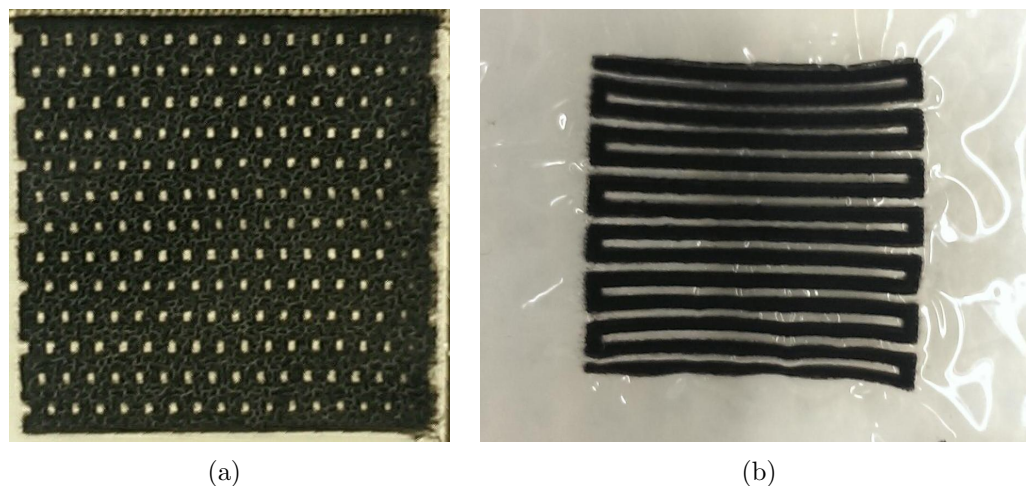
Figure 5.8 – Patterned electrodes fabricated using inkjet printing: (a) Electrode with micro-pores; (b) Electrode following the gas flow channels

Hydrogen crossover current for both the CCMs was below 1 mA/cm². When using 20% Pt/C catalyst, the active areas for CCMs with Pt loading of 0.08 mg/cm² were 47 m²/g and 52 m²/g while for Pt loading of 0.113 mg/cm², the active areas were 38 m²/g and 41 m²/g for the patterned and non-patterned CCMs respectively.

Figure 5.9 shows the Nyquist plot for the patterned and non-patterned CCMs with a Pt loading of 0.113 mg/cm². Analyzing the preliminary data resulted in a CL protonic resistance of around 165 mΩ.cm² for the patterned electrode and 210 mΩ.cm² for the non-patterned electrode (details regarding the analysis can be found in Chapter 2). Ohmic resistance (X-intercept) also appeared to be lower in the case of patterned CCM. Thus, patterning helped in reducing the proton transport losses across the electrode. Similar observations have been reported in literature for the case of patterned membranes [146, 147].

Figure 5.10 shows the performance comparison of the two for a Pt loading of 0.08 mg/cm² at 80 C and 50% and 90% RH. The voltage used was iR corrected in order
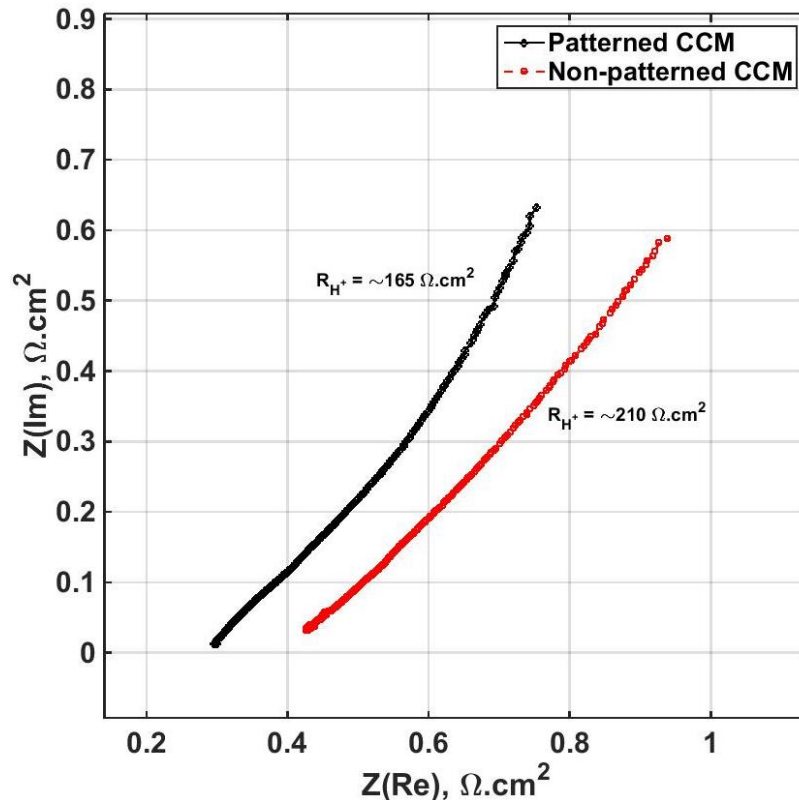
Figure 5.9 – Nyquist plot for inkjet printed CCMs with a Pt loading of 0.113 mg/cm^2 using potentiostatic EIS at a cell potential of 0.5 V at 80°C using H$_2$ /N$_2$ from 100 Hz to 25 kHz with anodic and cathodic RH of 50% and 0% respectively

to neglect ohmic losses between the samples and focus on mass transport variations. The patterned CCM used for testing was similar to the one shown in Figure 5.8 (a). Preliminary results show minimal difference in performance between the two CCMs under the given operating conditions with 1% oxygen, air and air at 150 kPaG back pressure. This suggests that the pattern resolution is too small for any noticeable change in performance.

Figure 5.11 (a) shows the performance comparison between the patterned and non-patterned CCMs when using 20% Pt/C catalyst having a Pt loading of 0.113 mg/cm^2 and whereas Figure 5.11 (b) shows a similar comparison but using 46% Pt/C catalyst at two Pt loading cases at 90% RH. The performance of the patterned and non-patterned CCMs is comparable here as well. The reason for this similar performance might be related to the reduced thickness of these printed electrodes where the macro-scale effects are insignificant even for the case of non-patterned CCM. Therdthianwong et al. [148] saw the effect of patterning only at 50 micron
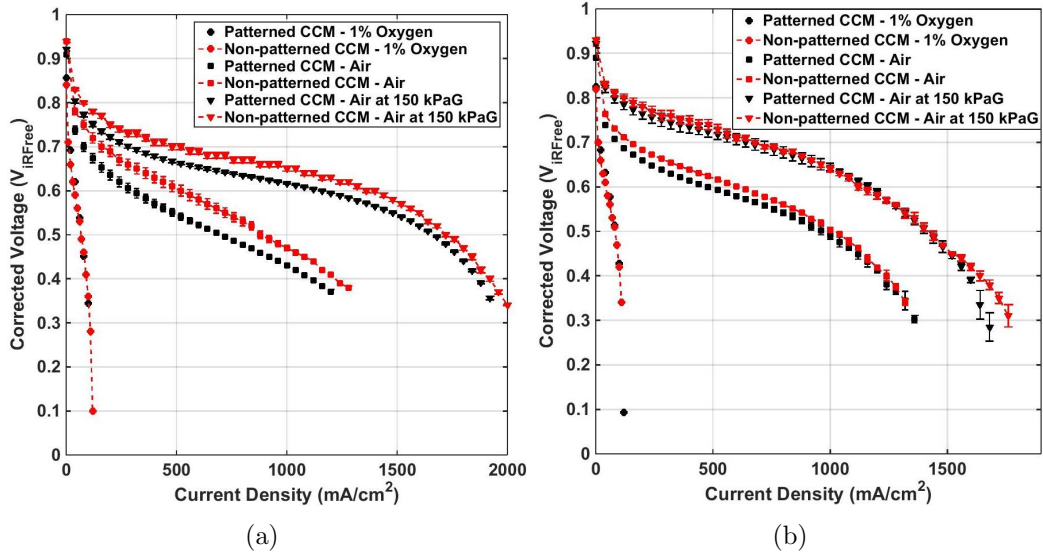
Figure 5.10 – Fuel cell performance of patterned and non-patterned electrodes with Pt loading of 0.08 mg/cm^2 (20% Pt/C catalyst) at 80°C using 1% oxygen, air and air at 150 kPaG as the cathodic reactants (a) 50% RH (b) 90% RH
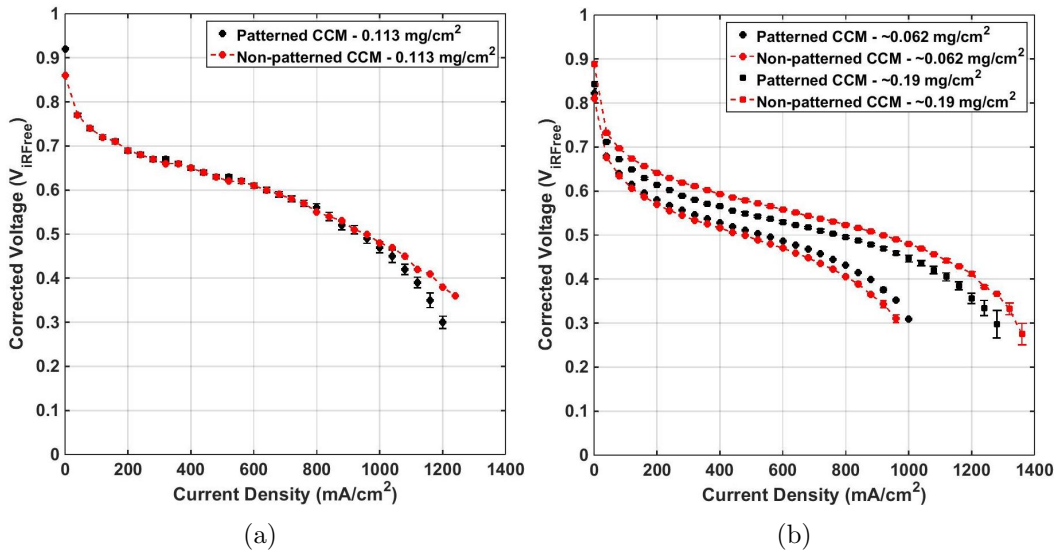
Figure 5.11 – Fuel cell performance of patterned and non-patterned electrodes at 90% RH and 80°C using H$_2$/air (a) using 20% Pt/C catalyst with Pt loading of 0.113 mg/cm^2 (b) using 46 wt% Pt/C catalyst at two Pt loading cases of approx. 0.062 mg/cm^2 and 0.19 mg/cm^2

electrode thickness. Thus, patterning may be beneficial for the case of higher Pt loading CCMs where the macro-scale losses are more prominent. Further analysis with multiple samples for each case is needed to be more certain about the findings since only one sample per case was tested.

5.4   Conclusions

The capability of producing patterned fuel cell electrodes was demonstrated in this study. The minimum resolution and feature size depended upon the type of cartridge and number of printed passes. Sharp images could be generated by lowering the number of working nozzles while printing. Macro-patterns retained their dimensions after decal transfer over a membrane from Teflon substrate. Initial results does not show any performance dependence on patterning of the electrodes which may be due to the lower electrode thickness and smaller pattern resolution.

Chapter 6

Effect of dispersion media on ink stability

This chapter provides an attempts to rationalize the effect of dispersion media on the stability of carbon black based on colloidal interactions. A model implementing van der Waals and Coulombic interaction energies is used to calculate the interaction energies and subsequently the decay in the number concentration of particles with time based on the stability ratios. Experimental validation using four non-aqueous dispersion media - methanol, ethanol, isopropanol and ethyl acetate is carried out. Section 6.1 talks about details regarding ink preparation and characterization methods used while section 6.2 discusses the theory used for evaluating the interaction energies, aggregation kinetics and the assumptions and constants used. Section 6.3 discusses the results obtained from the experiments for the stability time, a theoretical quantification for each case and the effect of Nafion for the IPA based ink.

6.1 Materials and methods

6.1.1 Sample preparation

Experiments were carried out using non-aqueous dispersion media (DM), i.e., ethyl acetate (EA) (HPLC grade, Fisher Scientific), isopropanol (IPA) (HPLC grade, Fisher Scientific), methanol (HPLC grade, Fisher Scientific) and ethanol (Commercial Alcohols Inc.). They were chosen because of the difference in their dielectric constants, a property which dictates particle interaction, available literature data for zeta potential of carbon black in these media and their common use as solvents in catalyst

inks [27, 74, 150]. Commercially available carbon black, Vulcan XC-72R (Fuel Cell Store) was used as received. The inks were prepared in glass vials by mixing 12.5 mg of carbon black with 3.5 ml of the DM. When considering the effect of ionomer, Nafion solution (5% wt, Ion Power Inc.) was added to the ink. The volume of DM was adjusted in order to maintain the solid fraction constant. The amount of ionomer to be added to the ink was calculated using equation (2.1) described in chapter 2 and was kept at 30 wt% unless specified.

The mixture was first stirred using a sonication bath (Branson 1800) for 45 minutes. It was further mixed with a probe sonicator (QSonica S-4000) for 15 minutes (2 min. ON and 1 min. OFF) to break up the aggregates and homogenize the suspension. The addition of Nafion was carried out drop-wise while the ink was being sonicated. The samples were finally stirred using a magnetic stirrer for 10 minutes before leaving them undisturbed for further analysis.

6.1.2 Particle size analysis

Dynamic light scattering (DLS) was employed to determine the particle size in the ink (ALV/CGS-3 GmBH Compact Goniometer System). Sample preparation involved dilution of the ink to less than 1% of its original weight. The dilution is essential to acquire good scattering data. Prior to testing, the sample was allowed to equilibrate to 25°C for 5 minutes. The scattering angle was kept at 90°. The input parameters, viscosity and refractive index of the dispersion media used for IPA were 1.96 cP/1.374, for EA were 0.42 cP/1.372, for methanol were 0.55 cP/1.326 and for ethanol were 1.09/1.361 respectively. The refractive index of carbon black was taken as 2.41 [151]. For each sample, three runs were conducted with a run time of 60 seconds each and a gap of 2 minutes between each run. The average value of particle radius with the standard deviation is reported.

It should be noted that DLS results are highly sensitive to the presence of larger aggregates in the sample that may lead to an overestimation of particle size when plotting the intensity size distribution [152]. Also, the particle size obtained from DLS is the hydrodynamic diameter for the particles. This value may be greater if the particle surface consists of attached polymer chains. These drawbacks, combined with the necessity to dilute the ink means that DLS results can only be used for a qualitative assessment of particle size.

6.1.3   Mercury intrusion porosimetry

The density of Vulcan XC-72 carbon black was evaluated by using a mercury intrusion porosimeter (Poremaster 33, Quantachrome Instruments). Details regarding the experimental procedure have been described in Chapter 2. The averaged density value of carbon black was found to be 1.69 ± 0.21 g/cm^3 based on 4 independent tests. This value of density was used in the model.

6.2   Theory

A catalyst ink can be considered as a colloidal dispersion of particles in a liquid medium. When introduced in a DM, these nanoparticles will tend to collide with each other due to their random Brownian motion. If the collision energies are large enough to overcome the repulsive energy barrier, they will lead to the formation of aggregates [153]. These aggregates will increase in size and at a point when the aggregate size can no longer remain in a state of colloidal dispersion, sedimentation will take place resulting in a non-dispersed ink. In order to prevent this phase-separation and keep the aggregate size as small as possible, a suitable DM needs to be selected and the interacting energies acting on the nanoparticles need to be studied. This section describes the evaluation of parameters used to estimate the effect of DM on ink stability.

6.2.1   Evaluation of interaction energy

Figure 6.1 shows the interacting energies between two colloidal particles of radius a separated by a distance h suspended in a dispersion medium. Distance between the center of the two particles is represented by r. Main interaction energies acting on the particles include attractive van der Waals (vdW) (arising from dipole-dipole interactions), repulsive Coulombic/electrostatic energies (arising from surface charges and electric double layer), steric interactions (caused by an attached polymer chain) as well as other forces such as hydrophobic interaction and drag.

For the case of aqueous dispersion, the particle surface potential (ζ) will attract counter-ions from the DM around the particle as shown in the Figure 6.1 to form an electric double layer. These electric double layers provide electrostatic repulsion when they interact as the particles approach. For the case of non-aqueous dispersion when counter-ion concentration is very low or absent, Coulombic interaction replaces the electrostatic double layer interaction between the particles [154]. The attractive
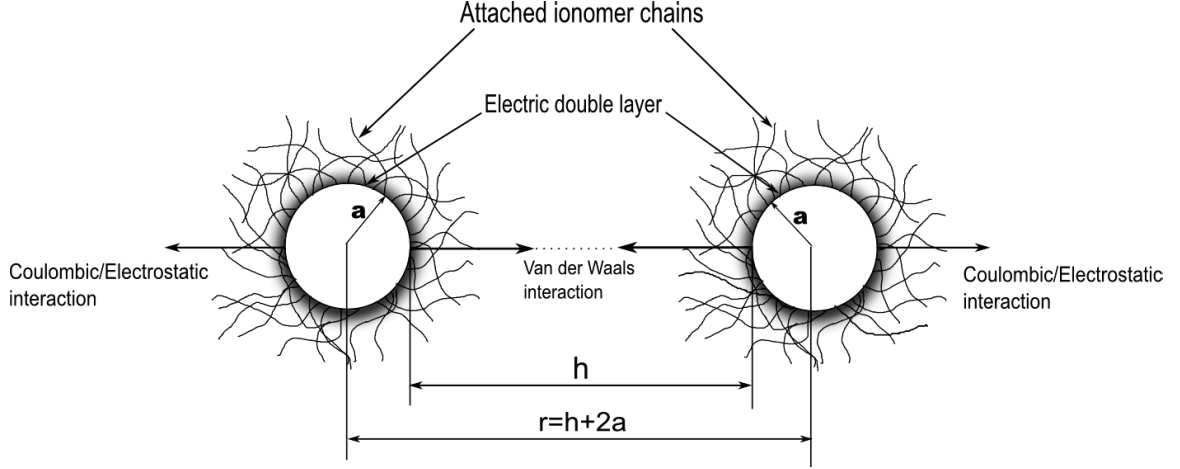
Figure 6.1 – Interactions between the colloidal particles when suspended in a liquid medium showing the van der Waals, electrostatic and Coulombic interactions

energy between the particles is in the form of van der Waals interaction. These interaction energies are discussed in more detail below.

Electrostatic energy should be carefully evaluated when dealing with hydrophobic colloidal particles such as carbon black since the properties of water change substantially near a hydrophobic surface [155]. The density, viscosity and dielectric permittivity of water decreases near a hydrophobic surface due to variation in hydrogen bonding and molecular mobility [155]. Thus, conventional DLVO type interaction may tend to over-predict the dispersion stability for such cases. Since this work is based on non-aqueous systems, such a detailed analysis was not performed.

When $a >> h$ (*Derjaguin* approximation), the van der Waals expression for two interacting spherical particles of radius a_i and a_j takes the form [156]

$$U_{vdW} = -\frac{A}{6} \cdot \left(\frac{a_i a_j}{a_i + a_j} \right) \cdot \frac{1}{r - (a_i + a_j)} \tag{6.1}$$

where U_{vdW} is the interacting energy, A is the Hamaker constant and the negative sign indicates attractive interaction. For two equal sized spheres of radius a, the equation simplifies to,

$$U_{vdW} = -\frac{aA}{12(r - 2a)} \tag{6.2}$$

The Hamaker constant (A) is a function of the particle and medium dielectric and optical properties and is approximated as [157],

$$A = \frac{3}{4} k_B T \left(\frac{\epsilon_p - \epsilon_m}{\epsilon_p + \epsilon_m} \right)^2 + \frac{3 h \nu_e}{16\sqrt{2}} \frac{(n_p^2 - n_m^2)^2}{(n_p^2 + n_m^2)^{3/2}} \tag{6.3}$$

where ϵ_p is the particle dielectric constant and ϵ_m is the medium dielectric constant. n_p and n_m are the respective refractive indices for particle and medium. The constant used for absorption frequency ν_e is taken as $5 \times 10^{15} s^{-1}$ [157].

The repulsive Coulombic interaction (U_{cf}) takes the form [158]

$$U_{cf} = \frac{4\pi\epsilon_m^* \psi^2 (a_i + a_j)^2}{r} = \left. \frac{4\pi\epsilon_m^* \psi^2 a^2}{r} \right|_{a_i = a_j} \tag{6.4}$$

where ψ is the particle surface charge and ϵ_m^* is the absolute permittivity of the medium. The overall energy balance for the two particles is written as the sum of the van der Waals and Coulombic energies. Thus, the total interaction energy (U_{tot}) becomes,

$$U_{tot}(r) = U_{vdw} + U_{cf} \tag{6.5}$$

Equation (6.5) is a modification of the commonly known DLVO type particle interaction.

6.2.2 Aggregation kinetics

During the aggregation process, two primary particles (monomers) collide and aggregate to form a dimer, while a monomer and a dimer collide to form a trimer which is an aggregate of three primary particles. Considering diffusion limited (perikinetic) aggregation, the population balance equation gives the rate of change of particle number concentration, i.e., number of particles per unit volume of ink with time [153]. Considering that particles i and j collide to form particle k, the concentration of particle k can be written as [153]

$$\frac{dn_k}{dt} = \frac{K_{ij}}{2} \sum_{i=1;j=k-i}^{i=k-1} n_i n_j - K_{ik} n_k \sum_{i=1}^{\infty} n_i \tag{6.6}$$

where n_i, n_j and n_k represent concentration of i, j and k particle aggregates respectively and K_{ij} is the rate constant of aggregation. For two colliding particles of radius a_i and a_j, the collision rate constant, K_{ij} is given as [153]

$$K_{ij} = \frac{2k_B T}{3\mu} \frac{(a_i + a_j)^2}{a_i a_j} \tag{6.7}$$

where $k_B T$ is the thermal energy associated with the particles and μ is the DM viscosity. If equal particle radii are considered ($a_i = a_j$) which is a reasonable assumption only during early stages of aggregation [153], the value of K becomes independent of the particle size,

$$K = \frac{8k_BT}{3\mu} \tag{6.8}$$

and the population balance equation can be written as [153, 156]

$$\frac{dn_t}{dt} = -\frac{K}{2}n_t^2 \tag{6.9}$$

where n_t is the total particle number-concentration.

Equations (6.6) and (6.9) allow the possibility to plot the rate of decay of particle number-concentration with time, for a given particle size. These equations however assume a collision efficiency of unity i.e., all collisions lead to aggregate formation. However, the collision efficiency (α) will depend upon the particle interactions and change with the type of DM. A DM in which repulsive energy between the colloidal particles is greater than the attractive energy will have a lower collision efficiency since not all collisions will lead to the formation of aggregates [153].

Thus, including the collision efficiency, equations (6.6) and (6.9) become,

$$\frac{dn_k}{dt} = \alpha \left(\frac{K_{ij}}{2} \sum_{i=1;j=k-i}^{i=k-1} n_i n_j - K_{ik} n_k \sum_{i=1}^{\infty} n_i \right) \tag{6.10}$$

and

$$\frac{dn_t}{dt} = -\alpha \frac{K}{2}n_t^2 \tag{6.11}$$

The collision efficiency, α is the inverse of the stability ratio, W. W is defined as the ratio of collision rate in absence of any external forces, i.e., solely due to Brownian motion, to the collision rate considering inter-particle interactions. For equal sized particles of radius a, it is given as [159]

$$W = \frac{1}{\alpha} = 2a \int_{(2a+a_t)}^{\infty} \frac{1}{r^2} exp \left(\frac{U(r)}{k_BT} \right) dr \tag{6.12}$$

where $U(r)$ is the total inter-particle interaction given by equation (6.5). The value of W was calculated by numerically integrating the expression in MATLAB. A minimum cut-off distance of 0.5 nm (a_t) was added while evaluating W in order to prevent the inter-particle distance from reaching zero.

6.2.3 Sedimentation-diffusion equilibrium

Given the particle diameter, it is possible to plot the particle number-density, n with respect to the height, z of the colloidal suspension by using the sedimentation-diffusion equilibrium equation [100]. This relation makes use of the particle terminal

velocity and Stefan velocity, which is the diffusive flux expressed in the form of a linear velocity. At equilibrium,

$$-D\frac{dln\,n}{dz} = \frac{4a^2(\rho_p - \rho)g}{18\mu} \tag{6.13}$$

where the right hand side of the equation is the terminal velocity and left hand side is the Stefan velocity. Here, ρ_p and ρ are the particle and medium densities, μ is the DM viscosity and g is the acceleration due to gravity taken as 9.81 m/s^2. Solving for the condition that at z=0, $n = n_0$, the initial particle concentration, we get

$$n(z) = n_0 exp\left[\frac{-\pi 8a^3(\rho_p - \rho)g}{6kT}z\right] \tag{6.14}$$

Using this relation, a plot of particle number-density profile with height has been obtained.

6.2.4   Assumptions and constants

The following assumptions and constants were used.

- Carbon particles are assumed to be perfectly spherical suspended in infinitely dilute concentrations in the DM at room temperature. The primary particle size is assumed to be 25 nm in diameter [160].

- Particle collisions are purely diffusion limited, i.e., perikinetic aggregation.

- Screening effects are absent in non-aqueous DM and the repulsive force is provided by Coulombic interactions.

- The zeta potential, ζ is assumed to be equal to the particle surface charge, ψ.

Constants used for the DM and particles are given in Table 6.1. The values of zeta potential for carbon black in IPA, methanol and ethanol were obtained from literature [150]. A value of ζ for carbon black in ethyl acetate was not found. Hence, a potential of -50 mV was considered here. Performing a sensitivity analysis, it was found that the ink stability was not a strong function of zeta potential for the case of ethyl acetate. Hence an approximate value of potential can be valid here. This has been discussed further in section 6.3.

Table 6.1 – Constants used and calculated Hamaker constants for the dispersion media

Dispersion Media	Dielectric constant, ϵ	Zeta Potential of CB in media, ζ (mV)	Refractive Index, n	Hamaker constant, A (J)
Ethyl Acetate	6.0	-50.0	1.37	3.19×10^{-19}
Isopropanol	18.0	-71.1 [150]	1.37	3.20×10^{-19}
Methanol	33.0	-28.5[150]	1.33	3.46×10^{-19}
Ethanol	25.3	-44.9[150]	1.36	3.26×10^{-19}

6.3 Results and discussion

6.3.1 Dispersion stability

6.3.1.1 Experimental observation

As time progresses, the collision between the carbon particles in the ink will lead to formation of larger aggregates. The larger aggregate size will lead to a lower particle concentration at the top compared to the bottom of the colloidal system into consideration. This will lead to a phase separation of DM and carbon particles in the ink. The time required for the colloidal particles to separate from each of the studied DM was noted based on visual inspection. Figure 6.2 shows the effect of DM on carbon stability for the four cases. Based on visual inspection, ethyl acetate and methanol based inks became unstable in under 2 minutes after their preparation, whereas IPA based ink was observed to be stable for more than 30 days. The stability time for ethanol based ink was found to be around 8-12 days. Based on these experimental observations for the four DM, IPA was found to be a better dispersion medium for carbon black.
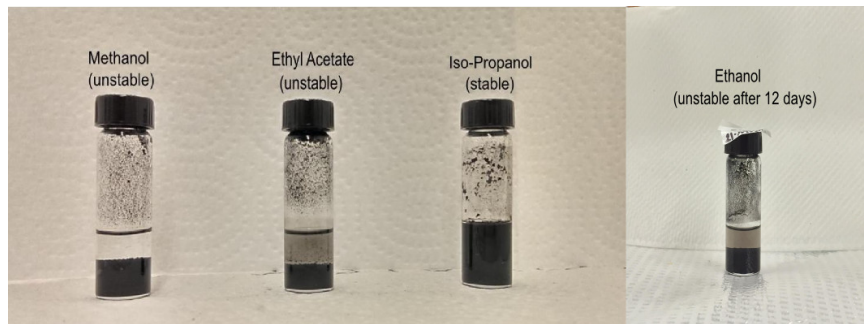
Figure 6.2 – Effect of DM on carbon ink stability

6.3.1.2 Model prediction

In order to analyze these observations, equation (6.5) was used to determine the interaction energy between the particles, which was then used to determine the values of W and rates of particle aggregation. Table 6.2 gives the calculated values of the stability ratio for particle radii from 12.5 nm to 60 nm for the four DM. It can be seen that for all the DM, W increases with particle size indicating that rate of aggregation decreases as the aggregate size increases. W was found to be a strong function of particle size for IPA followed by ethanol, methanol and finally ethyl acetate. Lower values of W for ethyl acetate and methanol indicate unstable dispersion as observed experimentally. The calculated values of W for IPA and ethanol beyond 45 nm are in agreement with the definition of a stable dispersion, i.e., $W > 10^5$ [154]. The stability ratio may therefore be a good qualitative indicator for determining whether a dispersion is stable or not.

Table 6.2 – Effect of particle size on Stability Ratio (W) for carbon black in ethyl acetate,methanol, ethanol and IPA

Particle radius (nm)	Ethyl Acetate	Methanol	Ethanol	Isopropanol
12.5	0.32	0.45	1.56	27.27
15	0.35	0.56	2.9	131.9
30	0.73	3.07	428	1.19×10^7
45	1.92	33.19	2.3×10^5	5.87×10^{12}
60	6.31	583.56	2.41×10^8	6.78×10^{18}

Quantification of time for which the inks remain dispersed required calculating the time needed for the carbon particles to reach a threshold size beyond which they will settle towards the bottom of the glass vial. The threshold particle size was calculated based on the number-density profile using equation (6.14). Figure 6.3 shows the particle distribution profile for different particle sizes from 50 nm to 800 nm in IPA. The height, z plotted on the Y-axis matched the height of the ink in the vial used for the experimental study. The X-axis shows fraction of the particle-concentration as a function of height, z. It can be seen from Figure 6.3 that for smaller particle sizes of 50 and 100 nm, little or no variation in the density profile is observed for the entire colloidal system height. As the aggregate size increases further, concentration towards the top starts to drop indicating that diffusion is lagging behind sedimentation to maintain particle distribution throughout the medium. For an aggregate size of 400 nm, the particle concentration at the top is less than 20% of the total particle concentration. At 800 nm, the top 1.5 cm appears to be void of any particles and

their concentration appears only below 1 cm from the bottom.
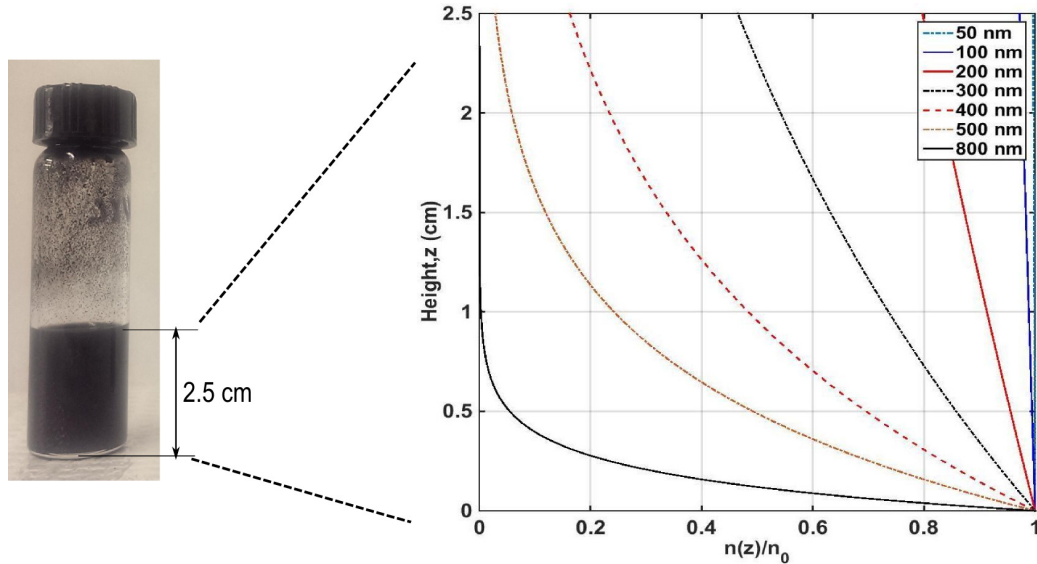
Figure 6.3 – Number density profiles of various particle sizes with the height, z in IPA. Smaller particles are well dispersed while sedimentation is more prominent in larger particles

The threshold particle size beyond which the ink is considered as unstable based on visual inspection is subjective. It will depend on how uniform we want the particle distribution in the ink to be and the height of the colloidal system into consideration. For this case, the threshold particle size is considered to be 300 nm where the particle number concentration at the top of the vial is less than 50% of the total number of particles in the system.

Based on the calculated values of W, equations (6.10) and (6.11) were used to plot a decay rate of the primary particles (normalized) with time considering poly-dispersed and monodispersed particle sizes respectively. Figure 6.4 shows the rate of change of primary particle concentration (n_1) to aggregates of 15 primary particles (n_{15}) normalized with the original particle concentration (n_0), considering the case of polydispersed particle sizes. Particle aggregates $> n_{15}$ will also be formed but have not been accounted for in Figure 6.4. Figure 6.5 shows a similar plot considering monodispersed particles. In Figure 6.4, n_1/n_0 decreases exponentially giving rise to the formation of dimers, trimers and so on. Ethyl acetate and methanol based inks appear to be unstable compared to ethanol and IPA based on a rapid drop in the particle concentration, whereas IPA based ink appears to be the most stable. The normalized concentration of the particles (n_t/n_0) plotted with respect to time t is

shown in Figure 6.5. Similar to Figure 6.4, the decay in particle concentration is seen to be delayed for the case of an IPA based ink as compared to others, as observed experimentally. Comparing the Figures 6.4 and 6.5, it can be seen that assuming monodispersity results in a reduced stability time for all the DM cases considered. One of the reasons for this is thought to be due to the fixed value of W used in this case.

Considering a particle size of 300 nm (assumed threshold limit), the ratio n_t/n_0 was calculated to be 0.0011 based on very loose packing density of 0.5236 for monodispersed spherical particles [161]. Based on Figure 6.5, this corresponded to a time of 6.7 hours, 12.2 hours, 3.5 days and 110 days for ethyl acetate, methanol, ethanol and IPA respectively. Table 6.3 shows a comparison of the experimentally observed and calculated stability time. The calculated values largely over-predict the time until which the ink will remain dispersed, except for the case of ethanol, however the correct trends are observed. The difference appears to be higher for dispersions that are unstable, i.e., ethyl acetate and methanol.

Table 6.3 – Comparison of stability time for carbon dispersion in the respective DM based on visual inspections and calculated values

DM	Experimental observation	Calculated value
Ethyl Acetate	< 2 minutes	6.7 hours
Methanol	< 2 minutes	12.2 hours
Ethanol	8-12 days	3.5 days
Iso-propanol	30 - 40 days	110 days

Discrepancy between the measured and calculated values of the stability time for the different DM may arise from the validity of the assumptions that have been made in the calculations. For simplicity, the carbon particles and aggregates have been assumed to be perfectly spherical. This may not be true since the nanoparticle aggregates may represent fractal-like structures instead of spherical aggregates [162]. Other forms of aggregation such as orthokinetic aggregation and differential sedimentation may influence the rates of aggregation in the later stages of the process. Also, the set limit for threshold particle size is subjective and will depend on how stable we want the colloidal system to be. In-spite of these differences, the experimental observations of ink stability can be qualitatively explained with the model. Given the primary particle size and its surface charge in a DM, it is possible to predict the stability of the ink dispersion.
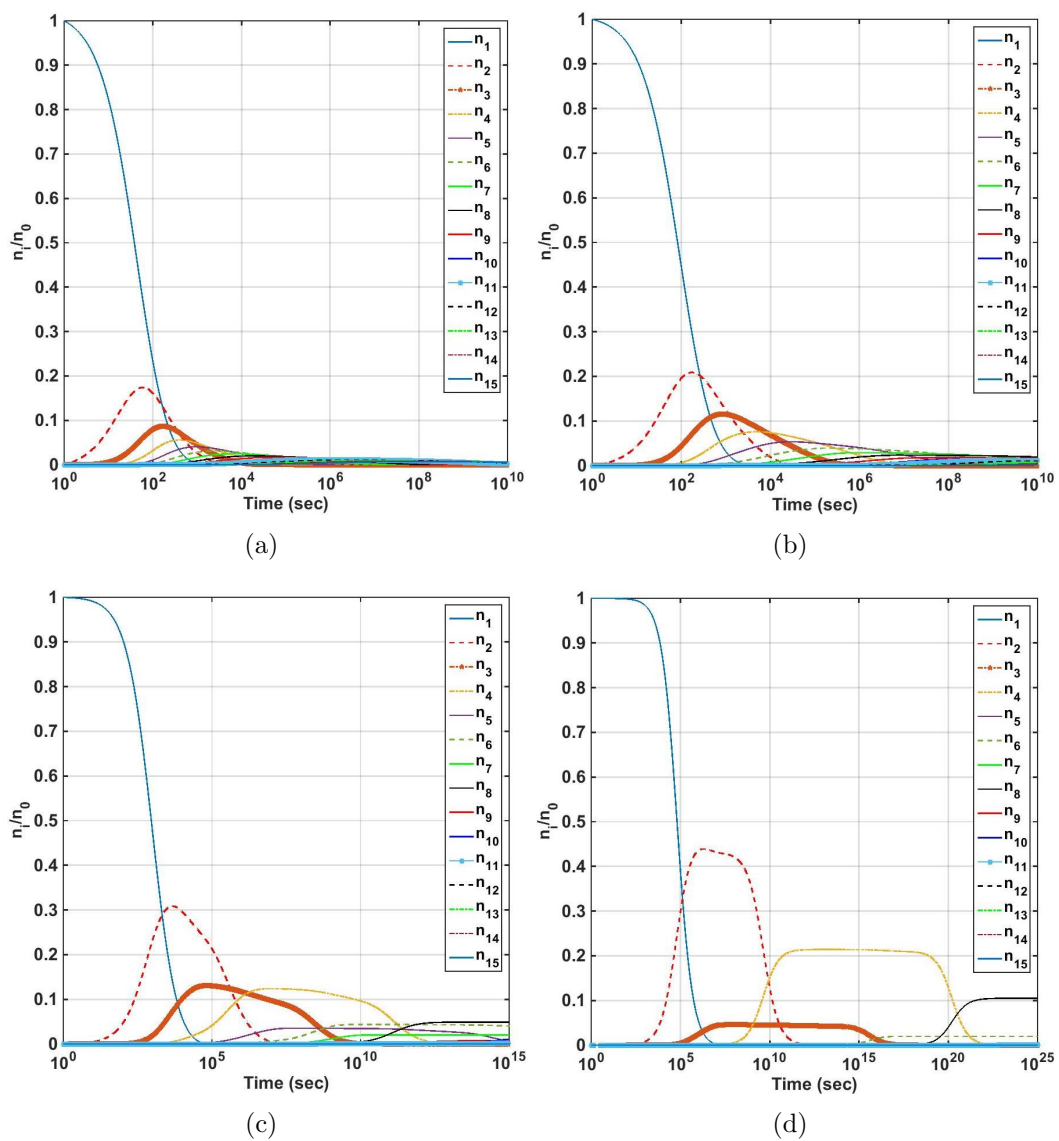
Figure 6.4 – Rate of change of monomer units (n_1 to n_{15}) with time based on equation (6.10) (a) ethyl acetate (b) methanol (c) ethanol and (d) IPA
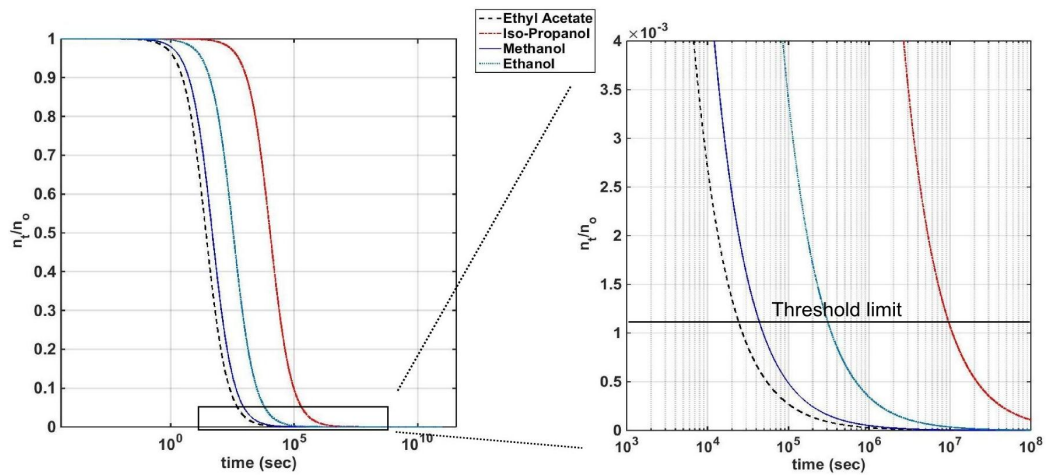
Figure 6.5 – Rate of decay in particle concentration (normalized) with time for ethyl acetate, methanol, ethanol and IPA based inks based on equation (6.11). Magnified image shows the concentration when the particle size reaches 300 nm based on loose random packing

6.3.2 Effect of Nafion

Apart from facilitating protonic transport through the electrodes, addition of Nafion ionomer to the ink also serves to enhances the ink stability by providing an additional repulsive energy between the particles in the form of steric interaction. It was observed that carbon particles that may be unstable in a DM may become stable after addition of Nafion. Quantification of the steric potential is complex because of its dependence on a number of parameters such as the type of DM, temperature, attachment mechanism, polymer concentration [157]. For the reasons above and due to the lack of quantitative literature data, the steric interaction potential was not implemented in the model. The effect of Nafion addition on the ink stability was however studied experimentally.

Experiments were performed to study the effect of Nafion by adding 30 wt% Nafion ionomer for each DM type and the ink stability was analyzed. The rate of change in particle size with time for Nafion loadings of 10 wt.%, 30wt% and 50 wt.% was also carried out for the case of IPA based ink to see if the particle size was a function of the amount of ionomer added.

Addition of Nafion increased the ink stability time for the two DM cases, ethyl acetate and methanol that were unstable prior to the addition of Nafion as well as resulted in a reduced measured particle size for the IPA based ink. However, unlike the methanol based ink, DM containing ethyl acetate remained stable for only a few hours. Table 6.4 shows the particle sizes using DLS before and after the addition of Nafion. Methanol and IPA based DM show a lower particle size compared to ethyl acetate based DM after ionomer was added. Apart from the lower stability, another reason for the higher measured particle size for the case of ethyl acetate might be an experimental artifact due to the nature of measurement technique. As discussed earlier, DLS measures the hydrodynamic diameter of the particles/aggregates including the attached polymer chains around the particles which may be different than the actual particle size. Based on the dielectric constants of the DM, Nafion chains will attach to the carbon particles only in presence of ethyl acetate but not in IPA and methanol [101, 102].

Theoretical quantification of the stability time for DM with the ionomer is not possible since the steric term has not been accounted for in the model. However, an explanation based on the magnitude of Coulombic interaction for the experimental

124

Table 6.4 – Average particle radius (nm) measured using DLS for carbon black dispersed in IPA, methanol and ethyl acetate with and without Nafion ionomer

IPA		Methanol		Ethyl Acetate	
Without Nafion	With Nafion	Without Nafion	With Nafion	Without Nafion	With Nafion
402±30	133±6	unstable	137±5	unstable	511±149

observation could be given. The zeta potential or particle surface charge which affects the magnitude of the Coulombic interaction between the particles, changes with the ion concentration [162]. It has been observed that addition of Nafion solution (mixture of water and volatile organic compounds) to the DM increases the H^+ ion concentration since the ionomer is acidic in nature due to the presence of sulphonic acid groups. This will affect the surface charge of the particles [162]. A parametric study of surface charge was carried out for the four DM as shown in Figure 6.6. For a particle size of 30 nm, the maximum dimensionless interaction energy (U/k_BT) is plotted against surface charge ranging from -100 mV to +100 mV. Interaction energy was found to be a strong function of the surface charge for the case of IPA, ethanol and methanol compared to ethyl acetate. Thus, any change in ζ resulting from the addition of ionomer would cause a greater increase in the repulsive interaction energy for the case of IPA and methanol as compared to ethyl acetate.

Finally, in order to determine whether the particle size was a function of the amount of Nafion being introduced in the ink, three inks with Nafion loadings of 10 wt%, 30 wt% and 50 wt% were prepared using IPA as the DM. The particle size for the prepared samples was measured using DLS with varying time intervals from 2 hours to 14 days. Figure 6.7 shows the average particle size measured for the three Nafion loading cases. No specific trend for particle size with time was observed. Even after 14 days, there was no increase in particle size for each of the three Nafion loading cases. Similar results were also obtained using non-diluted inks (Nanoplus 3, Micrometrics). Thus, even a small amount of ionomer added to the ink is sufficient to increase its stability for a prolonged period of time for the IPA based ink.
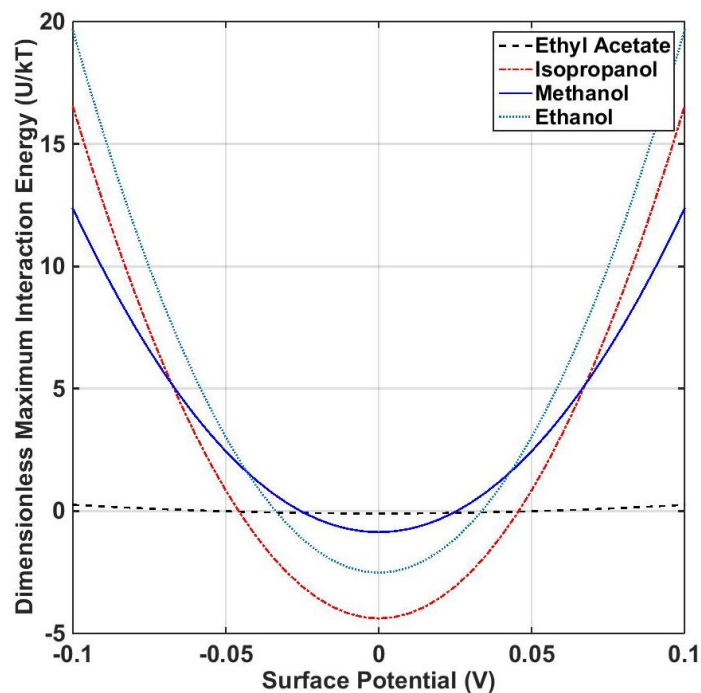
Figure 6.6 – Effect of surface charge on maximum interaction energy for the dispersion media. IPA, methanol and ethanol show a higher dependence on the charge as compared to ethyl acetate
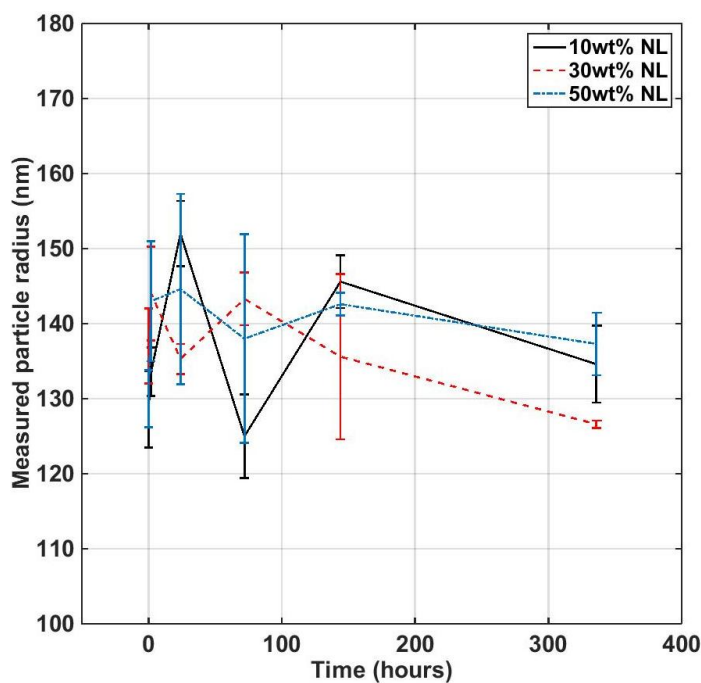
Figure 6.7 – Effect of Nafion loading on particle size for carbon black in IPA based ink

6.4 Conclusions

Effect of dispersion media on the stability of carbon black was reported for the case of non-aqueous media - IPA, methanol, ethanol and ethyl acetate. The stability time for ink dispersions based on visual inspection was carried out for the four DM. Of the studied dispersion solvents, IPA was found to be the best dispersing agent for carbon. In order to understand the experimental observations and to rationalize the solvent selection, a simple semi-empirical model comprising of van der Waals and Coulombic interactions was implemented to calculate the stability ratios and rates of aggregation. Quantification of settling time for the carbon inks in the four DM was carried out using diffusion limited aggregation kinetics and assuming a threshold aggregate size of 300 nm based on the sedimentation - diffusion equilibrium. A qualitative comparison with the experimental observations was confirmed. Addition of the Nafion ionomer helped to increase the ink stability and reduce the particle size. The increase in ink stability with Nafion addition was observed to be independent of the amount of Nafion used. Particle radii for the studied inks in presence of Nafion were 511±149 nm, 137±5 nm and 133±6 nm for the case of ethyl acetate, methanol and IPA respectively.

It is believed that the application of colloidal theories to predict the ink dispersion will help in optimizing the choice of the dispersion media to be used and help in an increased ink standing time for larger commercial processes. A reduced aggregate size in the ink and subsequently the catalyst layer will help in increasing the Pt utilization by improving the micro-scale transport.

Chapter 7

Conclusion and Future Work

Reducing the Pt loading in PEFC electrodes is essential for lowering fuel cell manufacturing costs which is required for large scale commercialization [163]. The catalyst layer fabrication process governs the Pt loading and distribution, microstructure and eventually the Pt utilization and electrode performance. Inkjet printing has the potential of fabricating thin, low Pt loading electrodes with a high transfer efficiency by allowing precise control over the deposition process. However, a thorough analysis of inkjet printed electrode characterization has been lacking in the literature. This work presents a detailed experimental analysis of the inkjet printed electrodes as well as testing of modified electrode structures. To improve ink formulations, an analysis of ink dispersion was also performed.

In summary, the thesis presents,

- A detailed analysis of inkjet printed PEFC electrodes including the effect of Nafion and Pt loading on the microstructure, electrochemical performance and the evaluation of transport resistance

- Fabrication and testing of modified electrode structures, i.e., electrode coated membrane containing a carbon layer over the CL and patterned electrodes in an attempt to improve mass transport

- Study of ink dispersion stability in order to rationalize the dispersion solvents based on DLVO type particle interactions

7.1   Conclusions

Utilizing inkjet printing for electrode fabrication and analysis of the fabricated electrode microstructures has been carried out in this work. The main challenges were

the formulation of a catalyst ink that worked with the printer, improving the kinetic performance of the inkjet printed electrodes and developing new architectures for improving the mass transport. The following paragraphs describe the main conclusions of the work with regards to the effect of Nafion loading on thin, low Pt loading IJP electrodes, analysis of electrode kinetics and transport resistance for IJP electrodes, application of IJP for direct deposition of MPLs over CLs and to create patterned electrode structures and finally the study on ink dispersion using colloidal particle interactions.

To understand the effect of Nafion loading in low loading and thin electrodes, inkjet printed electrodes with a Pt loading of 0.026 mg/cm^2 and electrode thickness between 1.5 - 2 μm were fabricated and tested with cathodic Nafion loadings ranging from 10 wt% to 50 wt%. Ex-situ SEM visualization of the electrodes revealed that particle size increased with increasing Nafion loading even though electrode thicknesses remained similar. In-situ testing showed minimal variation in the performance for electrodes with Nafion loadings between 20 - 40 wt%, unlike conventionally fabricated electrodes. Proton transport limitations were only observed when the Nafion loading was 10 wt% whereas the transport losses are evident at a higher Nafion loading of 50 wt%. Compared to spray coated electrodes, peak mass activity and Pt utilization for the inkjet printed electrodes were almost 10 times higher. In the kinetic region however, the inkjet printed electrodes performed poorly as compared to the spray coated electrode.

Mitigating the poor electrode kinetics for the inkjet printed electrodes was dealt with by increasing the Pt loading by increasing the number of printed passes. Analysis of electrode microstructure and performance with varying Pt loading was carried out. It was observed that porosity and active area of the electrodes decreased with increasing number of passes leading to a threshold Pt loading above which gains in cell performance were substantially reduced. Kinetic analysis showed that Tafel slope increased with decreasing Pt loading and oxygen partial pressure when the measured cell voltage dropped below 0.75 - 0.8 V, where the oxygen reduction reaction is known to change its mechanism. An improvement in the kinetic performance of the low Pt loading IJP electrodes could therefore be achieved by operating at higher back-pressures.

Experiments to measure the limiting current density were carried out using 1% oxygen as the cathodic reactant. Based on the value of limiting current density, the

total transport resistance, R_{total}, and subsequently the local transport resistance for oxygen was evaluated. At a cell temperature of 80°C, R_{total} decreased with increasing RH from 50% to 90%. The local transport resistance was also found to decrease from 5.93±3.16 s/cm to 3.43±1.67 s/cm from 50% to 90%. These values of local transport resistances were found to be similar to the ones reported in literature for conventionally fabricated electrodes thereby indicating that the IJP fabrication method does not impose any additional local transport losses in the electrodes. Even at higher Pt loadings, the lower performance of IJP electrodes compared to conventional electrodes was therefore associated to their lower active area and porosity.

Improving the mass transport region for the inkjet printed electrodes was dealt using two approaches, (a) fabrication of a novel electrode coated membrane (ECM) architecture where the micro-porous layer is printed directly over the CL to help reduce the transport resistance and (b) fabrication of patterned electrode structures in order to have pathways for the reactant and water transport across the electrodes. In the former case, ECMs were fabricated by depositing carbon/Nafion based ink over the CLs using inkjet printing. After 20 printed passes, the thickness of the carbon layer was found to be 5.6±0.5 μm. Compared to a standard inkjet printed electrode with similar Pt loading and incorporating a commercial diffusion media, performance in the kinetic region was reduced but the performance in the high current density region was higher due to the reduced thickness of the micro-porous layer. Based on the limiting current density experiments, the ECM showed a lower value of R_{total} as compared to a CL incorporating 24BC GDL.

In the latter approach, patterned electrodes were fabricated using inkjet printing and the performance was compared to a non-patterned electrode having a similar Pt loading. Due to lower pattern resolution, i.e., between 300 and 350 μm, fine enough patterns to show an advantage of patterned structures could not be observed.

Finally, a colloidal science based study relating ink stability to the type of dispersion solvent was done by implementing van der Waals and Coulombic particle interactions. A semi-empirical model based on diffusion limited aggregation of particles was used to predict the aggregation rate and stability time. Experimental validation using carbon based inks in IPA, ethyl acetate, methanol and ethanol was carried out by visual inspection for stability and dynamic light scattering to determine the particle size. The model was able to qualitatively predict whether the dispersion solvent was suited to achieve a stable carbon dispersion.
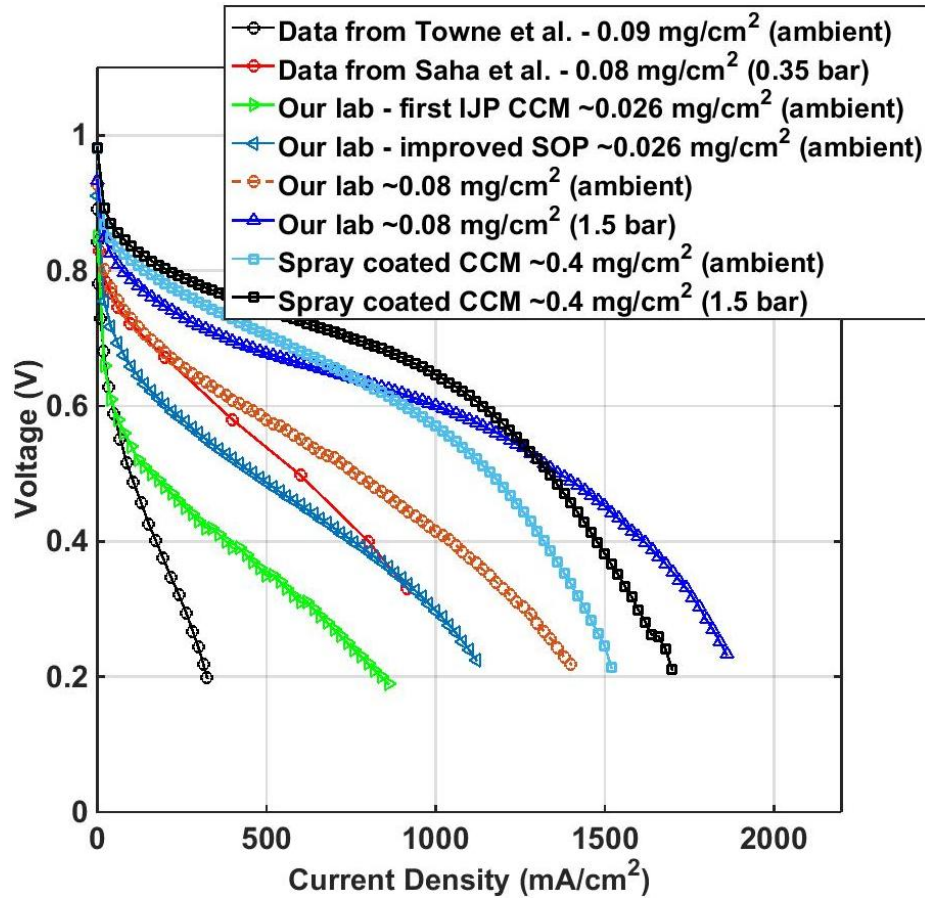
Figure 7.1 – Performance evolution of IJP electrodes compared to literature. Data from Towne et al. [5] and Saha et al. [3] is at 75°C, 100% RH (ambient) and 60°C, 100% RH (35 kPa) respectively. IJP CCMs for this work are shown at 70% RH, 80°C [6, 7]

Figure 7.1 shows the evolution of inkjet printed fuel cell performance before and after this work. Taking advantage of our increasing knowledge in ink fabrication and sensitivity to operating conditions, an improvement in fuel cell performance under H_2/air conditions was achieved without increasing the Pt loading and a substantial change in operating conditions. As seen from Figure 7.1, a performance improvement of around 0.14 V at 0.5 A/cm^2 was achieved using an improved SOP while maintaining the Pt loading of ∼0.026 mg/cm^2 in this work. For a Pt loading of around 0.08 mg/cm^2, performance of the electrode prepared in-house (at ambient pressure) is comparable to that reported by Saha et a. [3] at 35 kPa (gauge). As compared to the spray coated electrode, the effect of increased pressure operation is seen to be greater for the IJP CCM.

Based on the targets set by the US, Department of Energy (DOE) [164], the 2015 status of the performance at rated power at a pressure of 250 kPa (absolute) is 1060 mW/cm^2. On the other hand, the performance of the IJP CCMs with cathodic loadings of 0.08 and 0.4 mg/cm^2 are measured to be 149 mW/cm^2 and 362 mW/cm^2 respectively at the rated power (0.76 V). Thus, in order to meet the set targets by the US DOE, more efforts to improve the performance of IJP electrodes, especially at low overpotentials is needed.

7.2   Scope of future work

Even though application of inkjet printing to electrode fabrication has many advantages over using conventional methods, the reduced porosity and active area may hinder its applicability when considering higher Pt loading electrodes, as illustrated in this work. Zlotorowicz et al. [165] recently reported an enhanced electrode porosity by implementing monodispersed polystyrene particles during the CL fabrication resulting in a better fuel cell performance. The addition of pore-formers may thus help increase the electrode porosity for IJP electrodes. Alternatively, increasing the catalyst particle concentration in the ink would require lesser number of printed passes to achieve the desired Pt loading. Since it has been shown that there is a non-linear increase in the CL thickness with number of printed passes, this would result in a higher electrode porosity. It is believed that a change in the pore-size distribution due to the added porosity may also help to improve the active area leading to better electrode kinetics.

With regards to the study of ECMs, a parametric study of Nafion loading and thickness for the carbon micro-porous layers can be carried out. Ahn et al. [96] have reported an optimal Nafion loading value of 10 wt% in the MPL. Therefore, reducing the Nafion loading from 30 wt% to 10 wt% in the carbon layer of the ECM might improve its performance under very wet conditions.

Analyzing the inkjet printed CL durability was not part of this work, and has not been reported in the literature. Performance degradation has been observed at an accelerated rate in low Pt loading electrodes compared to conventional loading electrodes [166]. Thus, a durability analysis of the low Pt loading IJP electrodes which is essential to automotive fuel cells is another area of future investigation.

The semi-empirical DLVO based model presented in this work for ink analysis can

be improved further by adding the effect of Nafion ionomer that is ideally present in the catalyst ink. Values of zeta potential for the particles can be experimentally measured and used to test the applicability of the model for a wide range of dispersion solvents.

References

[1] Owejan J. P, Owejan J. E, and Gu W. Impact of platinum loading and catalyst layer structure on pemfc performance. *Journal of The Electrochemical Society*, 160(8):F824–F833, 2013.

[2] Qi Z and Kaufman A. Low pt loading high performance cathodes for pem fuel cells. *Journal of Power Sources*, 113(1):37–43, 2003.

[3] Saha M. S, Malevich D, Halliop E, Pharoah J. G, Peppley B. A, and Karan K. Electrochemical activity and catalyst utilization of low pt and thickness controlled membrane electrode assemblies. *Journal of The Electrochemical Society*, 158(5):B562–B567, 2011.

[4] Nonoyama N, Okazaki S, Weber A, Ikogi Y, and Yoshida T. Analysis of oxygen-transport diffusion resistance in proton-exchange-membrane fuel cells. *Journal of The Electrochemical Society*, 158(4):B416–B423, 2011.

[5] Towne S, Viswanathan V, Holbery J, and Rieke P. Fabrication of polymer electrolyte membrane fuel cell meas utilizing inkjet print technology. *Journal of Power Sources*, 171(2):575–584, 2007.

[6] Shukla S, Taufertshofer K, Bhattacharjee S, Secanell M, Halliop E, Malevich D, and Karan K. Effect of ionomer loading in inket printed catalyst coated membranes on pefc performance. In *ASME 2012 10th International Conference on Fuel Cell Science, Engineering and Technology collocated with the ASME 2012 6th International Conference on Energy Sustainability*, pages 123–128. American Society of Mechanical Engineers, 2012.

[7] Shukla S, Domican K, and Secanell M. Analysis of kinetic parameters and effect of pt loading on cell performance of pefc electrodes prepared by inkjet printing. *ECS Transactions*, 69(17):761–772, 2015.

[8] Litster S and McLean G. Pem fuel cell electrodes. *Journal of Power Sources*, 130(1):61–76, 2004.

[9] Larminie J, Dicks A, and McDonald M. S. *Fuel cell systems explained*, volume 2. Wiley New York, 2003.

[10] Mathias M, Roth J, Fleming J, and Lehnert W. Diffusion media materials and characterisation. *Handbook of fuel cells*, 2003.

[11] Weber A. Z and Newman J. Effects of microporous layers in polymer electrolyte fuel cells. *Journal of the Electrochemical Society*, 152(4):A677–A688, 2005.

[12] Gostick J. T, Ioannidis M. A, Fowler M. W, and Pritzker M. D. On the role of the microporous layer in pemfc operation. *Electrochemistry Communications*, 11(3):576–579, 2009.

[13] O'Hayre R. P, Cha S.-W, Colella W, and Prinz F. B. *Fuel cell fundamentals*, volume 2. John Wiley & Sons New York, 2006.

[14] Andress D, Das S, Joseck F, and Nguyen T. D. Status of advanced light-duty transportation technologies in the us. *Energy Policy*, 41:348–364, 2012.

[15] Eikerling M, Kornyshev A, and Kulikovsky A. Can theory help to improve fuel cells. *Fuel Cell Rev*, 1:15–25, 2005.

[16] Wang Y, Chen K. S, Mishler J, Cho S. C, and Adroher X. C. A review of polymer electrolyte membrane fuel cells: technology, applications, and needs on fundamental research. *Applied Energy*, 88(4):981–1007, 2011.

[17] Wee J.-H, Lee K.-Y, and Kim S. H. Fabrication methods for low-pt-loading electrocatalysts in proton exchange membrane fuel cell systems. *Journal of Power Sources*, 165(2):667–677, 2007.

[18] Wilson M. S and Gottesfeld S. Thin-film catalyst layers for polymer electrolyte fuel cell electrodes. *Journal of applied electrochemistry*, 22(1):1–7, 1992.

[19] Wilson M. S and Gottesfeld S. High performance catalyzed membranes of ultra-low pt loadings for polymer electrolyte fuel cells. *Journal of the Electrochemical Society*, 139(2):L28–L30, 1992.

[20] Paganin V, Ticianelli E, and Gonzalez E. Development and electrochemical studies of gas diffusion electrodes for polymer electrolyte fuel cells. *Journal of Applied Electrochemistry*, 26(3):297–304, 1996.

[21] Prater K. B. Solid polymer fuel cells for transport and stationary applications. *Journal of Power Sources*, 61(1):105–109, 1996.

[22] Kumar G. S, Raja M, and Parthasarathy S. High performance electrodes with very low platinum loading for polymer electrolyte fuel cells. *Electrochimica Acta*, 40(3):285–290, 1995.

[23] Voss H, Wilkinson D, Pickup P, Johnson M, and Basura V. Anode water removal: a water management and diagnostic technique for solid polymer fuel cells. *Electrochimica Acta*, 40(3):321–328, 1995.

[24] Ralph T, Hards G, Keating J, Campbell S, Wilkinson D, Davis M, St-Pierre J, and Johnson M. Low cost electrodes for proton exchange membrane fuel cells performance in single cells and ballard stacks. *Journal of the Electrochemical Society*, 144(11):3845–3857, 1997.

[25] Wilson M. S, Valerio J. A, and Gottesfeld S. Low platinum loading electrodes for polymer electrolyte fuel cells fabricated using thermoplastic ionomers. *Electrochimica Acta*, 40(3):355–363, 1995.

[26] Kriston Á, Xie T, Gamliel D, Ganesan P, and Popov B. N. Effect of ultra-low pt loading on mass activity of polymer electrolyte membrane fuel cells. *Journal of Power Sources*, 243:958–963, 2013.

[27] Xie Z, Zhao X, Adachi M, Shi Z, Mashio T, Ohma A, Shinohara K, Holdcroft S, and Navessin T. Fuel cell cathode catalyst layers from green catalyst inks. *Energy & Environmental Science*, 1(1):184–193, 2008.

[28] Holdcroft S. Ionomer in the catalyst layer. *ECS Transactions*, 50(2):47–50, 2013.

[29] Lee M, Uchida M, Yano H, Tryk D. A, Uchida H, and Watanabe M. New evaluation method for the effectiveness of platinum/carbon electrocatalysts under operating conditions. *Electrochimica Acta*, 55(28):8504–8512, 2010.

[30] Shin S.-J, Lee J.-K, Ha H.-Y, Hong S.-A, Chun H.-S, and Oh I.-H. Effect of the catalytic ink preparation method on the performance of polymer electrolyte membrane fuel cells. *Journal of power sources*, 106(1):146–152, 2002.

[31] Neyerlin K, Gu W, Jorne J, and Gasteiger H. A. Determination of catalyst unique parameters for the oxygen reduction reaction in a pemfc. *Journal of the Electrochemical Society*, 153(10):A1955–A1963, 2006.

[32] Gasteiger H, Panels J, and Yan S. Dependence of pem fuel cell performance on catalyst loading. *Journal of Power Sources*, 127(1):162–171, 2004.

[33] Suzuki T, Tsushima S, and Hirai S. Fabrication and performance evaluation of structurally-controlled pemfc catalyst layers by blending platinum-supported and stand-alone carbon black. *Journal of Power Sources*, 233:269–276, 2013.

[34] Okur O, Karadağ Ç. İ, San F. G. B, Okumuş E, and Behmenyar G. Optimization of parameters for hot-pressing manufacture of membrane electrode assembly for pem (polymer electrolyte membrane fuel cells) fuel cell. *Energy*, 57:574–580, 2013.

[35] Andersen S. M, Dhiman R, Larsen M. J, and Skou E. Importance of electrode hot-pressing conditions for the catalyst performance of proton exchange membrane fuel cells. *Applied Catalysis B: Environmental*, 172:82–90, 2015.

[36] Su H.-N, Zeng Q, Liao S.-J, and Wu Y.-N. High performance membrane electrode assembly with ultra-low platinum loading prepared by a novel multi catalyst layer technique. *International journal of hydrogen energy*, 35(19):10430–10436, 2010.

[37] Martin S, Garcia-Ybarra P, and Castillo J. Electrospray deposition of catalyst layers with ultra-low pt loadings for pem fuel cells cathodes. *Journal of Power Sources*, 195(9):2443–2449, 2010.

[38] Ohma A, Mashio T, Sato K, Iden H, Ono Y, Sakai K, Akizuki K, Takaichi S, and Shinohara K. Analysis of proton exchange membrane fuel cell catalyst layers for reduction of platinum loading at nissan. *Electrochimica Acta*, 56(28): 10832–10841, 2011.

[39] Tian Z. Q, Lim S. H, Poh C. K, Tang Z, Xia Z, Luo Z, Shen P. K, Chua D, Feng Y. P, Shen Z, and others . A highly order-structured membrane electrode assembly with vertically aligned carbon nanotubes for ultra-low pt loading pem fuel cells. *Advanced Energy Materials*, 1(6):1205–1214, 2011.

[40] Brodt M, Wycisk R, and Pintauro P. N. Nanofiber electrodes with low platinum loading for high power hydrogen/air pem fuel cells. *Journal of the Electrochemical Society*, 160(8):F744–F749, 2013.

[41] Gruber D, Ponath N, Müller J, and Lindstaedt F. Sputter-deposited ultra-low catalyst loadings for pem fuel cells. *Journal of Power Sources*, 150:67–72, 2005.

[42] Greszler T. A, Caulk D, and Sinha P. The impact of platinum loading on oxygen transport resistance. *Journal of The Electrochemical Society*, 159(12): F831–F840, 2012.

[43] Wang X, Richey F. W, Wujcik K. H, and Elabd Y. A. Ultra-low platinum loadings in polymer electrolyte membrane fuel cell electrodes fabricated via simultaneous electrospinning/electrospraying method. *Journal of Power Sources*, 264:42–48, 2014.

[44] Millington B, Whipple V, and Pollet B. G. A novel method for preparing proton exchange membrane fuel cell electrodes by the ultrasonic-spray technique. *Journal of Power Sources*, 196(20):8500–8508, 2011.

[45] Li G and Pickup P. G. Ionic conductivity of pemfc electrodes effect of nafion loading. *Journal of The Electrochemical Society*, 150(11):C745–C752, 2003.

[46] Lee S, Mukerjee S, McBreen J, Rho Y, Kho Y, and Lee T. Effects of nafion impregnation on performances of pemfc electrodes. *Electrochimica Acta*, 43(24): 3693–3701, 1998.

[47] Lai C.-M, Lin J.-C, Ting F.-P, Chyou S.-D, and Hsueh K.-L. Contribution of nafion loading to the activity of catalysts and the performance of pemfc. *international journal of hydrogen energy*, 33(15):4132–4137, 2008.

[48] Xie J, Xu F, Wood D. L, More K. L, Zawodzinski T. A, and Smith W. H. Influence of ionomer content on the structure and performance of pefc membrane electrode assemblies. *Electrochimica Acta*, 55(24):7404–7412, 2010.

[49] Xie Z, Navessin T, Shi K, Chow R, Wang Q, Song D, Andreaus B, Eikerling M, Liu Z, and Holdcroft S. Functionally graded cathode catalyst layers for polymer electrolyte fuel cells ii. experimental study of the effect of nafion distribution. *Journal of the Electrochemical Society*, 152(6):A1171–A1179, 2005.

[50] Martin S, Garcia-Ybarra P, and Castillo J. High platinum utilization in ultra-low pt loaded pem fuel cell cathodes prepared by electrospraying. *international journal of hydrogen energy*, 35(19):10446–10451, 2010.

[51] Sasikumar G, Ihm J, and Ryu H. Dependence of optimum nafion content in catalyst layer on platinum loading. *Journal of Power Sources*, 132(1):11–17, 2004.

[52] Sasikumar G, Ihm J, and Ryu H. Optimum nafion content in pem fuel cell electrodes. *Electrochimica Acta*, 50(2):601–605, 2004.

[53] Kim K.-H, Lee K.-Y, Kim H.-J, Cho E, Lee S.-Y, Lim T.-H, Yoon S. P, Hwang I. C, and Jang J. H. The effects of nafion® ionomer content in pemfc meas

prepared by a catalyst-coated membrane (ccm) spraying method. *International Journal of Hydrogen Energy*, 35(5):2119–2126, 2010.

[54] Passalacqua E, Lufrano F, Squadrito G, Patti A, and Giorgi L. Nafion content in the catalyst layer of polymer electrolyte fuel cells: effects on structure and performance. *Electrochimica Acta*, 46(6):799–805, 2001.

[55] Antolini E, Giorgi L, Pozio A, and Passalacqua E. Influence of nafion loading in the catalyst layer of gas-diffusion electrodes for pefc. *Journal of Power Sources*, 77(2):136–142, 1999.

[56] Lee D and Hwang S. Effect of loading and distributions of nafion ionomer in the catalyst layer for pemfcs. *International Journal of Hydrogen Energy*, 33 (11):2790–2794, 2008.

[57] Hirano S, Kim J, and Srinivasan S. High performance proton exchange membrane fuel cells with sputter-deposited pt layer electrodes. *Electrochimica Acta*, 42(10):1587–1593, 1997.

[58] Cha S and Lee W. Performance of proton exchange membrane fuel cell electrodes prepared by direct deposition of ultrathin platinum on the membrane surface. *Journal of the Electrochemical Society*, 146(11):4055–4060, 1999.

[59] OHayre R, Lee S.-J, Cha S.-W, and Prinz F. B. A sharp peak in the performance of sputtered platinum fuel cells at ultra-low platinum loading. *Journal of Power Sources*, 109(2):483–493, 2002.

[60] Debe M. K, Schmoeckel A, Hendricks S, Vernstrom G, Haugen G, and Atanasoski R. Durability aspects of nanostructured thin film catalysts for pem fuel cells. *ECS Transactions*, 1(8):51–66, 2006.

[61] Debe M. K. Nanostructured thin film electrocatalysts for pem fuel cells-a tutorial on the fundamental characteristics and practical properties of nstf catalysts. *Ecs Transactions*, 45(2):47–68, 2012.

[62] Debe M. K. Tutorial on the fundamental characteristics and practical properties of nanostructured thin film (nstf) catalysts. *Journal of the Electrochemical Society*, 160(6):F522–F534, 2013.

[63] Debe M. K. Electrocatalyst approaches and challenges for automotive fuel cells. *Nature*, 486(7401):43–51, 2012.

[64] Cavarroc M, Ennadjaoui A, Mougenot M, Brault P, Escalier R, Tessier Y, Durand J, Roualdès S, Sauvage T, and Coutanceau C. Performance of plasma sputtered fuel cell electrodes with ultra-low pt loadings. *Electrochemistry Communications*, 11(4):859–861, 2009.

[65] Xiong L and Manthiram A. High performance membrane-electrode assemblies with ultra-low pt loading for proton exchange membrane fuel cells. *Electrochimica Acta*, 50(16):3200–3204, 2005.

[66] Taylor A. D, Kim E. Y, Humes V. P, Kizuka J, and Thompson L. T. Inkjet printing of carbon supported platinum 3-d catalyst layers for use in fuel cells. *Journal of Power Sources*, 171(1):101–106, 2007.

[67] Saha M. S, Paul D, Malevich D, Peppley B, and Karan K. Preparation of ultra-thin catalyst layers by piezo-electric printer for pemfcs applications. *ECS Transactions*, 25(1):2049–2059, 2009.

[68] Saha M. S, Tam M, Berejnov V, Susac D, McDermid S, Hitchcock A. P, and Stumper J. Characterization and performance of catalyst layers prepared by inkjet printing technology. *ECS Transactions*, 58(1):797–806, 2013.

[69] Malevich D, Saha M. S, Halliop E, Peppley B. A, Pharoah J. G, and Karan K. Performance characteristics of pefcs with patterned electrodes prepared by piezo-electric printing. *ECS Transactions*, 50(2):423–427, 2013.

[70] Klingele M, Breitwieser M, Zengerle R, and Thiele S. Direct deposition of proton exchange membranes enabling high performance hydrogen fuel cells. *Journal of Materials Chemistry A*, 3(21):11239–11245, 2015.

[71] Breitwieser M, Klingele M, Britton B, Holdcroft S, Zengerle R, and Thiele S. Improved pt-utilization efficiency of low pt-loading pem fuel cell electrodes using direct membrane deposition. *Electrochemistry Communications*, 60:168–171, 2015.

[72] Yazdanpour M, Esmaeilifar A, and Rowshanzamir S. Effects of hot pressing conditions on the performance of nafion membranes coated by ink-jet printing of pt/mwcnts electrocatalyst for pemfcs. *international journal of hydrogen energy*, 37(15):11290–11298, 2012.

[73] Wang Z and Nagao Y. Effects of nafion impregnation using inkjet printing for membrane electrode assemblies in polymer electrolyte membrane fuel cells. *Electrochimica Acta*, 129:343–347, 2014.

[74] Shukla S, Domican K, Karan K, Bhattacharjee S, and Secanell M. Analysis of low platinum loading thin polymer electrolyte fuel cell electrodes prepared by inkjet printing. *Electrochimica Acta*, 156:289–300, 2015.

[75] Shukla S, Domican K, and Secanell M. Effect of electrode patterning on pem fuel cell performance using ink-jet printing method. *ECS Transactions*, 64(3): 341–352, 2014.

[76] Weber A. Z and Kusoglu A. Unexplained transport resistances for low-loaded fuel-cell catalyst layers. *J. Mater. Chem. A*, 2014.

[77] Su H, Liao S, S. , and Gao H. Performance of an ultra-low platinum loading membrane electrode assembly prepared by a novel catalyst-sprayed membrane technique. *Journal of Power Sources*, 195(3):756–761, 2010.

[78] Baker D, Caulk D, Neyerlin K, and Murphy M. Measurement of oxygen transport resistance in pem fuel cells by limiting current methods. *Journal of The Electrochemical Society*, 156(9):B991–B1003, 2009.

[79] Liu H, Epting W, and Litster S. Gas transport resistance in polymer electrolyte thin films on oxygen reduction reaction catalysts. *Langmuir*, 31(36):9853–9858, 2015.

[80] Hao L, Moriyama K, Gu W, and Wang C. Modeling and experimental validation of pt loading and electrode composition effects in pem fuel cells. *Journal of The Electrochemical Society*, 162(8):F854–F867, 2015.

[81] Secanell M, Putz A, Shukla S, Wardlaw P, Bhaiya M, Pant L, and Sabharwal M. Mathematical modelling and experimental analysis of thin, low-loading fuel cell electrodes. *ECS Transactions*, 69(17):157–187, 2015.

[82] Suzuki T, Kudo K, and Morimoto Y. Model for investigation of oxygen transport limitation in a polymer electrolyte fuel cell. *Journal of Power Sources*, 222:379–389, 2013.

[83] Jinnouchi R, Kudo K, Kitano N, and Morimoto Y. Molecular dynamics simulations on o 2 permeation through nafion ionomer on platinum surface. *Electrochimica Acta*, 188:767–776, 2016.

[84] Beuscher U. Experimental method to determine the mass transport resistance of a polymer electrolyte fuel cell. *Journal of The Electrochemical Society*, 153 (9):A1788–A1793, 2006.

[85] Ono Y, Mashio T, Takaichi S, Ohma A, Kanesaka H, and Shinohara K. The analysis of performance loss with low platinum loaded cathode catalyst layers. *ECS Transactions*, 28(27):69–78, 2010.

[86] Wang X, Zhang H, Zhang J, Xu H, Tian Z, Chen J, Zhong H, Liang Y, and Yi B. Micro-porous layer with composite carbon black for pem fuel cells. *Electrochimica Acta*, 51(23):4909–4915, 2006.

[87] Jordan L, Shukla A, Behrsing T, Avery N, Muddle B, and Forsyth M. Diffusion layer parameters influencing optimal fuel cell performance. *Journal of Power Sources*, 86(1):250–254, 2000.

[88] Passalacqua E, Squadrito G, Lufrano F, Patti A, and Giorgi L. Effects of the diffusion layer characteristics on the performance of polymer electrolyte fuel cell electrodes. *Journal of Applied Electrochemistry*, 31(4):449–454, 2001.

[89] Qi Z and Kaufman A. Improvement of water management by a microporous sublayer for pem fuel cells. *Journal of Power Sources*, 109(1):38–46, 2002.

[90] Park J, Pasaogullari U, and Bonville L. J. A new ccm/mpl structure for high power density polymer electrolyte fuel cells. *ECS Transactions*, 64(3):353–359, 2014.

[91] Park J, Pasaogullari U, and Bonville L. J. Characterization studies of a new mea structure for polymer electrolyte fuel cells. *ECS Transactions*, 69(17): 1355–1362, 2015.

[92] Kitahara T, Nakajima H, and Mori K. Hydrophilic and hydrophobic double microporous layer coated gas diffusion layer for enhancing performance of polymer electrolyte fuel cells under no-humidification at the cathode. *Journal of Power Sources*, 199:29–36, 2012.

[93] Kitahara T, Nakajima H, and Morishita M. Water vapor exchange system using a hydrophilic microporous layer coated gas diffusion layer to enhance performance of polymer electrolyte fuel cells without cathode humidification. *Journal of Power Sources*, 214:100–106, 2012.

[94] Kitahara T, Nakajima H, Inamoto M, and Morishita M. Novel hydrophilic and hydrophobic double microporous layer coated gas diffusion layer to enhance performance of polymer electrolyte fuel cells under both low and high humidity. *Journal of Power Sources*, 234:129–138, 2013.

[95] Kitahara T, Nakajima H, Inamoto M, and Shinto K. Triple microporous layer coated gas diffusion layer for performance enhancement of polymer electrolyte fuel cells under both low and high humidity conditions. *Journal of Power Sources*, 248:1256–1263, 2014.

[96] Ahn M, Cho Y.-H, Cho Y.-H, Kim J, Jung N, and Sung Y.-E. Influence of hydrophilicity in micro-porous layer for polymer electrolyte membrane fuel cells. *Electrochimica Acta*, 56(5):2450–2457, 2011.

[97] Tanuma T and Kinoshita S. Impact of cathode fabrication on fuel cell performance. *Journal of The Electrochemical Society*, 161(1):F94–F98, 2014.

[98] Secanell M, Karan K, Suleman A, and Djilali N. Multi-variable optimization of pemfc cathodes using an agglomerate model. *Electrochimica Acta*, 52(22): 6318–6337, 2007.

[99] Karan K. Assessment of transport-limited catalyst utilization for engineering of ultra-low pt loading polymer electrolyte fuel cell anode. *Electrochemistry Communications*, 9(4):747–753, 2007.

[100] Shukla S, Bhattacharjee S, and Secanell M. Rationalizing catalyst inks for pemfc electrodes based on colloidal interactions. *ECS Transactions*, 58(1):1409–1428, 2013.

[101] Uchida M, Aoyama Y, Eda N, and Ohta A. Investigation of the microstructure in the catalyst layer and effects of both perfluorosulfonate ionomer and ptfe-loaded carbon on the catalyst layer of polymer electrolyte fuel cells. *Journal of the Electrochemical Society*, 142(12):4143–4149, 1995.

[102] Uchida M, Fukuoka Y, Sugawara Y, Ohara H, and Ohta A. Improved preparation process of very-low-platinum-loading electrodes for polymer electrolyte fuel cells. *Journal of The Electrochemical Society*, 145(11):3708–3713, 1998.

[103] Therdthianwong A, Ekdharmasuit P, and Therdthianwong S. Fabrication and performance of membrane electrode assembly prepared by a catalyst-coated membrane method: effect of solvents used in a catalyst ink mixture. *Energy & Fuels*, 24(2):1191–1196, 2010.

[104] Yang T.-H, Yoon Y.-G, Park G.-G, Lee W.-Y, and Kim C.-S. Fabrication of a thin catalyst layer using organic solvents. *Journal of power sources*, 127(1): 230–233, 2004.

[105] Chisaka M and Daiguji H. Effect of organic solvents on catalyst layer structure in polymer electrolyte membrane fuel cells. *Journal of The Electrochemical Society*, 156(1):B22–B26, 2009.

[106] Sun L, Zhang H, Ilavsky J, Li Z, and Xie J. Investigation of solvent effects on the dispersion of carbon agglomerates and nafion ionomer particles in catalyst inks using ultra small angle x-ray scattering and cryo-tem. *ECS Transactions*, 50(2):1461–1466, 2013.

[107] Huang T, Shen H, Jao T, Weng F, and Su A. Ultra-low pt loading for proton exchange membrane fuel cells by catalyst coating technique with ultrasonic spray coating machine. *international journal of hydrogen energy*, 37(18):13872–13879, 2012.

[108] Millington B, Du S, and Pollet B. G. The effect of materials on proton exchange membrane fuel cell electrode performance. *Journal of Power Sources*, 196(21):9013–9017, 2011.

[109] Fernandez R, Ferreira-Aparicio P, and Daza L. Pemfc electrode preparation: influence of the solvent composition and evaporation rate on the catalytic layer microstructure. *Journal of power sources*, 151:18–24, 2005.

[110] Malek K, Eikerling M, Wang Q, Navessin T, and Liu Z. Self-organization in catalyst layers of polymer electrolyte fuel cells. *The Journal of Physical Chemistry C*, 111(36):13627–13634, 2007.

[111] Xiao Y, Dou M, Yuan J, Hou M, Song W, and Sundén B. Fabrication process simulation of a pem fuel cell catalyst layer and its microscopic structure characteristics. *Journal of The Electrochemical Society*, 159(3):B308–B314, 2012.

[112] Pollet B. G. Lets not ignore the ultrasonic effects on the preparation of fuel cell materials. *Electrocatalysis*, 5(4):330–343, 2014.

[113] Derby B. Inkjet printing of functional and structural materials: fluid property requirements, feature stability, and resolution. *Annual Review of Materials Research*, 40:395–414, 2010.

[114] Mangal P, Pant L. M, Carrigy N, Dumontier M, Zingan V, Mitra S, and Secanell M. Experimental study of mass transport in pemfcs: Through plane permeability and molecular diffusivity in gdls. *Electrochimica Acta*, 167:160–171, 2015.

[115] Cooper K. R. *Experimental methods and data analyses for polymer electrolyte fuel cells*. Scribner Associates, 2005.

[116] Wu J, Yuan X. Z, Wang H, Blanco M, Martin J. J, and Zhang J. Diagnostic tools in pem fuel cell research: Part i electrochemical techniques. *International journal of hydrogen energy*, 33(6):1735–1746, 2008.

[117] Bard A. J and Faulkner L. R. *Electrochemical methods: fundamentals and applications*, volume 2. Wiley New York, 1980.

[118] Baturina O. A, Aubuchon S. R, and Wynne K. J. Thermal stability in air of pt/c catalysts and pem fuel cell catalyst layers. *Chemistry of Materials*, 18(6): 1498–1504, 2006.

[119] Wang Q, Eikerling M, Song D, Liu Z, Navessin T, Xie Z, and Holdcroft S. Functionally graded cathode catalyst layers for polymer electrolyte fuel cells i. theoretical modeling. *Journal of the Electrochemical Society*, 151(7):A950– A957, 2004.

[120] Iden H and Ohma A. An in situ technique for analyzing ionomer coverage in catalyst layers. *Journal of Electroanalytical Chemistry*, 693:34–41, 2013.

[121] Lefebvre M. C, Martin R. B, and Pickup P. G. Characterization of ionic conductivity profiles within proton exchange membrane fuel cell gas diffusion electrodes by impedance spectroscopy. *Electrochemical and solid-state letters*, 2(6): 259–261, 1999.

[122] Cooper K and Smith M. Electrical test methods for on-line fuel cell ohmic resistance measurement. *Journal of Power Sources*, 160(2):1088–1095, 2006.

[123] Bockris J and Oldfield L. The oxidation-reduction reactions of hydrogen peroxide at inert metal electrodes and mercury cathodes. *Transactions of the Faraday Society*, 51:249–259, 1955.

[124] Parthasarathy A, Srinivasan S, Appleby A, and Martin C. Temperature dependence of the electrode kinetics of oxygen reduction at the platinum/nafion® interfacea microelectrode investigation. *Journal of the Electrochemical Society*, 139(9):2530–2537, 1992.

[125] Parthasarathy A, Srinivasan S, Appleby A, and Martin C. Pressure dependence of the oxygen reduction reaction at the platinum microelectrode/nafion

interface: electrode kinetics and mass transport. *Journal of the Electrochemical Society*, 139(10):2856–2862, 1992.

[126] Basura V, Beattie P. D, and Holdcroft S. Solid-state electrochemical oxygen reduction at pt nafion® 117 and pt—bam3g 407 interfaces. *Journal of Electroanalytical Chemistry*, 458(1):1–5, 1998.

[127] Beattie P. D, Basura V. I, and Holdcroft S. Temperature and pressure dependence of o 2 reduction at pt nafion® 117 and pt—bam 407 interfaces. *Journal of Electroanalytical Chemistry*, 468(2):180–192, 1999.

[128] Zhang L, Ma C, and Mukerjee S. Oxygen reduction and transport characteristics at a platinum and alternative proton conducting membrane interface. *Journal of Electroanalytical Chemistry*, 568:273–291, 2004.

[129] Mani A and Holdcroft S. Highly temperature dependent mass-transport parameters for orr in nafion® 211. *Journal of electroanalytical chemistry*, 651(2): 211–215, 2011.

[130] Paulus U, Schmidt T, Gasteiger H, and Behm R. Oxygen reduction on a high-surface area pt/vulcan carbon catalyst: a thin-film rotating ring-disk electrode study. *Journal of Electroanalytical Chemistry*, 495(2):134–145, 2001.

[131] Wakabayashi N, Takeichi M, Itagaki M, Uchida H, and Watanabe M. Temperature-dependence of oxygen reduction activity at a platinum electrode in an acidic electrolyte solution investigated with a channel flow double electrode. *Journal of Electroanalytical Chemistry*, 574(2):339–346, 2005.

[132] Dhanda A, O'Hayre R, and Pitsch H. Orr adsorbate dynamics on pt single crystal pem fuel cells. *ECS Transactions*, 16(2):1131–1142, 2008.

[133] Zhang L, Ma C, and Mukerjee S. Oxygen permeation studies on alternative proton exchange membranes designed for elevated temperature operation. *Electrochimica Acta*, 48(13):1845–1859, 2003.

[134] Subramanian N, Greszler T, Zhang J, Gu W, and Makharia R. Pt-oxide coverage-dependent oxygen reduction reaction (orr) kinetics. *Journal of The Electrochemical Society*, 159(5):B531–B540, 2012.

[135] Moore M, Putz A, and Secanell M. Investigation of the orr using the double-trap intrinsic kinetic model. *Journal of the Electrochemical Society*, 160(6): F670–F681, 2013.

[136] Martin S, Martinez-Vazquez B, Garcia-Ybarra P, and Castillo J. Peak utilization of catalyst with ultra-low pt loaded pem fuel cell electrodes prepared by the electrospray method. *Journal of Power Sources*, 229:179–184, 2013.

[137] Yu Z and Carter R. Measurement of effective oxygen diffusivity in electrodes for proton exchange membrane fuel cells. *Journal of Power Sources*, 195(4): 1079–1084, 2010.

[138] Gode P, Jaouen F, Lindbergh G, Lundblad A, and Sundholm G. Influence of the composition on the structure and electrochemical characteristics of the pefc cathode. *Electrochimica Acta*, 48(28):4175–4187, 2003.

[139] Cho Y, Park H, Cho Y, Jung D, Park H, and Sung Y. Effect of platinum amount in carbon supported platinum catalyst on performance of polymer electrolyte membrane fuel cell. *Journal of Power Sources*, 172(1):89–93, 2007.

[140] Uchimura M and Kocha S. 214th ecs meeting. *Honolulu, HI, Abstract*, (914), 2008.

[141] Markiewicz M, Zalitis C, and Kucernak A. Performance measurements and modelling of the orr on fuel cell electrocatalysts–the modified double trap model. *Electrochimica Acta*, 179:126–136, 2015.

[142] Inaba M, Yamada H, Tokunaga J, and Tasaka A. Effect of agglomeration of pt/c catalyst on hydrogen peroxide formation. *Electrochemical and Solid-State Letters*, 7(12):A474–A476, 2004.

[143] Liu W and Zuckerbrod D. In situ detection of hydrogen peroxide in pem fuel cells. *Journal of The Electrochemical Society*, 152(6):A1165–A1170, 2005.

[144] Carrigy N. B, Pant L. M, Mitra S, and Secanell M. Knudsen diffusivity and permeability of pemfc microporous coated gas diffusion layers for different polytetrafluoroethylene loadings. *Journal of The Electrochemical Society*, 160(2): F81–F89, 2013.

[145] Park S, Lee J.-W, and Popov B. N. Effect of carbon loading in microporous layer on pem fuel cell performance. *Journal of Power Sources*, 163(1):357–363, 2006.

[146] Aizawa M and Gyoten H. Effect of micro-patterned membranes on the cathode performances for pem fuel cells under low humidity. *Journal of The Electrochemical Society*, 160(4):F417–F428, 2013.

[147] Koh J. K, Jeon Y, Cho Y. I, Kim J. H, and Shul Y.-G. A facile preparation method of surface patterned polymer electrolyte membranes for fuel cell applications. *Journal of Materials Chemistry A*, 2(23):8652–8659, 2014.

[148] Therdthianwong A, Saenwiset P, and Therdthianwong S. Cathode catalyst layer design for proton exchange membrane fuel cells. *Fuel*, 91(1):192–199, 2012.

[149] Deshmukh A. B, Kale V. S, Dhavale V. M, Sreekumar K, Vijayamohanan K, and Shelke M. V. Direct transfer of micro-molded electrodes for enhanced mass transport and water management in pemfc. *Electrochemistry Communications*, 12(11):1638–1641, 2010.

[150] Xu R, Wu C, and Xu H. Particle size and zeta potential of carbon black in liquid media. *Carbon*, 45(14):2806–2809, 2007.

[151] Polyanskiy M. N. Refractive index database, 2014. http://refractiveindex. info. Accessed: March 15, 2016.

[152] Anderson W, Kozak D, Coleman V. A, Jämting Å. K, and Trau M. A comparative study of submicron particle sizing platforms: Accuracy, precision and resolution analysis of polydisperse particle size distributions. *Journal of colloid and interface science*, 405:322–330, 2013.

[153] Elimelech M, Jia X, Gregory J, and Williams R. *Particle deposition & aggregation: measurement, modelling and simulation*. Butterworth-Heinemann, 1998.

[154] Morrison I. D. Criterion for electrostatic stability of dispersions at low ionic strength. *Langmuir*, 7(9):1920–1922, 1991.

[155] Mishchuk N. A. The model of hydrophobic attraction in the framework of classical dlvo forces. *Advances in colloid and interface science*, 168(1):149–166, 2011.

[156] Masliyah J and S.Bhattacharjee . *Electrokinetic and Colloid Transport Phenomena*. Wiley Online Library, 2006.

[157] Israelachvili J. *Intermolecular and surface forces: revised third edition*. Academic press, 2011.

[158] Berg J. *Introduction to Interfaces and Colloids*. World Scientific Publishing Company Incorporated, 2009.

[159] Marmur A. A kinetic theory approach to primary and secondary minimum coagulations and their combination. *Journal of Colloid and Interface Science*, 72(1):41–48, 1979.

[160] Santiago D, Rodríguez-Calero G. G, Rivera H, Tryk D. A, Scibioh M. A, and Cabrera C. R. Platinum electrodeposition at high surface area carbon vulcan-xc-72r material using a rotating disk-slurry electrode technique. *Journal of The Electrochemical Society*, 157(12):F189–F195, 2010.

[161] Dullien F. A. *Porous media: fluid transport and pore structure*. Academic press, 2012.

[162] Viswanath B, Patra S, Munichandraiah N, and Ravishankar N. Nanoporous pt with high surface area by reaction-limited aggregation of nanoparticles. *Langmuir*, 25(5):3115–3121, 2009.

[163] Kongkanand A and Mathias M. F. The priority and challenge of high-power performance of low-platinum proton-exchange membrane fuel cells. *The journal of physical chemistry letters*, 7:1127–1137, 2016.

[164] Steinbach A. 2014 annual merit review doe hydrogen and fuel cells and vehicle technologies programs. https://www.hydrogen.energy.gov/pdfs/review14/fc104˙steinbach˙2014˙o.pdf. Accessed: May 27, 2016.

[165] Zlotorowicz A, Jayasayee K, Dahl P, Thomassen M, and Kjelstrup S. Tailored porosities of the cathode layer for improved polymer electrolyte fuel cell performance. *Journal of Power Sources*, 287:472–477, 2015.

[166] Arisetty S, Wang X, Ahluwalia R, Mukundan R, Borup R, Davey J, Langlois D, Gambini F, Polevaya O, and Blanchet S. Catalyst durability in pem fuel cells with low platinum loading. *Journal of The Electrochemical Society*, 159 (5):B455–B462, 2012.

[167] Bhaiya M, Putz A, and Secanell M. Analysis of non-isothermal effects on polymer electrolyte fuel cell electrode assemblies. *Electrochimica Acta*, 147:294–309, 2014.

[168] Springer T. E, Zawodzinski T, and Gottesfeld S. Polymer electrolyte fuel cell model. *Journal of the Electrochemical Society*, 138(8):2334–2342, 1991.

Appendix A

Conditioning protocol, RH and stoichiometry calculations

A.1   Cell conditioning

After assembly and prior to testing, the cell was conditioned at 80% RH, 80°C, using the following protocol:

- Applying a constant current of 0.1 A for 60 minutes and monitoring the voltage

- Applying a constant current of 0.25 A for 60 minutes and monitoring the voltage

- Applying a constant current of 0.5 A for 60 minutes and monitoring the voltage

- Applying a constant current of 1 A for 120 minutes and monitoring the voltage

- Applying a constant current of 2 A for 120 minutes and monitoring the voltage

- Applying a constant current of 3 A for 120 minutes and monitoring the voltage

- Applying a constant current of 4 A for 120 minutes and monitoring the voltage

- Applying a constant current of 5 A for 120 minutes and monitoring the voltage

- Applying a constant current of 6 A for 120 minutes and monitoring the voltage (for higher Pt loading electrodes)

A.2   Calculation of reactant RH

Relative humidity of the reactants was varied by changing the humidifier temperature with respect to the cell temperature. It was assumed that the reactant gases

are saturated at the humidifier temperature prior to entering the cell. Anodic and cathodic RH (%) was calculated using the following relation,

$$RH = \frac{p_{sat}|_{HT}}{p_{sat}|_{CT}} \times 100 \tag{A.1}$$

where $p_{sat}|_{HT}$ is the saturation pressure of water at humidifier temperature and $p_{sat}|_{CT}$ is the saturation pressure at cell temperature. The saturation pressure of water, p_{sat} (atm) was calculated by using the following equation, [167, 168]

$$log_{10}(p_{sat}) = -2.1794 + (0.02953T - 9.1837 \times 10^{-5}T^2) + (1.4454 \times 10^{-7}T^3) \tag{A.2}$$

where T is the temperature in Celsius. Based on equations (A.1) and (A.2), for a desired value of RH the anodic/cathodic humidifier temperatures and the cell temperature were set during the fuel cell operation. Usually, at a cell temperature of 80°C, the humidifier temperatures were set to 64°C, 71°C and 77°C for RH values of 50%, 70% and 90% respectively.

A.3   Calculation of stoichiometry

Stoichiometric ratio, S is the ratio of the total amount of reactant supplied to the system to the amount of reactant consumed [115]. Since the amount of reactant consumed will increase with increasing current density based on Faraday's law, the stoichiometric ratio will decrease with current for a constant flow-rate of reactants. S also depends on the partial pressures of hydrogen (p_{H_2}) and oxygen (p_{O_2}) which are a function of temperature and RH. For hydrogen, the stoichiometric ratio, S_{H_2} is given as

$$S_{H_2} = p_{H_2} \frac{v^s_{H_2}}{v^c_{H_2}} \tag{A.3}$$

where p_{H_2} is the hydrogen partial pressure, $v^s_{H_2}$ is the mass flow rate supplied in liters per minute and $v^c_{H_2}$ is the mass flow rate of the consumed hydrogen. The mass flow rate of consumed hydrogen (lpm) is given as,

$$v^c_{H_2} = \left(\frac{RT}{P}\right)\left(\frac{I}{2F}\right) \times 60 \tag{A.4}$$

where R is the ideal gas constant (0.0821 l.atm/mol.K), T is the temperature in K, P is the pressure in atm, I is the current in A and F is the Faraday constant (96485 C/mol). Similarly, the stoichiometric ratio for oxygen is calculated using the following,

$$S_{O_2} = p_{O_2} \frac{v_{O_2}^s}{v_{O_2}^c} \tag{A.5}$$

where p_{O_2} is the oxygen partial pressure, $v_{O_2}^s$ is the supplied mass flow rate (lpm) and $v_{O_2}^c$ is the mass flow rate of the consumed oxygen (lpm), which is given as

$$v_{O_2}^c = \left(\frac{RT}{P}\right)\left(\frac{I}{4F}\right) \times 60 \tag{A.6}$$